FEDERICO TORRIANO

INVESTIGATION OF THE 3D FLOW CHARACTERISTICS IN A ROTATING CHANNEL SETUP

Mémoire présenté
à la Faculté des études supérieures de l'Université Laval
dans le cadre du programme de maîtrise en génie mécanique
pour l'obtention du grade de maître ès sciences (M.Sc.)

FACULTÉ DES SCIENCES ET DE GÉNIE
UNIVERSITÉ LAVAL
QUÉBEC

OCTOBRE 2006

Résumé

L'objectif de ce projet de maîtrise est de contribuer à une meilleure compréhension des écoulements dans les conduits rectangulaires en rotation. Une attention particulière est apportée aux effets de bout et au développement de l'écoulement.
Des simulations RANS en régime stationnaire ont démontré que la présence d'un écoulement secondaire de faible intensité est suffisante pour modifier le profil de vitesse axiale de façon à que ce dernier diffère significativement de la solution théorique 2D. En conséquence, les comparaisons entre les résultats expérimentaux et les simulations numériques 2D devraient être faites avec prudence.
Les calculs stationnaires ont également montré que le développement de l'écoulement dans un canal tournant est affecté par l'apparition de cellules de type Taylor-Görtler le long du mur pression. Puisque ces tourbillons sont légèrement inclinés par rapport au plan horizontal, une solution stationnaire pleinement développée n'est jamais atteinte. Des simulations subséquentes en régime instationnaire dans un domaine périodique ont prouvé qu'une solution pleinement développée peut cependant exister dans un canal tournant, mais l'écoulement est alors formellement instationnaire car les cellules longitudinales sont convectées vers les bouts de la conduite par l'action de l'écoulement secondaire.

Abstract

The objective of the present work is to provide a basic description and to contribute toward a better understanding of rotating high aspect ratio duct flows. Particular attention is given to end-wall effects and flow development.
Steady RANS simulations have shown that the presence of a weak, but unavoidable, end-wall generated secondary flow produces sufficient transverse advection to alter the streamwise velocity profile in such a way that it differs noticeably from the theoretical 2D channel case. Thus, comparisons between experimental results and 2D numerical simulations should be performed very cautiously.
Steady state calculations have also revealed that the flow development in a rotating duct is subtly affected by the appearance of longitudinal Taylor-Görtler type cells near the pressure wall. Since the roll cells are tilted toward the end-wall, no steady fully developed solution is ever reached.
Subsequent unsteady flow calculation in a streamwise periodic domain have shown that a fully developed solution can exist in a rotating duct, but the resulting flow field is formally unsteady due to the convection of the roll cells toward the end-wall.

Avant-propos

J'aimerais d'abord remercier mon directeur de recherche, le professeur Guy Dumas. Ses précieux conseils et son ample expertise dans le domaine de la mécanique des fluides numérique m'ont permis de mener à terme le projet de maîtrise et d'acquérir des bonnes connaissances de base en CFD. Je tiens également à souligner la contribution du professeur Yvan Maciel car son expertise dans le domaine des écoulements en repère tournant a grandement contribué au bon déroulement de mes recherches.
Je voudrais aussi souligner le soutien financier du Conseil de Recherche en Sciences Naturelles et Génie (CRSNG) du Canada et la contribution, via son programme de bourses, du Fond Québécois de la Recherche sur la Nature et les Technologies (FQRNT). Leur appui financier a été grandement apprécié.
Je souhaiterais également exprimer ma profonde gratitude à Steve Julien avec qui j'ai partagé une grande partie du projet de recherche. Je profite également de cette occasion pour saluer tous les étudiants membres du LMFN et en particulier Florian, Thomas, Julie, Pascal, Félix-Antoine et Pierre-Luc.
En dernier lieu, je veux exprimer ma plus grande gratitude à mes parents à qui ce travail est dédié.

A tutta la mia famiglia

Semper ad maiora

Contents

Résumé ii

Abstract iii

Avant-propos iv

Contents vi

List of Tables viii

List of Figures ix

1 Introduction 1
- 1.1 Preliminaries . . . 1
- 1.2 Objectives . . . 3
- 1.3 Methodology . . . 3

2 Theoretical background 4
- 2.1 Governing equations . . . 4
- 2.2 Flow phenomena in a rotating channel . . . 5
- 2.3 Flow phenomena in a rotating duct . . . 7
- 2.4 Flow phenomena in a bend . . . 10

3 Numerical method 12
- 3.1 *Fluent*: a finite volume solver . . . 12
- 3.2 RANS approach to turbulent flows . . . 13
- 3.3 Wall treatment . . . 17
- 3.4 Numerical schemes . . . 19

4 Validation efforts 21
- 4.1 Validation of the turbulence model and wall treatment . . . 21
- 4.2 Validation of the boundary conditions . . . 25

5 Fully developed flow in rotating channels and rectangular ducts 32

5.1 Fully developed flow in a rotating channel 32
5.2 Fully developed flow in a rotating duct 36
5.2.1 Mesh independence 37
5.2.2 End-wall effects on two-dimensionality 41
5.2.3 Reynolds and Rotation number effects 46
5.2.4 Comparison between experimental and DNS data 52

6 Flow development in a rotating channel **54**
6.1 Effect of rotation on flow development 54
6.1.1 Mesh independence 55
6.1.2 Flow development in a rotating and non-rotating channel 57
6.2 Validation of the design hypothesis 61
6.3 Improvements on the actual design 69

7 Flow development in a rotating duct **74**
7.1 Effect of rotation on flow development 74
7.1.1 Mesh independence 74
7.1.2 Flow development in a rotating and non-rotating duct 77
7.1.3 Effect of mesh discretization on roll cell instability 84
7.1.4 Effect of roll cell instability on flow development 87
7.2 Validation of the design hypothesis 90
7.3 Improvements on the actual design 99

8 Unsteady fully developed flow in a rotating duct **105**
8.1 Unsteady calculation in a rotating duct of finite aspect ratio 105
8.2 Unsteady calculation in a rotating duct of infinite aspect ratio 110

9 Conclusion **112**

Bibliography **115**

A Fully developed solution with periodic boundary conditions **118**

B Tested designs for promoting flow development **122**
B.1 Actual channel without splitter plate 122
B.2 Actual channel with symmetric lips 123
B.3 Actual channel with symmetric lips and flaps 124
B.4 Actual channel with symmetric lips, flaps and filters 125

C Parallel solver performance **127**

List of Tables

4.1 Comparaison of non-rotating case - $Re = 6210$. 22
4.2 Comparaison of rotating case - $Re = 6899$ at $Ro = 0.2$. 22
4.3 $\|\triangle_{L=100h}\|_{RMS}$ values in a yz plane of a rotating duct at two measurement stations - $Re = 40000$ and $Ro = 0.22$. 29

5.1 Rotation effect on wall shear stress at $Re = 40000$. 34
5.2 Reynolds effect on wall shear stress at $Ro = 0.22$. 34
5.3 $\|\triangle\|_{RMS}$ values in the central yz plane of a rotating duct at $Re = 40000$ and $Ro = 0.22$. 40
5.4 $\|\triangle\|_{RMS}$ values at symmetry axis of a rotating duct at $Re = 40000$ and $Ro = 0.22$. 40
5.5 $\|\triangle_{z/h=0}\|_{RMS}$ values of streamwise velocity at different spanwise locations (from symmetry plane at $z/h = 0$ toward the end wall of a rotating and non-rotating duct at $Re = 40000$. 45
5.6 $\|\triangle_{2D}\|_{RMS}$ values of streamwise velocity at different locations of a rotating and non-rotating duct at $Re = 40000$. 45
5.7 $\|\triangle_{2D}\|_{RMS}$ values of streamwise velocity at the symmetry plane of a rotating duct at $Ro = 0.22$. 52

6.1 $\|\triangle\|_{RMS}$ values at different stations along a rotating channel at $Re = 40000$ and $Ro = 0.22$. 55

7.1 $\|\triangle\|_{RMS}$ values at different stations along a duct at $Re = 40000$ and $Ro = 0$. 77

A.1 $\|\triangle\|_{RMS}$ values at the central position of a periodic domain. 118
A.2 2D channel at $Re = 40000$ and $Ro = 0$. Maximum variable fluctuations along a line at $y/h = -0.5$. 121

C.1 Computational time of serial and parallel solvers. 127
C.2 Computational gain from parallel solver. 128
C.3 Computational gain from parallel solver. 128

List of Figures

1.1 Experimental setup. (a): top view; (b): side view. From Maciel *et al.* (2003). 2

1.2 Experimental results (Maciel *et al.*, 2003). (a): Mean streamwise velocity profiles at $Re_\tau \approx 180$. $\square, x/h = 80$; $\triangle, x/h = 118$; —, DNS (Alvelius *et al.*, 1999). (b): R.m.s. streamwise velocity fluctuations at $Re_\tau \approx 180$, symbols as in (a). 2

2.1 Rotating turbulent channel flow. —, Streamwise velocity profile for $Ro > 0$; - - -, streamwise velocity profile for $Ro = 0$. 6

2.2 Secondary flow generation in a rotating duct. 8

2.3 Roll cells instability in rotating duct flow. Light gray contours: $\omega_x > 0$; dark gray: $\omega_x < 0$. 9

2.4 Details of the experimental setup configuration. Secondary flow generation in a bend (Dean-type cells). 11

3.1 Velocity profile as a function of distance normal to the wall. $\square$, Experimental data; - - -, wall functions. From Ferziger & Perić, 2002. 17

3.2 Wall function approach. 18

3.3 Finite volume approach for a Cartesian 2D grid. From Ferziger & Peric, 1992. 20

4.1 Coarse mesh for rotating case. 22

4.2 Mean velocity profiles in wall coordinates for different rotation rates ($0 \leq Ro \leq 0.50$) at $Re = 2900$. From Kristoffersen & Andersson, 1993. 23

4.3 Normalized mean velocity profiles and Reynolds stress components. $\square$, Coarse mesh; $\triangle$, fine mesh; —, DNS by Alvelius. (a): $Re = 6210$ at $Ro = 0$; (b): $Re = 6899$ at $Ro = 0.20$. 24

4.4 Normalized mean velocity profiles and Reynolds stress components at $Re = 40000$ and $Ro = 0.22$. $\square$, Domain of length $60h$; —, domain of length $100h$. (a): Measurement station at $x/h = 50$ ($10h$ from exit boundary of shorter domain); (b): measurement station at $x/h = 60$ (at exit boundary of shorter domain). 27

4.5 Plane contours in a rotating duct at $Re = 40000$ and $Ro = 0.22$. Flow direction toward the observer. (a): Measurement station at $x/h = 50$ ($10h$ from exit boundary of shorter domain); (b): measurement station at $x/h = 60$ (at exit boundary of shorter domain). Top figures correspond to the short domain while bottom ones correspond to the long domain. 28

4.6 Fully developed solution in a rotating duct at $Re = 40000$ and $Ro = 0.22$. Normalized mean velocity profiles and Reynolds stress components along a line placed at $x/h = 0$ and $z/h = 0$. □, Domain with *symmetry* condition; —, whole domain. 30

4.7 Fully developed solution in a rotating duct at $Re = 40000$ and $Ro = 0.22$. Normalized mean velocity profiles and Reynolds stress components along a line placed at $x/h = 0$ and $z/h = 2$. □, Domain with *symmetry* condition; —, whole domain. 31

5.1 Fully developed solution in a rotating channel at $Re = 40000$. Normalized mean streamwise velocity and Reynolds stress components. —, $Ro = 0$; – –, $Ro = 0.11$; - - -, $Ro = 0.22$. 33

5.2 Fully developed solution in a rotating channel at $Ro = 0.22$. Normalized mean streamwise velocity and Reynolds stress components. —, $Re = 40000$; – –, $Re = 20000$; - - -, $Re = 10000$. 35

5.3 (a): Computational domain of 3D fully developed duct. (b): Mesh distribution in the yz plane; size of wall-adjacent cells corresponds to case at $Re = 40000$ and $Ro = 0.22$. 37

5.4 Plane contours of a rotating duct at $Re = 40000$ and $Ro = 0.22$. (a): Standard mesh; (b): fine mesh. Flow direction toward the observer. 38

5.5 Profiles at symmetry axis of a rotating duct at $Re = 40000$ and $Ro = 0.22$. —, Fine mesh; – –, standard mesh. 39

5.6 End-wall effects in a rotating duct at $Re = 40000$ and $Ro = 0.22$. Flow direction toward the observer. 41

5.7 Velocity and Reynolds stress profiles of a rotating duct/channel at $Re = 40000$ and $Ro = 0.22$. —, 3D case (at symmetry plane); – –, 2D case. U_m is the mean velocity at the symmetry plane. 42

5.8 Turbulence and secondary flow contributions to the x-momentum equation at the symmetry plane of a rotating duct (thin lines) and rotating channel (thick line); $Re = 40000$ and $Ro = 0.22$. 43

5.9 Velocity profiles at different spanwise locations of a duct at $Re = 40000$: $z/h = 0$, $z/h = 2$, $z/h = 4$, $z/h = 6$, $z/h = 8$, $z/h = 10$. (a): $Ro = 0.22$; (b): $Ro = 0$. —, 3D case; – –, 2D case. The direction of the arrows indicates increasing z. 44

5.10 Plane contours of a duct at $Re = 40000$. (a): $Ro = 0.11$; (b): $Ro = 0$. Flow direction toward the observer. 47

5.11 Velocity and Reynolds stress profiles of a duct and channel at $Re = 40000$. —, 3D case (at symmetry plane); – –, 2D case. U_m is the mean velocity at the symmetry plane. 48
5.12 Turbulence and secondary flow contributions to the x-momentum equation at the symmetry plane of a rotating duct at $Ro = 0.22$. Black lines: $Re = 40000$; red lines: $Re = 20000$; green lines: $Re = 10000$. 49
5.13 Plane contours of a duct at $Ro = 0.22$. (a): $Re = 20000$; (b): $Re = 10000$. Flow direction toward the observer. 50
5.14 Velocity and Reynolds stress profiles of a duct and channel at $Ro = 0.22$. —, 3D case (at symmetry plane); – –, 2D case. U_m is the mean velocity at the symmetry plane. 51
5.15 Experimental streamwise velocity profile at the symmetry plane of a rotating duct at $Re = 2897$ and $Ro = 0.22$ (Maciel *et al.*, 2003). $\square, x/h = 80$; $\bigcirc, x/h = 135$; – –, DNS (Alvelius *et al.*, 1999). 53

6.1 Standard mesh for studying the flow development in a rotating channel at $Re = 40000$ and $Ro = 0.22$. 55
6.2 Streamwise velocity and turbulent viscosity ratio profiles at different stations along a rotating channel at $Re = 40000$ and $Ro = 0.22$. —, Fine mesh; – –, standard mesh. 56
6.3 Streamwise velocity profiles at different stations along a channel at $Re = 40000$. —, Solution at measurement station; – –, fully developed solution. (a): $Ro = 0$; (b): $Ro = 0.22$. (c): $\|\triangle_{FD}\|_{RMS}$ norm of the difference. 58
6.4 Turbulent viscosity ratio profiles at different stations along a channel at $Re = 40000$. —, Solution at measurement station; – –, fully developed solution. (a): $Ro = 0$; (b): $Ro = 0.22$. (c): $\|\triangle_{FD}\|_{RMS}$ norm of the difference. 61
6.5 (a): Top view of experimental setup; (b): 2D computational domain. 62
6.6 Inlet section of computational domain. Mesh discretization for case study at $Re = 40000$ and $Ro = 0.22$. 63
6.7 Streamwise velocity profiles and $\|\triangle_{FD}\|_{RMS}$ values at different stations along a rotating channel at $Ro = 0.22$. —, Straight channel; — – —, actual channel; – –, fully developed solution. (a): $Re = 40000$; (b): $Re = 20000$. 64
6.8 Streamlines in the entrance region of the actual channel at $Ro = 0.22$. (a): $Re = 40000$; (b): $Re = 20000$. 65
6.9 Turbulent viscosity ratio profiles at different stations along a rotating channel at $Ro = 0.22$. —, Straight channel; — – —, actual channel; – –, fully developed solution. (a): $Re = 40000$; (b): $Re = 20000$. 66
6.10 Streamwise velocity profiles and $\|\triangle_{FD}\|_{RMS}$ values at different stations along a rotating channel at $Ro = 0.22$. —, Straight channel; — – —, actual channel; – –, fully developed solution. (a): $Re = 40000$; (b): $Re = 20000$. 67

6.11 Streamlines in the entrance region of the actual channel at $Ro = 0.22$. (a): $Re = 40000$; (b): $Re = 20000$. 68
6.12 Inlet section of computational domain. Mesh discretization for case study at $Re = 40000$ and $Ro = 0.22$. 69
6.13 Streamlines in the entrance region of the modified channel at $Ro = 0.22$. (a): $Re = 40000$; (b): $Re = 20000$. 70
6.14 Streamwise velocity profiles and $\|\triangle_{FD}\|_{RMS}$ values at different stations along a rotating channel at $Ro = 0.22$. ——, Actual channel; — – —, modified channel; – –, fully developed solution. (a): $Re = 40000$; (b): $Re = 20000$. 71
6.15 Turbulent viscosity ratio profiles at different stations along a rotating channel at $Ro = 0.22$. ——, Actual channel; — – —, modified channel; – –, fully developed solution. (a): $Re = 40000$; (b): $Re = 20000$. 72

7.1 Coarse and refined meshes for studying the flow development in a non-rotating duct at $Re = 40000$. 75
7.2 Flow development in a duct at $Re = 40000$ and $Ro = 0$. Plane contours at $x/h = 140$. (a): Standard mesh; (b): fine mesh. Flow direction toward the observer. 76
7.3 Evolution of the mean velocity at the symmetry plane of a duct at $Re = 40000$. 78
7.4 Streamwise velocity profiles (normalized with the bulk velocity) at symmetry plane of a duct at $Re = 40000$. ——, Solution at measurement station; – –, fully developed solution. (a): $Ro = 0$; (b): $Ro = 0.22$. (c): $\|\triangle_{FD}\|_{RMS}$ norm of the difference. 80
7.5 Streamwise velocity profiles (normalized with the mean velocity) at symmetry plane of a duct at $Re = 40000$. ——, Solution at measurement station; – –, fully developed solution. (a): $Ro = 0$; (b): $Ro = 0.22$. (c): $\|\triangle_{FD}\|_{RMS}$ norm of the difference. 81
7.6 Plane contours at different stations along a duct at $Re = 40000$. (a): $Ro = 0$; (b): $Ro = 0.22$. Flow direction toward the observer. 82
7.7 Flow development processes in a finite aspect ratio rotating duct. 83
7.8 Transverse velocity profiles at symmetry plane of a duct at $Re = 40000$ and $Ro = 0.22$. ——, Solution at measurement station; – –, fully developed solution. (a): Coarse mesh; (b): fine mesh. 84
7.9 Plane contours at different stations along a duct at $Re = 40000$ and $Ro = 0.22$. Flow direction toward the observer. 85
7.10 Streamwise velocity profiles at symmetry plane of a duct at $Re = 40000$ and $Ro = 0.22$. ——, Solution at measurement station; – –, fully developed solution. (a): Coarse mesh; (b): fine mesh. (c): $\|\triangle_{FD}\|_{RMS}$ norm of the difference. . 86
7.11 Rotating duct at $Re = 40000$ and $Ro = 0.22$. a): Solution in a y-z plane at $x/h = 300$; (b): solution at $x/h = 320$. Flow direction toward the observer. . 88

7.12 Rotating duct at $Re = 40000$ and $Ro = 0.22$. Contours of streamwise vorticity ω_x in a xz plane at 0.25h from the pressure wall. Light gray contours: $\omega_x > 0.01$; dark gray: $\omega_x < -0.01$. Flow direction toward the right. 89
7.13 Isometric view of the inlet section in the actual duct. 90
7.14 Streamlines at the symmetry plane of the actual rotating duct. (a): $Re = 40000$; (b): $Re = 20000$. 91
7.15 Streamwise vorticity contours at different stations along the actual duct at $Re = 40000$ and $Ro = 0$. Flow direction toward the observer. 92
7.16 Plane contours at different stations along the actual duct at $Re = 40000$ and $Ro = 0.22$. Flow direction toward the observer. 94
7.17 Plane contours at different stations along the straight duct at $Re = 40000$ and $Ro = 0.22$. Flow direction toward the observer. 95
7.18 Plane contours at different stations along the actual duct at $Re = 20000$ and $Ro = 0.22$. Flow direction toward the observer. 96
7.19 Plane contours at different stations along the straight duct at $Re = 20000$ and $Ro = 0.22$. Flow direction toward the observer. 97
7.20 Streamwise velocity profiles at the symmetry plane of a rotating duct at $Ro = 0.22$. ——, Straight duct; — – —, actual duct; – –, fully developed solution. (a): $Re = 40000$; (b): $Re = 20000$. 98
7.21 Streamlines at the symmetry plane of the modified rotating duct. (a): $Re = 40000$; (b): $Re = 20000$. 100
7.22 Plane contours at different stations along the modified duct at $Re = 40000$ and $Ro = 0.22$. Flow direction toward the observer. 101
7.23 Plane contours at different stations along the modified duct at $Re = 20000$ and $Ro = 0.22$. Flow direction toward the observer. 102
7.24 Streamwise velocity profiles at the symmetry plane of a rotating duct at $Ro = 0.22$. ——, Actual duct; — – —, modified duct; – –, fully developed solution. (a): $Re = 40000$; (b): $Re = 20000$. 103

8.1 Unsteady flow in a rotating duct at $Re = 40000$ and $Ro = 0.22$. Flow direction toward the observer. 107
8.2 Plane contours and secondary flow pathlines at $t^* = 500$ in a rotating duct at $Re = 40000$ and $Ro = 0.22$. Flow direction toward the observer. 108
8.3 Streamwise velocity profiles in a rotating duct at $Re = 40000$ and $Ro = 0.22$. (a): ——, 3D unsteady case at $z/h = 0$; – –, 3D steady case at $z/h = 0$. (b): ——, 3D unsteady case at $z/h = 0$; – –, 2D steady case. 109
8.4 Steady state solution in a rotating duct of $AR = \infty$ (periodic length of $6h$ imposed) at $Re = 40000$ and $Ro = 0.22$. Flow direction toward the observer. 110

A.1 2D channel at $Re = 40000$ and $Ro = 0$. (a): Streamwise velocity profile at the center of periodic domain; (b): turbulent viscosity ratio profile at the center of periodic domain. 119
A.2 2D channel at $Re = 40000$ and $Ro = 0$. (a): Turbulent viscosity ratio profile at the center of periodic domain; (b): enlarged view of (a). 120
A.3 2D channel at $Re = 40000$ and $Ro = 0$. (a): Turbulent viscosity ratio profile at the center of periodic domain; (b): enlarged view of (a). 120

B.1 2D modified channel at $Re = 40000$ and $Ro = 0.22$. (a): Streamlines; (b): streamwise velocity profiles at different stations along the channel: — –, Actual channel; — – —, modified channel; – –, fully developed solution. . 123
B.2 2D modified channel at $Re = 40000$ and $Ro = 0.22$. (a): Streamlines; (b): streamwise velocity profiles at different stations along the channel: — –, Actual channel; — – —, modified channel; – –, fully developed solution. . 124
B.3 2D modified channel at $Re = 40000$ and $Ro = 0.22$. (a): Streamlines; (b): streamwise velocity profiles at different stations along the channel: — –, Actual channel; — – —, modified channel; – –, fully developed solution. . 125
B.4 2D modified channel at $Re = 40000$ and $Ro = 0.22$. (a): Streamlines; (b): streamwise velocity profiles at different stations along the channel: — –, Actual channel; — – —, modified channel; – –, fully developed solution. . 126

Chapter 1

Introduction

A good understanding of the effects of rotation on the fine structure of turbulence is of fundamental importance in many engineering applications. Cooling passages of gas turbines, centrifugal separators, radial pumps and compressors are all systems that feature flows in rotating frames of reference. For such flows the centrifugal and Coriolis forces play an active role on the intensity and structure of turbulence.

1.1 Preliminaries

Since the experimental data on turbulent flows in rotating reference frames is quite limited, an ambitious setup has been designed and built in the Experimental Fluid Mechanics Laboratory at Laval University. This unique rig (FIG. 1.1) consists of a 5-meter long rotating rectangular duct of high aspect ratio ($AR = 11$) destined to provide a fully developed two-dimensional flow. The whole unit has been designed to achieve $\Omega = 4$ revolutions/s. The use of a settling chamber at the entrance of the main channel was not considered a worthwhile option because of strong centrifugal forces and size restrictions. Instead, the main channel is preceded by two lateral feeding channels that merge after a 180° turn. The hypotesis behind such a design is that the secondary channels will contribute to "pre-develop" the flow in terms of its z-vorticity and turbulence.
Recent measurements (FIG. 1.2) have shown however that the main flow characteristics at the two most downstream measurements stations (some $80h$ and $135h$ from the main channel inlet, h being the main channel half-width) differ from the DNS results obtained by Alvelius *et al.* (1999). In order to simulate a two-dimensional Poiseuille flow, the

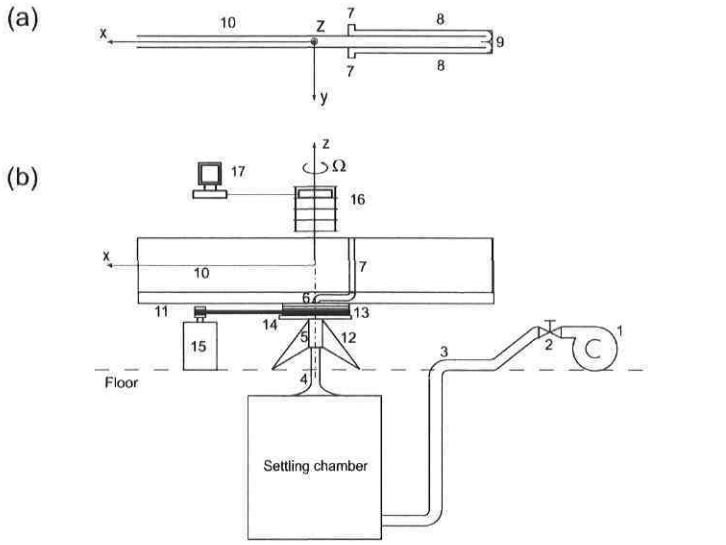

1. Blower
2. Control valve
3. PVC tubing
4. Contraction and pipe
5. Rotating shaft
6. Flow connectors
7. Lateral channels' chambers
8. Lateral channels
9. 180° turns
10. Main channel
11. Support beam
12. Tripod
13. Pulley
14. Disk break
15. AC motor
16. Instruments rotating shelf
17. Control PC computer

Figure 1.1: Experimental setup. (a): top view; (b): side view. From Maciel *et al.* (2003).

authors performed an unsteady calculation on a 3D domain with periodic conditions in the streamwise and spanwise directions. Since in the experimental setup the flow is bounded in the z-direction, it is suspected that complex three-dimensional end-wall effects may affect the flow development and its characteristics.

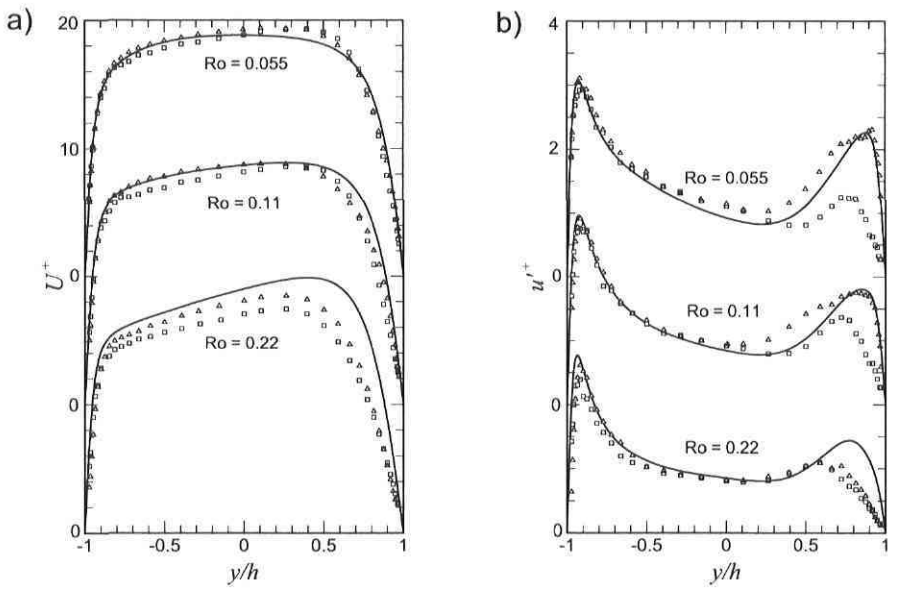

Figure 1.2: Experimental results (Maciel *et al.*, 2003). (a): Mean streamwise velocity profiles at $Re_\tau \approx 180$. $\square, x/h = 80$; $\triangle, x/h = 118$; —, DNS (Alvelius *et al.*, 1999). (b): R.m.s. streamwise velocity fluctuations at $Re_\tau \approx 180$, symbols as in (a).

1.2 Objectives

Based on the aforementioned concerns, the main objectives of the present study can now be formulated:

- *To provide numerical modeling data to better understand the discrepancies between the experimental and DNS results.*
- *To contribute to the identification and understanding of the physical mechanisms responsible for the rotation effects.*
- *To elaborate strategies to promote flow development in the rotating duct.*

1.3 Methodology

In order to satisfy the set goals, 2D and 3D RANS simulations of the flow development in the actual experimental setup have been performed. The domains considered in the present work include only the last portion of the lateral channels, the bends, the merging area and the main channel. Also, to save computer resources, only the upper half section of the channel is modeled and a symmetry plane is applied to the bottom boundary. Commercial codes *Gambit 2.1* and *Fluent 6.1* are employed as mesh generator and flow solver respectively. Turbulence closure is achieved with a RSM model in order to better account for the complex anisotropic effects of rotation on the turbulent structures.
Fully developed solutions of a 2D and 3D rotating channel, obtained through periodic boundary conditions in the streamwise direction, are produced as reference cases. Moreover, they contribute to better understand the end-wall effects for high aspect ratio rotating duct flows. The intensity and dynamic consequences of 3D end-wall structures are examined and the effect of the Reynolds number ($Re = U_b h/\nu$) and the Rotation number ($Ro = 2\Omega h/U_b$) on such flows are also investigated.
Moreover, the flow development in a duct having uniform inlet conditions (mimicking the presence of a settling chamber) is modeled in order to validate the design hypothesis stating that by pre-developing the flow in the two lateral channel, the fully developed state would be reached faster. Finally, many geometrical modifications, aimed at promoting the flow development in the main channel, are numerically tested in both two-dimensional and three-dimensional cases. The feasibility of implementing such devices in the experimental setup are also discussed.

Chapter 2

Theoretical background

It is well known that the Coriolis force, associated with system rotation, plays a fundamental role in the stabilization or destabilization of turbulent shear flows. In the following chapter, the governing equations for an incompressible fluid flow in a rotating reference frame are presented. The non-dimensional parameters governing such flows are identified and flow phenomena are discussed.

2.1 Governing equations

For an incompressible flow in a rotating reference frame subject to constant rotation, the continuity and Navier-Stokes equations can be expressed as:

$$\nabla \cdot \mathbf{u} = 0, \tag{2.1}$$

$$\frac{\partial \mathbf{u}}{\partial t} + \mathbf{u} \cdot \nabla \mathbf{u} = -\frac{1}{\rho}\nabla \mathrm{p} - \boldsymbol{\Omega} \times (\boldsymbol{\Omega} \times \mathbf{r}) - 2\boldsymbol{\Omega} \times \mathbf{u} + \nu \nabla^2 \mathbf{u}. \tag{2.2}$$

The second and third term on the right side of equation (2.2) are the centrifugal and Coriolis forces respectively. The centrifugal force can be expressed as the gradient of a scalar quantity,

$$\boldsymbol{\Omega} \times (\boldsymbol{\Omega} \times \mathbf{r}) = -\nabla \left(\frac{1}{2} \Omega^2 \, \mathrm{r}'^{\,2} \right),$$

where r′ is the distance from the axis of rotation. Hence, by replacing the pressure with the so-called reduced pressure ($p_{red} = p - \frac{1}{2}\Omega^2 \, r'^{\,2}$), the Navier-Stokes equation can be

rewritten in a more compact and non-dimensional form:

$$\frac{\partial \mathbf{u}}{\partial t} + \mathbf{u} \cdot \nabla \mathbf{u} = -\nabla \mathrm{p_{red}} + \frac{1}{\mathrm{Re}} \nabla^2 \mathbf{u} - \mathrm{Ro}\,(\mathbf{\Omega} \times \mathbf{u})\,. \tag{2.3}$$

From equation (2.3), it is apparent that the non-dimensional parameters dictating the fluid flow in a rotating reference frame are the Reynolds number $Re = U_b h/\nu$ and the Rotation number $Ro = 2\,\Omega h/U_b$. Here, U_b represents the bulk velocity and h is the half-width of the channel. A combination of the Reynolds and Rotation number allows to define a new parameter, the Ekman number $E = 1/\,(Re \cdot Ro)$.
Since all computed results in the present study are obtained using a RANS approach (Reynolds Averaged Navier-Stokes), it is relevant to introduce the complete set of N-S equations in a rotating reference frame under this form:

$$\begin{aligned} U\frac{\partial U}{\partial x} + V\frac{\partial U}{\partial y} + W\frac{\partial U}{\partial z} = &-\frac{\partial P}{\partial x} + \frac{1}{Re}\left(\frac{\partial^2 U}{\partial x^2} + \frac{\partial^2 U}{\partial y^2} + \frac{\partial^2 U}{\partial z^2}\right) \\ &-\frac{\partial}{\partial x}\overline{u'^2} - \frac{\partial}{\partial y}\overline{u'v'} - \frac{\partial}{\partial z}\overline{u'w'} + Ro\,\Omega\,V, \end{aligned} \tag{2.4}$$

$$\begin{aligned} U\frac{\partial V}{\partial x} + V\frac{\partial V}{\partial y} + W\frac{\partial V}{\partial z} = &-\frac{\partial P}{\partial y} + \frac{1}{Re}\left(\frac{\partial^2 V}{\partial x^2} + \frac{\partial^2 V}{\partial y^2} + \frac{\partial^2 V}{\partial z^2}\right) \\ &-\frac{\partial}{\partial x}\overline{u'v'} - \frac{\partial}{\partial y}\overline{v'^2} - \frac{\partial}{\partial z}\overline{v'w'} + Ro\,\Omega\,U, \end{aligned} \tag{2.5}$$

$$\begin{aligned} U\frac{\partial W}{\partial x} + V\frac{\partial W}{\partial y} + W\frac{\partial W}{\partial z} = &-\frac{\partial P}{\partial z} + \frac{1}{Re}\left(\frac{\partial^2 W}{\partial x^2} + \frac{\partial^2 W}{\partial y^2} + \frac{\partial^2 W}{\partial z^2}\right) \\ &-\frac{\partial}{\partial x}\overline{u'w'} - \frac{\partial}{\partial y}\overline{v'w'} - \frac{\partial}{\partial z}\overline{w'^2}. \end{aligned} \tag{2.6}$$

In equations (2.4) to (2.6), the variables in capital letters are averaged quantities whereas the lowercase variables with the prime exponent represent the fluctuations around the mean values.

2.2 Flow phenomena in a rotating channel

The rotating plane channel corresponds to a rotating duct of infinite aspect ratio ($AR = \infty$). If one further restricts to 2D flow solutions in a plane channel, one has $W = \partial/\partial z = \partial^2/\partial z^2 = 0$. By looking at equations (2.4) and (2.5), it is apparent then that for a laminar fully developed 2D flow the Coriolis force has no consequences on the

streamwise velocity U. Therefore, the only effect of rotation is to generate a pressure gradient in the direction normal to the flow, equivalent to a hydrostatic pressure field:

$$\frac{\partial p_{red}}{\partial y} = -2Ro\,U. \tag{2.7}$$

However, when a flow transitions to a turbulent state, rotation plays a much more significant role on the flow dynamics. The reason is that, as it will be shown in the next chapter, the Coriolis term appears in the Reynolds stress transport equation.

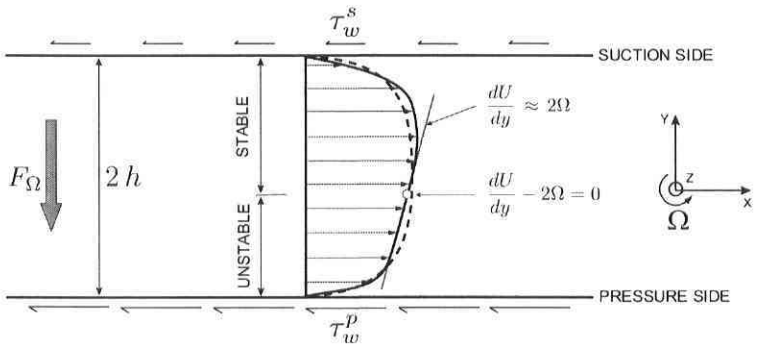

Figure 2.1: Rotating turbulent channel flow. ——, Streamwise velocity profile for $Ro > 0$; - - -, streamwise velocity profile for $Ro = 0$.

Therefore, one can state that system rotation has an indirect effect on the momentum equations through the Reynolds stress tensor. In the schematic of FIG. 2.1, it can be seen that the Coriolis force has three distinct effects on a turbulent Poiseuille flow:

- To create a pressure gradient in the direction normal to the flow.
- To separate the flow in two zones: a region where the intensity of turbulence is increased and a region where turbulence is damped.
- To cause an asymmetry in the streamwise velocity profile (U) and thus, in the shear stresses on the two walls.

The first phenomenon is also present for the laminar case and it simply arises from the necessity to generate a force able to equilibrate the Coriolis force. It is essentially identical to the event that takes place in a bend where a radial pressure gradient must be created to balance the centrifugal force.
The separation of the flow in two distinct regions comes from an inviscid flow analysis (Bradshaw, 1969) stating that conditions leading to instability are locally satisfied when the absolute vorticity $\zeta = -(dU/dy - 2\Omega)$ is negative somewhere in the flow. This criterion predicts stability near the suction side wall, where $dU/dy < 0$, for all positive rotation rates ($\Omega > 0$). For strong rotation rates it is even possible to have

relaminarization of the flow (zero turbulent intensity) along the low-pressure side. Near the pressure side wall the physics is more diverse since for moderate rotation rates (i.e., $dU/dy > 2\Omega > 0$) instabilities can grow, but when the background vorticity (2Ω) is greater than the transverse gradient of the mean velocity, turbulence is once again weakened. A simple manipulation of the stability criterion allows to determine that the critical value of the Rotation number for which the high-pressure side also becomes stabilized is 0.5. The enhancement of the turbulent intensity has a profound effect on the shear stress ($\tau = \mu\, dU/dy - \rho\,\overline{u'v'}$) along the pressure side wall. Along this boundary, the wall shear stress is significantly increased due to the destabilizing effect of the Coriolis force.

As shown in FIG. 2.1, the mean streamwise velocity profile is no longer symmetric when the system has an angular rotation rate. The maximum of the streamwise velocity is shifted toward the suction side since the flow is subject to less "resistance" in this region. It is also observed that in a certain zone the slope of the mean velocity profile is close to the value of the background vorticity, but so far there is no clear explanation in the literature about this behaviour.

2.3 Flow phenomena in a rotating duct

This section presents a discussion of the flow phenomena that occur when the channel is bounded by a lower and upper wall. From now on, a channel with a finite aspect ratio will be called a duct. The analysis will focus only on the upper end of the duct since a symmetry condition exists at the center plane of the domain. As shown in FIG. 2.2, the presence of a wall boundary in the xy plane and the subsequent no-slip condition causes a spanwise variation of the streamwise velocity profile. On the contrary, the transverse pressure gradient is essentially uniform in the spanwise direction. Therefore, near the upper wall boundary the axial velocity is reduced in magnitude and the Coriolis force ($2\Omega \times U$) is no longer sufficient to balance the pressure gradient. This results in the generation of a secondary flow driven in the positive y-direction by the pressure force. The secondary flow is associated with the generation of streamwise vorticity (ω_x). The origin of such vorticity can be understood from the analysis of the laminar vorticity equation in a rotating reference frame:

$$\frac{D\boldsymbol{\omega}}{Dt} = (\boldsymbol{\omega} + 2\boldsymbol{\Omega}) \cdot \nabla \mathbf{u} + \nu \nabla^2 \boldsymbol{\omega}. \tag{2.8}$$

Knowing that the rotation vector ($\boldsymbol{\Omega}$) has only a spanwise component, the vorticity equation in the x-direction becomes:

$$\frac{D\omega_x}{Dt} = \omega_x \frac{\partial U}{\partial x} + \omega_y \frac{\partial U}{\partial y} + (\omega_z + \Omega_z) \frac{\partial U}{\partial z} + \nu \left(\frac{\partial^2 \omega_x}{\partial x^2} + \frac{\partial^2 \omega_x}{\partial y^2} + \frac{\partial^2 \omega_x}{\partial z^2} \right). \tag{2.9}$$

If the analysis is limited to the region near the upper-wall boundary where the secondary flow is generated, equation (2.9) reduces to:

$$\frac{D\omega_x}{Dt} = \Omega_z \frac{\partial U}{\partial z}. \tag{2.10}$$

Equation (2.10) states that the streamwise vorticity, also called the Ekman vorticity, is generated from a rotation of the background vorticity lines which are aligned in the z-direction. The region where the secondary flow is generated is commonly named the

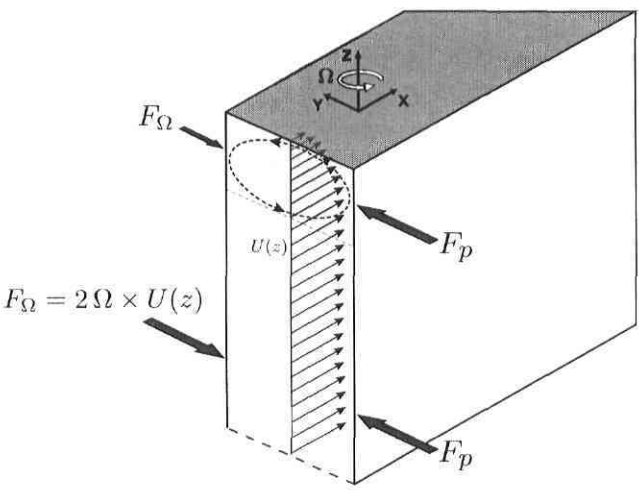

Figure 2.2: Secondary flow generation in a rotating duct.

Ekman layer. As it will be presented later on, the thickness of this layer is function of the Reynolds and Rotation numbers. In the next chapters it will be shown that, even for high aspect ratio ducts, the momentum transport of the secondary flow has a major impact on the streamwise velocity profile at the symmetry plane of the duct. The presence of a secondary flow near the horizontal boundaries is possible even for very low Rotation numbers, but two new mechanisms appear only when the rotation rate increases. The ones discussed here are the generation of longitudinal roll cells (Taylor-Görtler type vortices) and the instauration of the Taylor-Proudman-like regime in turbulent rotating duct flow.

Experimentally, the first observation of roll cells was made by Johnston *et al.* (1972) when they noticed large-scale streamwise structures near the pressure side wall of a rotating duct apparatus. The authors stated that the cell patterns seemed to be 'steady' in the sense that the time period over which a pattern persisted was long relative to the turbulence time scales. However, no truly steady cell pattern was clearly identified. In the paper of Lezius & Johnston (1976), a two-layer model of a turbulent flow is employed to estimate the critical rotation number necessary for the onset of roll cells instabilities. Their study predicts that in fully turbulent flow ($Re > 6000$) the appearance of roll cells structures is essentially independent of the Reynolds number and begins to take place for a Rotation number $Ro \approx 0.02$.

As illustrated in FIG. 2.3, the roll cells instability appears under the form of counter-rotating longitudinal vortex pairs. These vortical structures induce a velocity that, between the positive and negative members of each vortex pair, sweeps the fluid particles away from the pressure side of the duct. On the contrary, between counter-rotating pairs they draw the flow toward the pressure wall. This transport has a noticeable effect on the streamwise velocity and turbulent activity across the duct. The DNS data of Kristoffersen & Andersson (1993) supports the fact that the number of vortex pairs in a given duct must be an integer N. By assuming that the vortices are circular and that they occupy half the cross-section, one can estimate the number of pairs in the duct as:

$$N = int\left(\frac{H}{2h}\right), \tag{2.11}$$

where H is the height of the duct (i.e., $H/2h = AR$). However, the shape and size of the roll cells may vary for different Reynolds and Rotations numbers. Generally, the number of vortex pairs tends to increase with Ro, and the wavelength (λ) of a pair of roll cells approaches $2h$ at high rotation rates ($Ro \approx 0.2$), as suggested in FIG. 2.3. The aspect ratio is another parameter affecting the preferred wavelength of the vortices and, in certain cases, may prevent their formation.

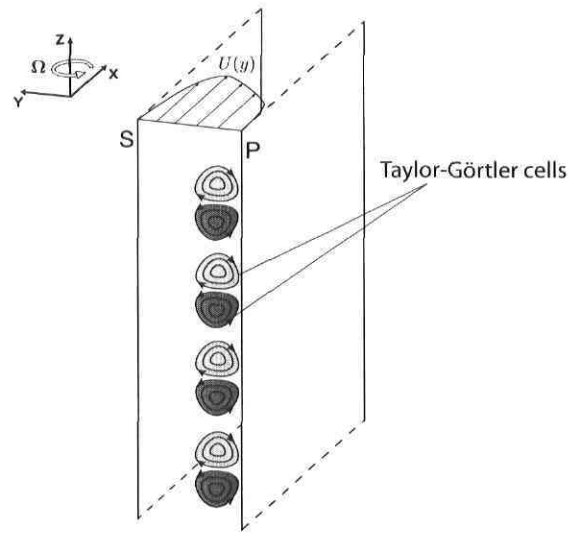

Figure 2.3: Roll cells instability in rotating duct flow. Light gray contours: $\omega_x > 0$; dark gray: $\omega_x < 0$.

When the rotation rate of the duct is further increased (i.e., $Ro > 0.5$), it leads to a restabilization of the flow toward a Taylor-Proudman-like regime. The direct consequence is a decrease of the turbulent intensity near the pressure side wall and the disappearance of the roll cells. This phenomenon is predicted by the displaced particle analysis of Tritton (1992) which states that the flow is stabilized everywhere in the duct for high enough rotation rates ($|S| = -2\Omega/\omega_z > 1$). This analysis assumes an inviscid flow, but it is reasonable to suppose that for a viscous flow, the restabilization

will occur at lower rotation rates than those theoretically predicted.
The Taylor-Proudman-like regime is characterized by a region in the spanwise direction where the flow is two-dimensional ($\partial/\partial z = 0$). The complete derivation of the Taylor-Proudman theorem can be found in Tritton (1988), and thus only the main features are discussed here. The first hypothesis is that in equation (2.2) the Coriolis term is large compared to both inertia and viscous terms (i.e., $Ro \gg 1$ and $E \ll 1$). The steady state equation of motion thus reduces to:

$$2\boldsymbol{\Omega} \times \mathbf{u} = -\frac{1}{\rho}\nabla \mathrm{p}. \tag{2.12}$$

Such flow is called geostrophic. An important characteristic of this type of flow is that the pressure gradient is normal to the flow direction and therefore the pressure is constant along a streamline. Another feature of a geostrophic flow can be found by applying the curl operator to equation (2.12)

$$\nabla \times (2\boldsymbol{\Omega} \times \mathbf{u}) = 0. \tag{2.13}$$

The expansion of the curl gives

$$\boldsymbol{\Omega} \cdot \nabla \mathbf{u} - \mathbf{u} \cdot \nabla \boldsymbol{\Omega} + \mathbf{u}(\nabla \cdot \boldsymbol{\Omega}) - \boldsymbol{\Omega}(\nabla \cdot \mathbf{u}) = \mathbf{0}. \tag{2.14}$$

Since Ω is a constant, the second and third terms are zero and the last term is also nul because of the continuity condition. If the axis of rotation is chosen in the z-direction, equation (2.14) becomes

$$\Omega \frac{\partial \mathbf{u}}{\partial \mathrm{z}} = 0. \tag{2.15}$$

Hence, there is no variation of the velocity field in the spanwise direction and it corresponds, by definition, to a two-dimensional flow. It is important to mention that the solution of a rotating duct in a Taylor-Proudman-like regime will not necessarily correspond to the theoretical 2D solution of a rotating channel since the secondary flow due to end effects may play an important role.

2.4 Flow phenomena in a bend

The generation of a secondary flow in a bend is a well known subject and is treated in many textbooks. The topic is discussed here since in the experimental setup (Maciel *et al.*, 2003), that we wish to model in the present study, the main channel is preceded by two lateral feeding channels that merge after a 180° turn. As shown in FIG. 2.4, a pressure gradient is generated in the radial direction (normal to streamlines curvature) in order to counteract the centrifugal force. However, near the top wall, the no-slip

condition imposes a velocity gradient in the spanwise direction. The reduction of the streamwise velocity in this region directly affects the magnitude of the centrifugal force, which is now unable to balance the established radial pressure force. Consequently, a secondary flow is generated. Its presence increases the dissipative losses in the duct since slow moving fluid is convected from the wall into the main flow and, by continuity, high-energy fluid is moved toward the wall.

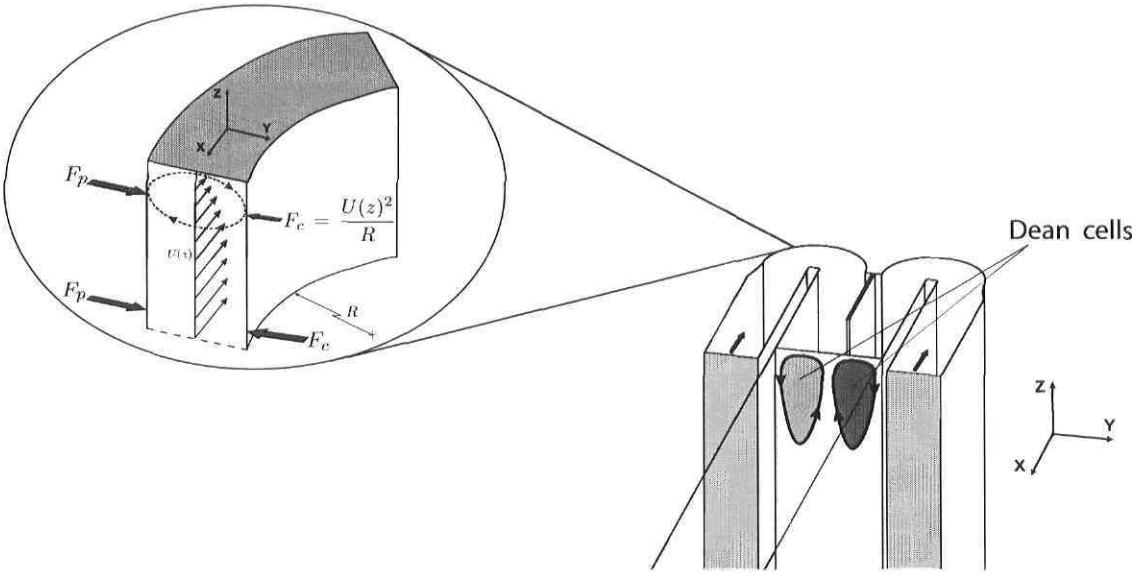

Figure 2.4: Details of the experimental setup configuration. Secondary flow generation in a bend (Dean-type cells).

In the configuration of this experimental setup, two 180° bends are present and one expects to find two counter-rotating vortices in the entrance region of the main duct, as sketched on FIG. 2.4. Moreover, when the rig is subjected to rotation, the centrifugal vortices should strongly interact with the Ekman vortex associated to the end wall and the Coriolis force.

Chapter 3

Numerical method

The present numerical study of turbulent flows in rotating ducts is based on the solution of the Reynolds Averaged Navier-Stokes equations in conjunction with a Reynolds Stress Model for turbulence closure.
The following chapter provides a brief justification for the choice of this particular method as well as a detailed characterisation of the turbulence model and wall treatment. The basic features of the commercial finite volume code *Fluent v6.1.22* are also discussed.

3.1 *Fluent*: a finite volume solver

Fluent is a commercial finite volume (FV) solver that has been used at the LMFN ("Laboratoire de Mécanique des Fluides Numérique") over the past several years. The code has proven its accuracy and reliability in many problems varying from the unsteady flow around an oscillating wing to the flow around a passenger vehicle. Moreover, *Fluent* has the capability to analyze physical phenomenon involving turbulence, compressible effects, heat transfer and chemical reactions. As mentioned above, *Fluent* is a finite volume code that uses the integral form of the conservation and transport equations to solve for all quantities at the center of each control volume (CV). For a given variable (ϕ), and assuming that the velocity field and fluid properties are known, this yields:

$$\oint \rho\phi\,\mathbf{u}\cdot\mathbf{n}\,dA = \oint \Gamma_\phi \nabla\phi\cdot\mathbf{n}\,dA + \int_V q_\phi\,dV, \tag{3.1}$$

where Γ_ϕ is the diffusion coefficient for ϕ and q_ϕ is a source term. Since convective and diffusive fluxes at the CV faces are also needed, an interpolating scheme must be

used. Finite volume methods can be adapted to any type of grid and this makes them suitable for complex geometries. A disadvantage of FV methods, compared to finite difference schemes, is that they require three levels of approximation (interpolation, differentiation and integration). This feature makes it difficult to develop higher than second order discretization schemes in 3D (Ferziger & Peric, 1992).
The solver version employed in the present study is *Fluent v6.1.22* and all meshes are generated using *Gambit v2.1.6*.

3.2 RANS approach to turbulent flows

It is well known in the CFD community that the most accurate approach to turbulence simulation is to completely solve the Navier-Stokes equations without averaging or approximation. This approach is called direct numerical simulation (DNS). In a DNS computation, all turbulent scales are captured and all fluid motions are resolved. This implies an unsteady calculation and a three-dimensional flow field. Moreover, a valid direct numerical simulation requires that each dimension of the domain must be at least a few times the scales of the largest turbulent eddies (L), and that the mesh discretization is fine enough to capture the smallest scales on which the viscosity is active (the Kolmogoroff length scale, η). A quick estimation gives that the minimum number of cells required in each direction is L/η. In their book, Tennekes and Lumley (1976) have shown that this ratio is proportional to $Re^{3/4}$. Since the time step is related to the mesh size, the total cost of a DNS computation is proportional to Re^3. With the current computer performance, it is easy to comprehend why DNS is only used to solve simple flow geometries at low Reynolds numbers ($Re \approx 10^3$). Because the present numerical study involves an elaborate geometry and turbulent flows at $Re > 10^4$, the DNS approach did not appear as a viable option.
A second approach to turbulent flows is large eddy simulation (LES). The fundamental principle behind this method is that the small scales are much weaker and provide little transport of conserved properties compared to the large scales. LES still remains a time dependent three-dimensional computation but it requires a much smaller number of grid points since all small eddies are now modeled, and only large eddies are simulated. This explains why LES is becoming increasingly popular among CFD users (mainly among scientists still today). However, large eddy simulations are often run on powerful cluster machines and, depending on the flow complexity, they still require days in terms of computing time. As mentioned in the introduction, several geometries at various flows regimes have to be tested in the current study and the LES approach thus appears too demanding for the present purposes.
The arguments mentioned above justify the use of a RANS method where the smaller

time scales in the flow are regarded as part of turbulence and can thus be averaged. In a statistically steady flow, the velocity and pressure fields can be expressed as the sum of a time-averaged value and a time-varying fluctuation about that value:

$$\mathbf{u}(\mathbf{x}, \mathrm{t}) = \mathbf{U}(\mathbf{x}) + \mathbf{u}'(\mathbf{x}, \mathrm{t}),$$

$$\mathrm{p}(\mathbf{x}, \mathrm{t}) = \mathrm{P}(\mathbf{x}) + \mathrm{p}'(\mathbf{x}, \mathrm{t}).$$

If the flow is unsteady, time averaging cannot be applied and it is replaced by ensemble averaging. When this decomposition and averaging process is applied to the Navier-Stokes equations, it yields the Reynolds Averaged Navier-Stokes equations ((2.4) to (2.6)). It is easily verified that the number of unknowns is greater than the number of equations. In order to have a closed set of equations, it is necessary to introduce a turbulence model. Many models have been developed over the years and they can be divided in two categories: eddy-viscosity models and Reynolds stress models. The former are based on the Boussinesq hypothesis stating that the Reynolds stresses can be approximated as follows:

$$-\rho\overline{u_i' u_j'} = \mu_t \left(\frac{\partial U_i}{\partial x_j} + \frac{\partial U_j}{\partial x_i} \right) - \frac{2}{3}\rho\delta_{ij}k\,, \tag{3.2}$$

where k is the turbulent kinetic energy:

$$k = \frac{1}{2}\overline{u_i' u_i'}.$$

With this type of turbulence modeling, the RANS equations have the same form as the Navier-Stokes equations except that the molecular viscosity is now replaced with an *effective* viscosity $\mu_{eff} = \mu + \mu_t$. Many models have been developed in order to evaluate the eddy viscosity (μ_t) but the most popular are $k-\epsilon$, $k-\omega$, and Spalart-Allmaras models. The great advantage of the eddy viscosity models is that they are easy to implement in a computer code and they perform relatively well when the hypothesis of local equilibrium is respected (e.g., zero pressure gradients boundary layers). However, in many cases, this assumption is not valid and such models cannot be employed accurately.

The second and more elaborate approach to RANS turbulence modeling is a second order closure scheme. This method gives a more complete description of the energy exchange between the mean flow and the turbulence. Moreover, it has the great advantage of taking into account the anisotropy of turbulence. The Reynolds Stress Model (RSM) belongs to this category and its transport equations can be derived from the

Navier-Stokes equations (2.2) as follows (from Mårtensson, 2004):

$$\overbrace{\frac{\partial \overline{u_i' u_j'}}{\partial t} + U_k \frac{\partial \overline{u_i' u_j'}}{\partial x_k}}^{C_{ij}} = \overbrace{-\left(\overline{u_i' u_k'} \frac{\partial U_j}{\partial x_k} + \overline{u_i' u_k'} \frac{\partial U_j}{\partial x_k}\right)}^{P_{ij}} + \overbrace{\overline{\frac{p'}{\rho}\left(\frac{\partial u_i'}{\partial x_j} + \frac{\partial u_j'}{\partial x_i}\right)}}^{\Phi_{ij}}$$

$$+ \underbrace{\frac{\partial}{\partial x_k}\left(\nu \frac{\partial \overline{u_i' u_j'}}{\partial x_k}\right)}_{D_{ij}} - \underbrace{\frac{\partial}{\partial x_k}\left(\overline{u_i' u_j' u_k'} + \overline{\frac{p'}{\rho}\left(u_i' \delta_{jk} + u_j' \delta_{ik}\right)}\right)}_{T_{ij}} \tag{3.3}$$

$$- \underbrace{2\nu \overline{\frac{\partial u_i'}{\partial u_j'} \frac{\partial u_j'}{\partial x_k}}}_{\epsilon_{ij}} - \underbrace{\Omega_k \left(\overline{u_j' u_m'} \epsilon_{ikm} + \overline{u_i' u_m'} \epsilon_{jkm}\right)}_{R_{ij}},$$

where

$C_{ij} \equiv$ Convection
$P_{ij} \equiv$ Production
$\Phi_{ij} \equiv$ Pressure strain
$D_{ij} \equiv$ Molecular diffusion
$T_{ij} \equiv$ Turbulent diffusion
$\epsilon_{ij} \equiv$ Dissipation
$R_{ij} \equiv$ Redistribution due to the Coriolis force.

Of the numerous terms of equation (3.3), C_{ij}, P_{ij} D_{ij} and R_{ij} can be solved directly. However, T_{ij}, Φ_{ij} and ϵ_{ij} need to be modeled in terms of computed quantities in order to have a closed set of equations.
The turbulent diffusion term is approximated with the generalized gradient-diffusion model of Shir (1973):

$$T_{ij} = \frac{\partial}{\partial x_k}\left(\frac{C_\mu}{\sigma_k} \frac{k^2}{\epsilon} \frac{\partial \overline{u_i' u_j'}}{\partial x_k}\right), \tag{3.4}$$

where $C_\mu = 0.09$ and $\sigma_k = 0.82$.
Fluent v6.1.22 offers an optional SSG model proposed by Speziale, Sarkar and Gatski (1991) in order to calculate the pressure-strain term. This approach is a variant of the standard linear pressure-strain model (Gibson and Launder, 1975) and it has demonstrated to provide superior accuracy for rotating shear flows and complex engineering flows where streamline curvature is present. The SSG model, also called the quadratic

pressure-strain model (QPS), is defined as follows:

$$\begin{aligned}\Phi_{ij} = &-\left(C_1\epsilon + C_1^* P\right) b_{ij} + C_2\,\epsilon\left(b_{ik}b_{kj} - \frac{1}{3}b_{mn}b_{mn}\delta_{ij}\right)\\ &+\left(C_3 - C_3^*\sqrt{b_{ij}b_{ij}}\right) kS_{ij}\\ &+C_4\,k\left(b_{ik}S_{jk} + b_{jk}S_{ik} - \frac{2}{3}b_{mn}S_{mn}\delta_{ij}\right) + C_5\,k\left(b_{ik}\omega_{jk} + b_{jk}\omega_{ik}\right),\end{aligned} \tag{3.5}$$

where

$$\begin{aligned}P &= \tfrac{1}{2}P_{kk}\\ b_{ij} &= -\left(\frac{-\overline{u_i'u_j'} + \frac{2}{3}k\delta_{ij}}{2k}\right)\\ S_{ij} &= \tfrac{1}{2}\left(\frac{\partial u_j}{\partial x_i} + \frac{\partial u_i}{\partial x_j}\right)\\ \omega_{ij} &= \tfrac{1}{2}\left(\frac{\partial u_i}{\partial x_j} - \frac{\partial u_j}{\partial x_i}\right),\end{aligned}$$

and the constants are (from *Fluent 6.1* documentation):

$C_1 = 3.4;\ C_1^* = 1.8;\ C_2 = 4.2;\ C_3 = 0.8;\ C_3^* = 1.3;\ C_4 = 1.25;\ C_5 = 0.4.$

Assuming the isotropy of the dissipative structures, which is plausible far from the solid boundaries at high Reynolds number, the dissipation rate can be modeled as:

$$\epsilon_{ij} = \frac{2}{3}\,\epsilon\,\delta_{ij}. \tag{3.6}$$

The scalar dissipation ϵ is computed from a transport equation,

$$\frac{\partial \epsilon}{\partial t} + \epsilon\frac{\partial u_i}{\partial x_i} = \frac{\partial}{\partial x_j}\left(\left(\nu + \frac{\nu_t}{\sigma_\epsilon}\right)\frac{\partial \epsilon}{\partial x_j}\right) + \frac{1}{2}C_{\epsilon 1}P_{ii}\frac{\epsilon}{k} - C_{\epsilon 2}\frac{\epsilon^2}{k}, \tag{3.7}$$

where $\sigma_\epsilon = 1.0;\ C_{\epsilon 1} = 1.44;\ C_{\epsilon 2} = 1.92.$

As for all differential equations, boundary conditions are required for each equations. This subject is discussed in the next section.

3.3 Wall treatment

Turbulent flows are greatly affected by the presence of walls. Numerous experiments have shown that the near-wall region can be divided into three separate layers: the viscous sublayer, the buffer layer and the fully turbulent layer (see FIG. 3.1). Very close to the wall (i.e., viscous sublayer), the molecular viscosity of the fluid plays an important role in damping the velocity fluctuations. Further from the solid boundaries (i.e., fully turbulent region), the turbulence intensity increases rapidly due to the large velocity gradients. An accurate representation of the near-wall region is critical to the

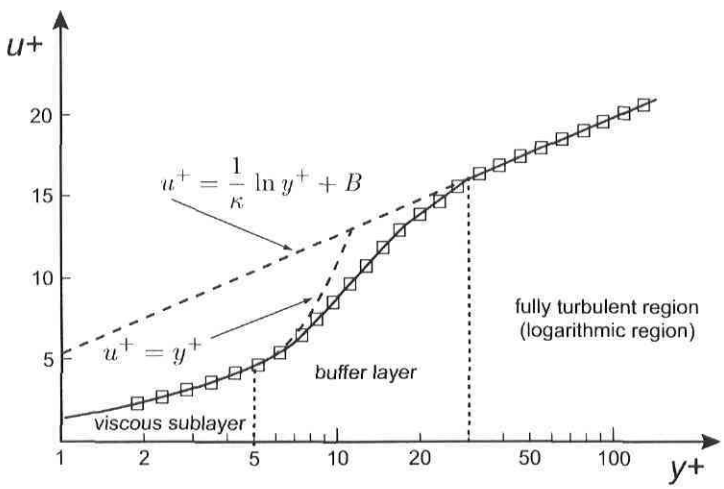

Figure 3.1: Velocity profile as a function of distance normal to the wall. □, Experimental data; - - -, wall functions. From Ferziger & Perić, 2002.

overall flow solution. In CFD, the conditions at solid boundaries can be treated in two separate ways. The first and more direct method is to solve the equations accurately up to the wall and apply the usual no-slip conditions for the velocity. For the Reynolds stresses and the dissipation, "low-Reynolds models" are often used in order to properly damp turbulence in the viscous sublayer. The setback with this approach is that, at high Reynolds number, the viscous sublayer becomes very thin and many grid cells are necessary in order to well resolve it. The alternative is to use a wall function. This approach relies on the existence of an expected logarithmic region in the velocity profile such that:

$$u^+ = U/u_\tau = \frac{1}{\kappa} \ln y^+ + B, \tag{3.8}$$

where κ is the von Karman constant ($\kappa = 0.41$), B is an empirical constant (B$\approx$ 5.45) and y^+ is the normalized wall distance:

$$y^+ = \frac{\rho u_\tau y}{\mu}. \tag{3.9}$$

In equation (3.9), u_τ is the friction velocity ($u_\tau = \sqrt{\tau_w/\rho}$) and y is the normal distance to the nearest wall. The standard wall function in *Fluent* is based on the proposal of

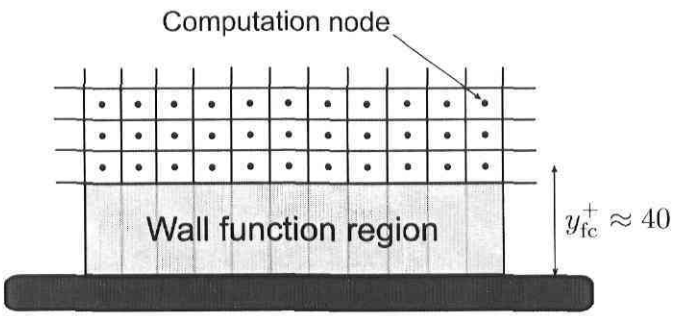

Figure 3.2: Wall function approach.

Launder and Spalding (1974) and is employed whenever the first cell has a $y_{\text{fc}}^+ > 11.225$. From equation (3.8), and assuming that the flow is in local equilibrium (i.e., production and dissipation of turbulence are equal), one can show that $u_\tau = C_\mu^{1/4}\sqrt{k}$. The expression for the mean velocity at the first grid point can thus be written as:

$$U_{\text{fc}} = u^+ u_\tau = \left(\frac{1}{\kappa}\ln y_{\text{fc}}^+ + B\right) C_\mu^{1/4} k^{1/2}, \tag{3.10}$$

where $C_\mu = 0.09$. The production of turbulent kinetic energy (k) in the wall region is computed from:

$$P_k \approx \tau_w \frac{\partial U_{\text{fc}}}{\partial n} = \tau_w \frac{C_\mu^{1/4} k^{1/2}}{\kappa\, y_{\text{fc}}}. \tag{3.11}$$

The dissipation at the wall-adjacent cells is obtained assuming, once again, local equilibrium:

$$\epsilon = \frac{C_\mu^{3/4} k^{3/2}}{\kappa\, y_{\text{fc}}}. \tag{3.12}$$

Finally, the near-wall values of the Reynolds stresses are derived from the wall functions:

$$\frac{\overline{u_\tau'^2}}{k} = 1.098, \quad \frac{\overline{u_\eta'^2}}{k} = 0.247, \quad \frac{\overline{u_\lambda'^2}}{k} = 0.655, \quad \frac{\overline{u_\tau' u_\eta'}}{k} = 0.255, \tag{3.13}$$

where, in a local coordinate system, the index τ represents the tangential coordinate, η the normal coordinate and λ the binormal one. To evaluate the turbulent kinetic energy at the wall-adjacent cells, the k transport equation must be solved:

$$\frac{\partial k}{\partial t} + \frac{\partial}{\partial x_i}(u_i\, k) = \frac{\partial}{\partial x_j}\left(\left(\nu + \frac{\nu_t}{\sigma_k}\right)\frac{\partial k}{\partial x_j}\right) + \frac{1}{2}P_{ii} - \epsilon, \tag{3.14}$$

where $\sigma_k = 0.82$. Even though the values of k are only needed in the cells contiguous to the wall, equation (3.14) is solved in the entire domain for computational convenience. It is relevant to mention that the standard wall function is valid when the first grid

point is situated in the logarithmic region (i.e., $y_{fc}^{+} > 30$). However, the optimal range is comprised between $y_{fc}^{+} = 30$ and 60 (FIG. 3.2). In problems where the equilibrium hypothesis is not valid (e.g., separated flows), the standard wall functions become less reliable and the user should verify that such flow regions do not exist over a large portion of the domain. In the case of rotating duct flows, the Coriolis force can cause the velocity profile to depart from the standard logarithmic behavior, especially near the suction wall. The validity of using a wall function approach in rotating flows is discussed in section 4.1.

3.4 Numerical schemes

All numerical results are obtained with a segregated type solver where the governing equations (continuity, momentum and turbulent quantities) are solved sequentially within a given loop. Since the governing equations are non-linear and coupled, many iterations of the solution loop must be performed before a converged solution is obtained. In addition, the non-linear equations have to be linearized. The linearization method is "implicit" due to the fact that, for a given variable, the unknown value in each cell is computed using a relation that implies both existing and unknown values from neighbouring cells. This results in a system of linear equations with one equation for each cell in the domain. *Fluent* employs an iterative Gauss-Seidel linear equations solver in conjunction with an algebraic multigrid (AMG) method to solve for the dependent variable in the system of equations. In the following section, the main features of the discretization schemes are addressed since they have a significant impact on the accuracy of the solution.
In order to reduce numerical diffusion and achieve a higher degree of precision, a second order upwind scheme is chosen. In *Fluent*, this scheme uses a multidimensional linear reconstruction approach where the values at the cell face (see FIG. 3.3) are obtained through a Taylor series expansion of the cell-centered solution about the cell centroid:

$$\phi_e = \phi_P + \nabla\phi_P \cdot \Delta\mathbf{s} \tag{3.15}$$

where $\Delta\mathbf{s}$ is the displacement vector from the upstream cell centroid (P) to the face centroid (e), and the gradient $\nabla\phi$ is computed using the Green-Gauss theorem. In all simulations performed here, the second order scheme is selected for momentum, turbulent kinetic energy, turbulent dissipation rate and Reynolds stress equations.
Diffusion terms are always discretized using a central difference scheme that provides second order accuracy.
The remaining variable to be calculated is the pressure. Since the momentum equations are already employed to determine the velocity components, the only equation allowing

to solve for pressure is the continuity condition. Unfortunately, for incompressible flows the latter does not contain any pressure term and therefore some manipulations are required. The most common method is to take the divergence of the momentum equation and to apply the continuity condition in order to simplify certain terms. The result is a Poisson equation for pressure:

$$\frac{\partial}{\partial x_i}\left(\frac{\partial p}{\partial x_i}\right) = -\frac{\partial}{\partial x_i}\left(\frac{\partial\left(\rho u_i u_j\right)}{\partial x_j}\right). \tag{3.16}$$

Equation (3.16) is coupled with the momentum equation and is solved using the PRESTO! scheme (pressure staggering option). This particular model is recommended for rotating flows and flows in strongly curved domains. Since both of these conditions are met in the present study, the PRESTO! model is the preferred pressure interpolation scheme.

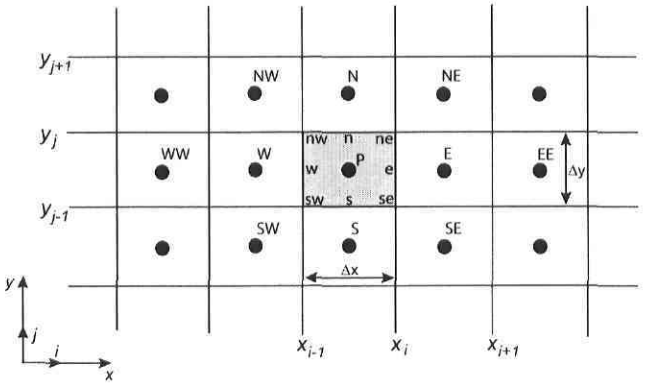

Figure 3.3: Finite volume approach for a Cartesian 2D grid. From Ferziger & Peric, 1992.

In order to guarantee that the pressure and velocity fields satisfy the momentum and continuity equations, a "correction method" has to be used. With this approach, the velocity and pressure fields computed from the linearized momentum equations are taken as provisional and a correction is applied to them in order to enforce the conservation law. When this procedure is applied to equation (3.16), it yields a pressure-correction equation. Many options are available for solving this latter equation, but the approach chosen here is the SIMPLEC algorithm (van Doormal and Raithby, 1984).

Chapter 4

Validation efforts

Before modeling the experimental setup, many numerical tests are performed on much simpler configurations in order to validate the CFD code for flows in rotating channels. The present investigation will demonstrate the ability of the RSM model, and its wall function, to capture the effects of rotation on turbulence. The soundness of the boundary conditions and their ability to mimic the experimental conditions are also asserted.

4.1 Validation of the turbulence model and wall treatment

As it was stated in the previous chapter, the second order closure schemes are expected to be a more accurate approach to turbulence modeling than the simpler and cheaper first order counterparts. The great advantage of using a Reynolds Stress Model (RSM) is that the rotation effects are implicit in the model without any adjustment or correction.

The present validation of the Reynolds Stress Model is done by running a simulation of a fully developed turbulent flow in a non-rotating and rotating channel, and by comparing the results with the DNS calculations of Alvelius *et al.* (1999). Moreover, two meshes of different size are used in order to assert the mesh independence of the solution. The coarse grid has 80 elements in the streamwise direction (x-direction) and 35 in the transverse direction (y-direction), uniformely distributed (see FIG. 4.1). The refined grid has the same discretization in the streamwise direction and 51 cells in the transverse direction. Since a wall function is employed in the near-wall region, the size of the wall-adjacent cell is set to $y_{\mathrm{fc}}^{+} \approx 40$ which does not correspond to the

same physical size on each side of the rotating channel. The domain has a length of $10h$ and a width of $2h$, where h is the half-width of the channel. Periodic conditions are applied at the inlet and outlet boundaries while a prescribed flowrate is imposed in the x-direction. The domain length and streamwise discretization are chosen in order to guarantee a $\partial/\partial x = 0$ (fully developed condition) along the channel. One should

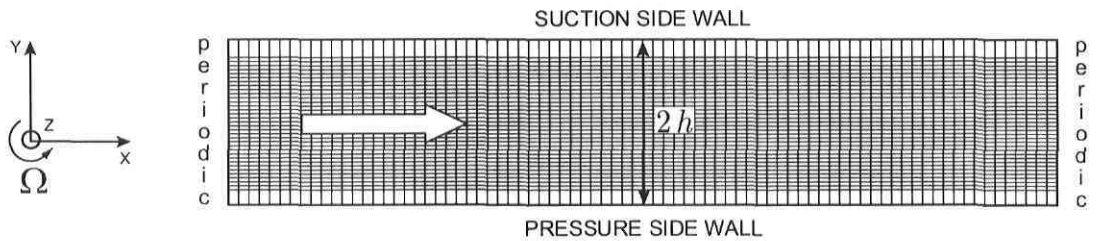

Figure 4.1: Coarse mesh for rotating case.

note that the periodic conditions only imply that the solution at the two boundaries must be identical, and therefore, an evolution along the domain is allowed. However, it is reasonable to expect a uniform solution in the streamwise direction under such conditions. Further information about this issue is presented in Appendix A.
TABLE 4.1 and 4.2 compare the predicted $Re_\tau = u_\tau h/\nu$ values on the suction and pressure side walls of the channel. This parameter represents a ratio between the turbulent

	Re_τ^s	Re_τ^p	Re_τ
RANS (coarse mesh)	351.5	351.5	351.5
RANS (fine mesh)	351.9	351.9	351.9
DNS (Alvelius)	358.7	359.3	359.0

Table 4.1: Comparaison of non-rotating case - $Re = 6210$.

and viscous transport and allows to evaluate the validity of the turbulence modeling in the near-wall region. The values of Re_τ listed in TABLE 4.1 as well as the profiles plotted in FIG. 4.3a indicate that, without system rotation, the solution is symmetric and the RANS modeling is able to capture relatively well the near-wall behaviour (about 2% on Re_τ). Predictions are particularly good for the $\overline{u'v'}$ stress component,

	Re_τ^s	Re_τ^p	Re_τ
RANS (coarse mesh)	306.1	415.2	360.7
RANS (fine mesh)	305.8	416.2	361.0
DNS (Alvelius)	279.9	426.6	353.3

Table 4.2: Comparaison of rotating case - $Re = 6899$ at $Ro = 0.2$.

which is the only non-vanishing Reynolds stress term in the x-momentum equation. When system rotation is present, the symmetry is broken and the velocity profile shows a central region of near constant slope ($dU/dy = 2\Omega$). The RANS predictions match fairly well with the DNS results of Alvelius *et al.* (1999) even though the estimates on the suction (stabilized) side are less accurate. These results are not surprising since turbulence is damped in this portion of the channel and there is a deviation from the standard log-like behaviour. The computations of Kristoffersen & Andersson (1993) illustrate this phenomenon (FIG. 4.2). It is interesting to notice that for high Rotation

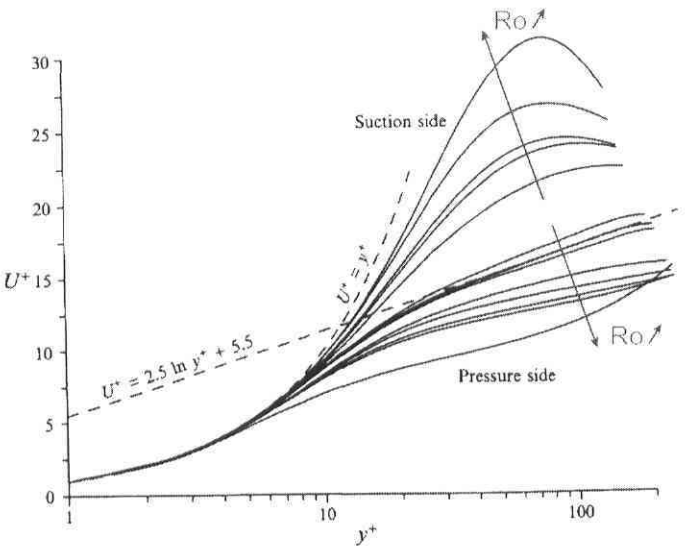

Figure 4.2: Mean velocity profiles in wall coordinates for different rotation rates ($0 \leq Ro \leq 0.50$) at $Re = 2900$. From Kristoffersen & Andersson, 1993.

numbers, the mean velocity profile near the suction side has a more laminar-like shape and approaches the linear law $u^+ = y^+$. Normally, for such low Reynolds number flows, the wall function approach would not be necessary but, for the moment, *Fluent* does not offer an efficient wall damping model.

In the present study, the Reynolds number will vary between 10000 and 40000 and it is expected that the wall function will perform better since the existence of a logarithmic region in the velocity profile is formally verified for an infinite Reynolds number.

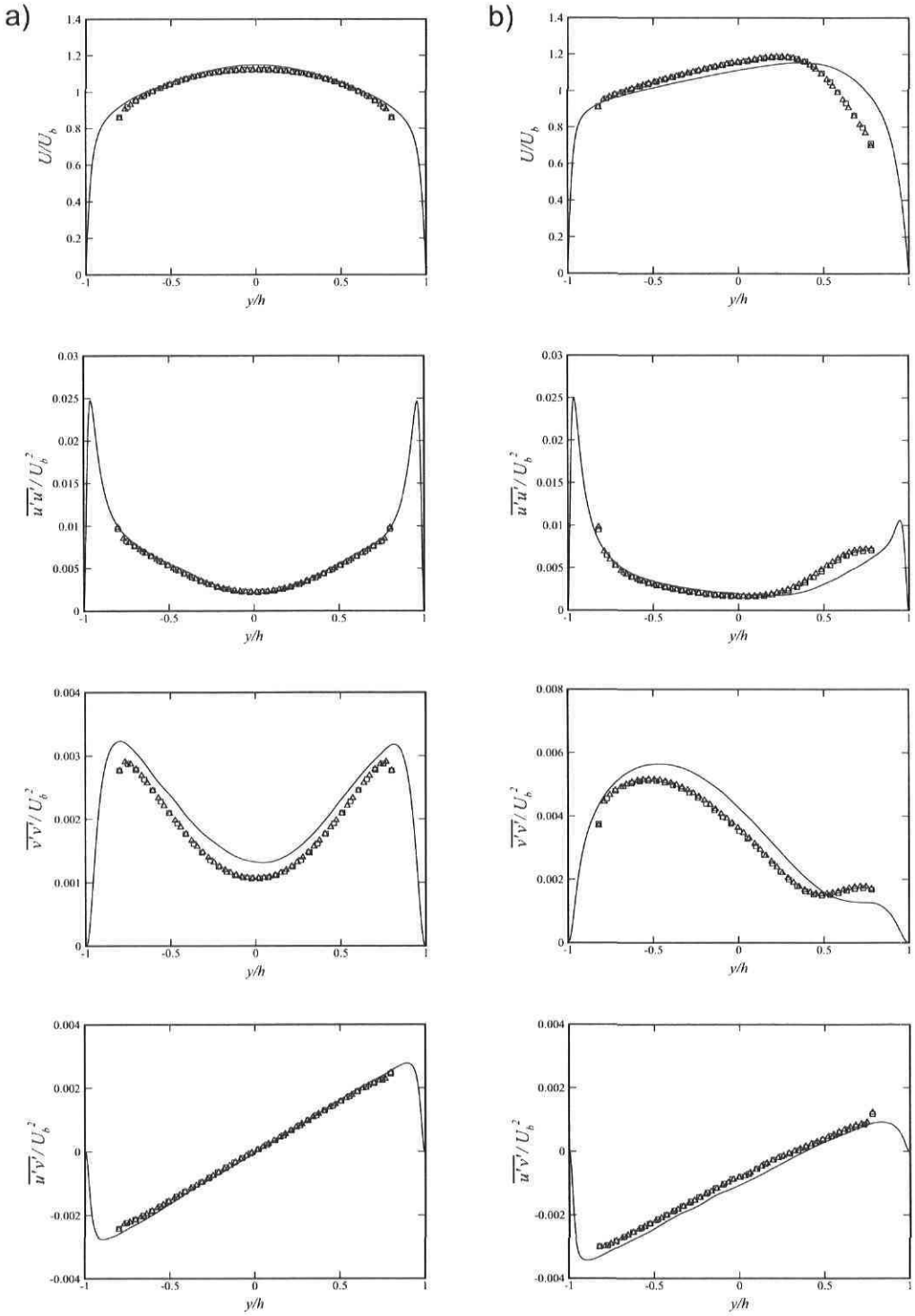

Figure 4.3: Normalized mean velocity profiles and Reynolds stress components. □, Coarse mesh; △, fine mesh; ——, DNS by Alvelius. (a): $Re = 6210$ at $Ro = 0$; (b): $Re = 6899$ at $Ro = 0.20$.

4.2 Validation of the boundary conditions

In the finite volume method, each CV provides an algebraic equation but the fluxes through the faces located along the domain boundaries require a special treatment. Those fluxes must be known or have to be a combination of interior values and boundary data. *Fluent* offers a variety of boundary conditions for both the inlet and exit boundaries, but only a few are mentioned here below:

- Inlet conditions: *velocity inlet, pressure inlet, mass flow inlet*
  - **Velocity inlet**: allows to define the flow velocity, along with all relevant scalar properties of the flow. The total (or stagnation) properties of the flow are not fixed, so they will rise to whatever value is necessary to provide the prescribed velocity distribution.
  - **Pressure inlet**: allows to define the fluid total pressure at flow inlets, along with all other scalar properties of the flow. They are suitable for both incompressible and compressible flow calculations and can be used even if the flow rate and/or velocity is not known.
  - **Mass flow inlet**: provides a prescribed mass flow rate or mass flux distribution at an inlet. It is often used when it is more important to match a prescribed mass flow rate than to match the total pressure of the inflow stream.
- Exit conditions: *outflow, pressure outlet*
  - **Outflow**: allows to model flow exits where the details of the flow velocity and pressure are not known prior to solution of the flow problem. No conditions are specified by the user at outflow boundaries but a zero normal diffusion flux is assumed.
  - **Pressure outlet**: requires the specification of a uniform static pressure at the outlet boundary.
- Wall boundary conditions: used to separate fluid and solid regions. In viscous flows, the no-slip boundary condition is enforced by default, but a tangential velocity component in terms of the translational or rotational motion of the wall can also be specified.
- Symmetry conditions: useful when the physical geometry of interest and the flow patterns have mirror symmetry. This condition can also be used to model zero

shear slip walls in viscous flows. A symmetry conditions assumes zero convective and diffusion fluxes across the boundary.

- Periodic conditions: helpful when the physical geometry of interest and the flow patterns possess a periodically repeating nature. When a pressure drop or a flowrate are specified across translational periodic boundaries, this condition enables to model fully developed flows.

Although many options are available, the preferred entrance condition for analyzing the flow development in a rotating duct is the *velocity inlet* since it allows to specify a given velocity and/or turbulent profile as inlet condition. Hence, the conditions present in the experimental setup can be reproduced in the computational domain. This b.c. is also very interesting for demanding problems since the domain can be separated in many smaller sub-domains and the flow solution at the exit of a section can be set as inlet condition for the following downstream section.
The choice of an exit condition is more delicate since it often assumes a certain flow state. For example, the *pressure outlet* condition presumes that the value of the static pressure is uniform on the boundary. This b.c. is certainly inappropriate for modeling the flow in a rotating duct, since it is well known that rotation, through the action of the Coriolis force, generates a pressure gradient in the direction normal to the flow. Consequently, the pressure along the outlet boundary is not uniform. A more suitable exit condition is the *outflow* because no restrictions are enforced on the pressure distribution at the boundary. However, the *outflow* condition is formally respected only in fully developed flows. Since in the present study, the flow at the exit boundary is rarely close to full development, it is necessary to verify the effect of such condition on the solution. For this purpose, the flow development in a rotating channel is chosen as the test case. Two rectangular domains of width $2h$, but having different lengths are considered ($60h$ and $100h$ respectively). The same boundary conditions are applied to both domains (i.e., a uniform velocity profile with no turbulence at the entrance, an *outflow* condition at the exit and solid walls on the sides of the channel). The mesh discretization in the transverse direction is identical for both cases. In the streamwise direction, the channel having a length of $100h$ has the same discretization as the shorter channel up to a distance of $60h$ from the inlet. The remaining length of $40h$ has a uniform mesh and "grid continuity" is respected.
In the following analysis, the flow development in each domain is compared at two positions along the channel. The first station is at a distance $x/h = 50$. The second position coincides with the exit boundary of the short domain ($x/h = 60$). The long domain will serve as the reference case since the *outflow* b.c. is very far from the measurement stations and it is thus reasonable to assume that it has no effect on the flow solution at the two given stations.

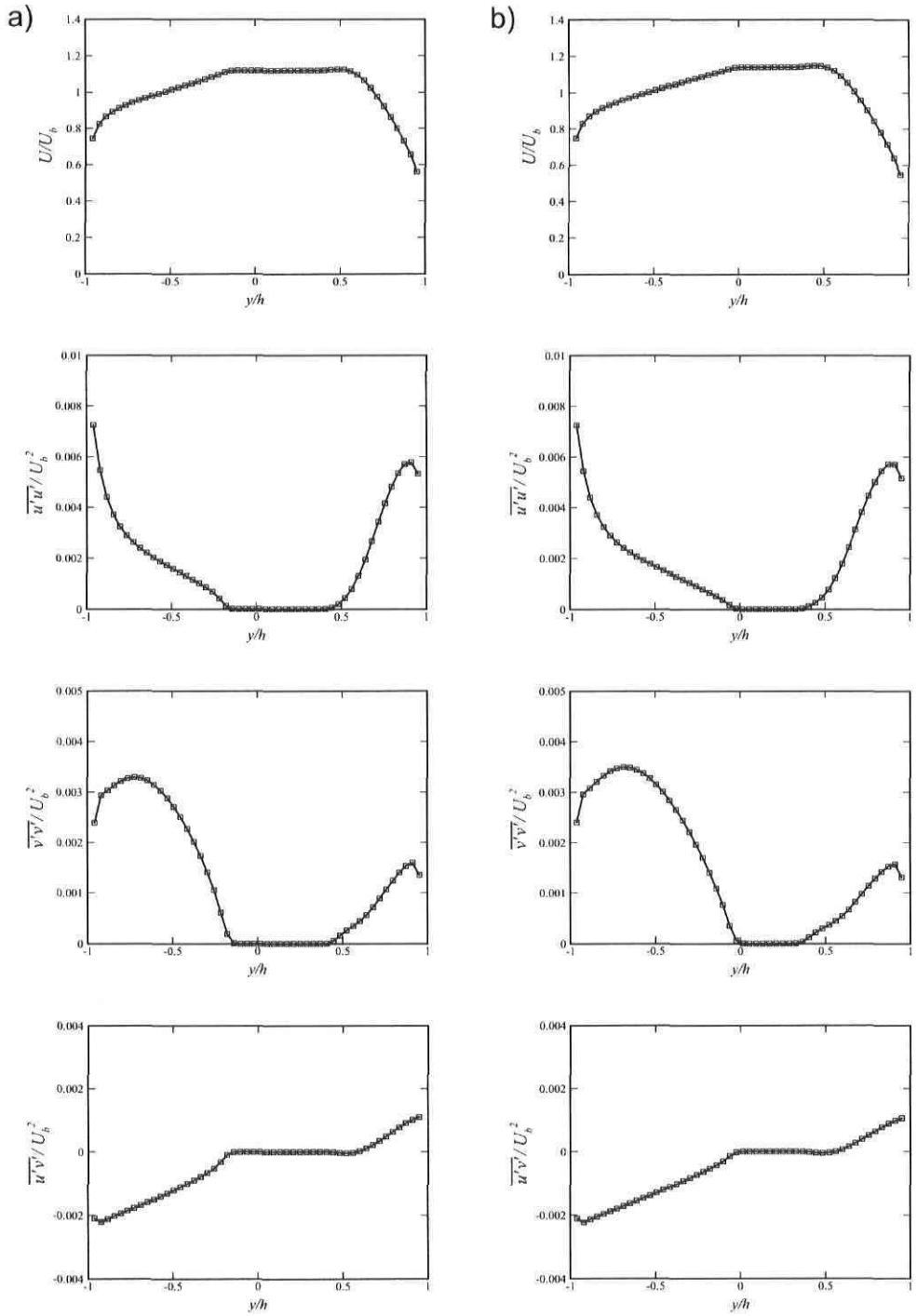

Figure 4.4: Normalized mean velocity profiles and Reynolds stress components at $Re = 40000$ and $Ro = 0.22$. □, Domain of length $60h$; ——, domain of length $100h$. (a): Measurement station at $x/h = 50$ ($10h$ from exit boundary of shorter domain); (b): measurement station at $x/h = 60$ (at exit boundary of shorter domain).

The plots of FIG. 4.4 show that in a rotating 2D channel, the *outflow* condition does not affect noticeably the flow development and, even very close to the exit boundary, no deviation is detected. Moreover, the present results confirm the independence of the flow solution with respect to the position of the rotation axis along the channel. In fact, when using an *outflow* condition with the *Fluent* solver, **the axis of rotation must be placed at the center of the exit boundary** (not mentioned in the *Fluent* documentation). This implies that the rotation axis is not located at the same position for the two domains.

Even though the soundness of the outlet condition has been proven for a 2D calculation, it is necessary to validate the b.c. for a three-dimensional case also. The chosen configuration is identical to the 2D case, except for the fact that the two ducts have now a finite aspect ratio ($AR = 11$). The mesh distribution in the streamwise and transverse directions remains unchanged with respect to the two-dimensional case and

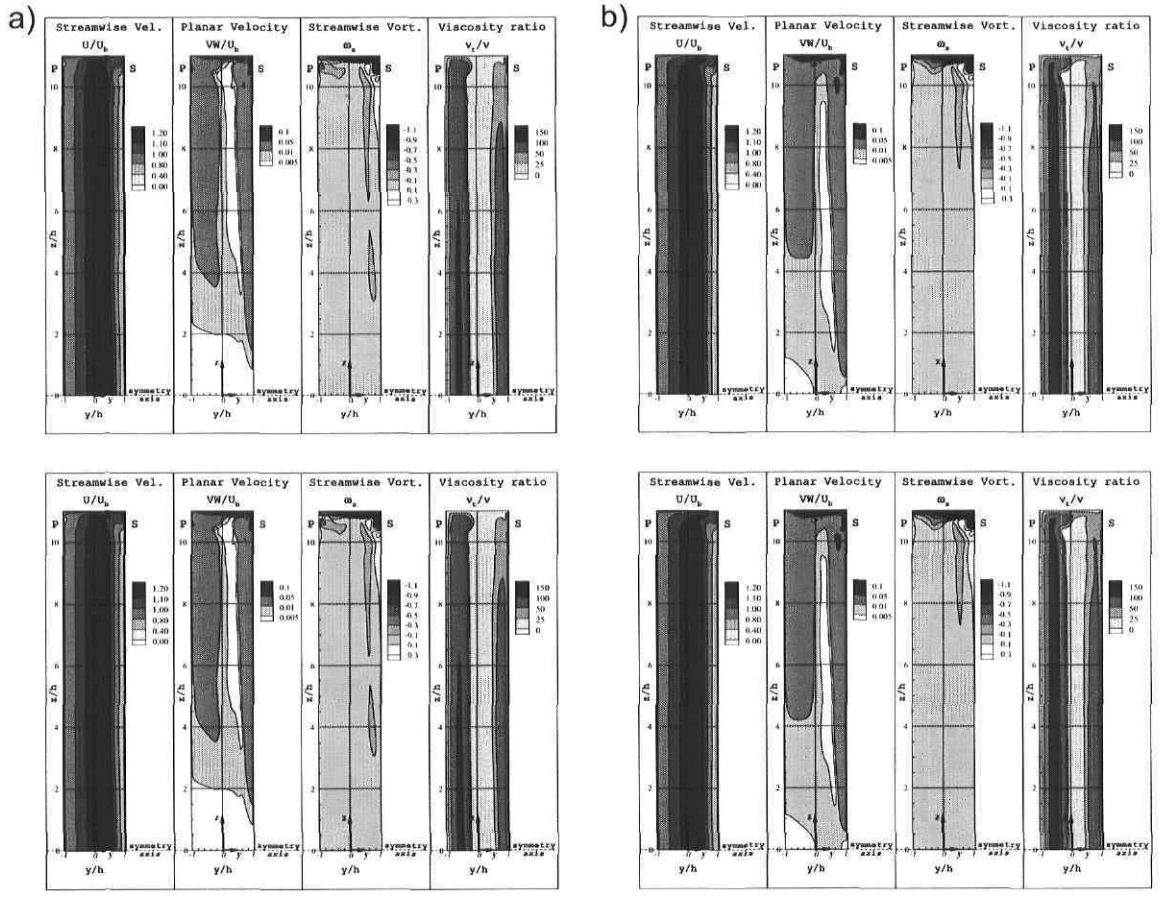

Figure 4.5: Plane contours in a rotating duct at $Re = 40000$ and $Ro = 0.22$. Flow direction toward the observer. (a): Measurement station at $x/h = 50$ ($10h$ from exit boundary of shorter domain); (b): measurement station at $x/h = 60$ (at exit boundary of shorter domain). Top figures correspond to the short domain while bottom ones correspond to the long domain.

the spanwise discretization is identical for the two domains. The contours of FIG. 4.5 show the solutions in a plane normal to the flow direction. At least qualitatively, the *outflow* boundary condition has a negligible impact on the flow development. In fact, at both measurement stations of the short duct, the computed field quantities match very well with those obtained from the longer domain. In order to measure more precisely the upwind effect of the outlet b.c., the RMS norm of the difference is computed for each quantity of interest:

$$\| \triangle_{L=100h} \|_{RMS} = \sqrt{\frac{1}{N}\sum_{i=1}^{N}\left(\frac{x_{i,\,L=60h} - x_{i,\,L=100h}}{x_{i,\,L=100h}}\right)^2}$$

where N is the number of cell-centered points present in the yz plane. The RMS values are listed in TABLE 4.3. The effect of the *outflow* condition is particularly important for

RMS norm	$x/h = 50$	$x/h = 60$
Streamwise velocity (U/U_b)	1.5×10^{-5}	7.9×10^{-4}
Planar velocity (VW/U_b)	1.0×10^{-3}	3.7×10^{-2}
Streamwise vorticity (ω_x)	1.6×10^{-4}	2.0×10^{-2}
Viscosity ratio (ν_t/ν)	1.6×10^{-4}	2.2×10^{-2}

Table 4.3: $\|\triangle_{L=100h}\|_{RMS}$ values in a yz plane of a rotating duct at two measurement stations - $Re = 40000$ and $Ro = 0.22$.

the planar velocity, the streamwise vorticity and the turbulent viscosity ratio since those quantities are evolving much more than the streamwise velocity between $x/h = 50$ and $x/h = 60$. Consequently, they are farther from the fully developed condition assumed at the *outflow* boundary. The RMS values listed in TABLE 4.3 indicate that a distance of $10h$ from the outlet is sufficient to guarantee that the upstream solution is essentially not affected by the *outflow* boundary. However, the distance of $10h$ should not be taken as an absolute criterion since this value can vary depending on the state of flow development. For example, if the domain had been shorter (e.g., $L = 30h$), the flow at the exit b.c. would have been still farther from being fully developed, and the $10h$ buffer zone would probably have been insufficient.

In the present study, the flow development in rotating ducts is performed with domains having lengths of $60h$ or more. Hence, the analysis will be confined to the region upstream of the $10h$ buffer zone.

The last boundary condition to be discussed is the *symmetry* condition. This b.c. is very useful and often employed since it allows to cut by half the number of cells in the computational domain. In the present study, only the upper-half portion of the duct is modeled and a symmetry plane is placed on the lower-end boundary (as shown in FIG. 4.5). Consequently, it is important to check that the *symmetry* condition is

adequate and that it does not induce any unwanted behaviour of the flow. The analysis is performed by computing the fully developed solution in a rotating duct of $AR = 11$. Once again, two computational domains are necessary. One domain models only the upper-half section of the duct and has a symmetry plane in the center (at $z/h = 0$). The second one represents the whole duct and no-slip wall conditions are set on both the upper and lower ends of the duct. For both calculations, the fully developed state is obtained by setting periodic conditions on the inlet and outlet planes of the duct. The length of both domains is $L = 0.1h$ and they are centered at $x/h = 0$. The mesh

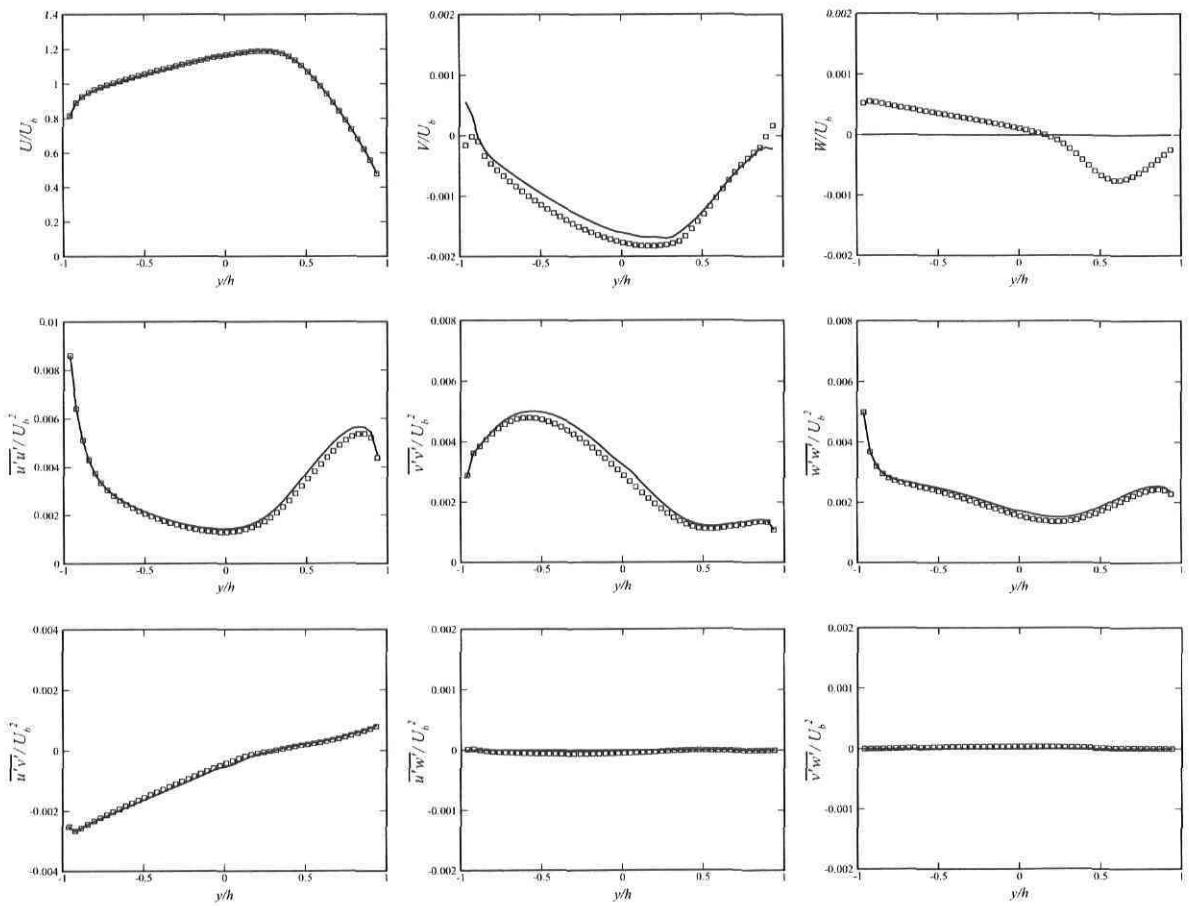

Figure 4.6: Fully developed solution in a rotating duct at $Re = 40000$ and $Ro = 0.22$. Normalized mean velocity profiles and Reynolds stress components along a line placed at $x/h = 0$ and $z/h = 0$. □, Domain with *symmetry* condition; —, whole domain.

discretization is identical for the two domains in all three directions (i.e., the second domain has exactly twice the number of cells of the first one). The graphs of FIG. 4.6 compare the solutions along an horizontal line placed in the center plane of the duct. The computation in a whole duct (i.e., continuous line plots) shows that a symmetry condition does indeed exist at the $z/h = 0$ plane, since the mean spanwise velocity (W), $\overline{u'w'}$ and $\overline{v'w'}$ are null at this location — all odd terms (with respect to z) are

null at $z/h = 0$. By comparing the solutions of the two domains, it seems that the *symmetry* condition is satisfied for all quantities except for the spanwise velocity (W). In fact, the impermeability condition is not strictly respected at the symmetry plane (error $O(10^{-3})$). Unfortunately, no clear explanation has been found for the observed phenomenon. Because of this anomaly, a comparison between the two simulation is

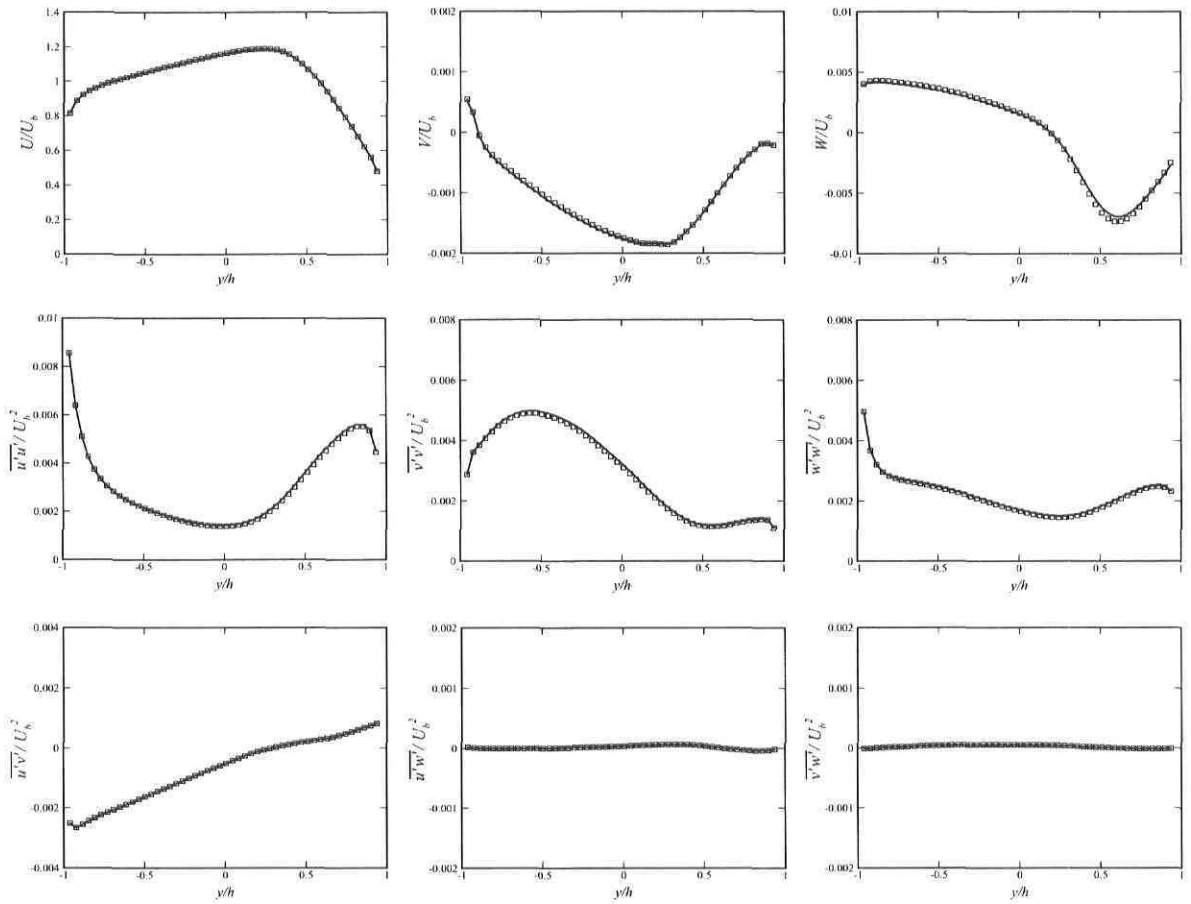

Figure 4.7: Fully developed solution in a rotating duct at $Re = 40000$ and $Ro = 0.22$. Normalized mean velocity profiles and Reynolds stress components along a line placed at $x/h = 0$ and $z/h = 2$. □, Domain with *symmetry* condition; —, whole domain.

performed at a new position across the duct ($z/h = 2$) somewhat above the previous mid-section. The results are illustrated in FIG. 4.7. It is reassuring to find that at this position, the two solutions match very well and no anomalies are present. In conclusion, the option of simulating only the upper-end portion of the duct, and of using a *symmetry* condition yields satisfactory results everywhere in the flow field except on the symmetry plane itself. Therefore, this approach will be employed for all subsequent calculations.

Chapter 5

Fully developed flow in rotating channels and rectangular ducts

Numerous simulations of rotating channel and duct flows are performed in order to investigate the effects of the Reynolds number and the Rotation number on the main flow characteristics. For the 3D case, the intensity and dynamic consequences of end-wall structures are also discussed.
The simulations of this chapter will also help explain the discrepancies observed between the experimental measurements and the DNS results, a problematic which has in part motivated the present investigation as mentioned in the introduction of chapter one.

5.1 Fully developed flow in a rotating channel

In this section, the fully developed ($\partial/\partial x = 0$) two-dimensional ($\partial/\partial z = 0$) Poiseuille flow in a rotating channel is considered. The objective is to show how the Rotation number affects the mean velocity and Reynolds stress profiles. Moreover, the effect of the Reynolds and Rotation numbers on the extent of the constant slope region in the mean velocity profile is addressed. In the following calculations, the Reynolds number is varied between 10000 and 40000 whereas the Rotation number ranges from 0 to 0.22. The computational domain has a length of $10h$ and a width of $2h$. The mesh has 80 points in the streamwise direction and 51 in the transverse direction. The size of the wall adjacent cells is adjusted for each regime in order to always maintain a $y^+_{\text{fc}} \approx 40$. Periodic conditions are set on the inlet and outlet boundaries (see Appendix A for more details on this approach).

As shown in FIG. 5.1, the shape of the streamwise velocity profile near the walls is altered, even at a low Rotation number ($Ro = 0.11$). As the system angular velocity

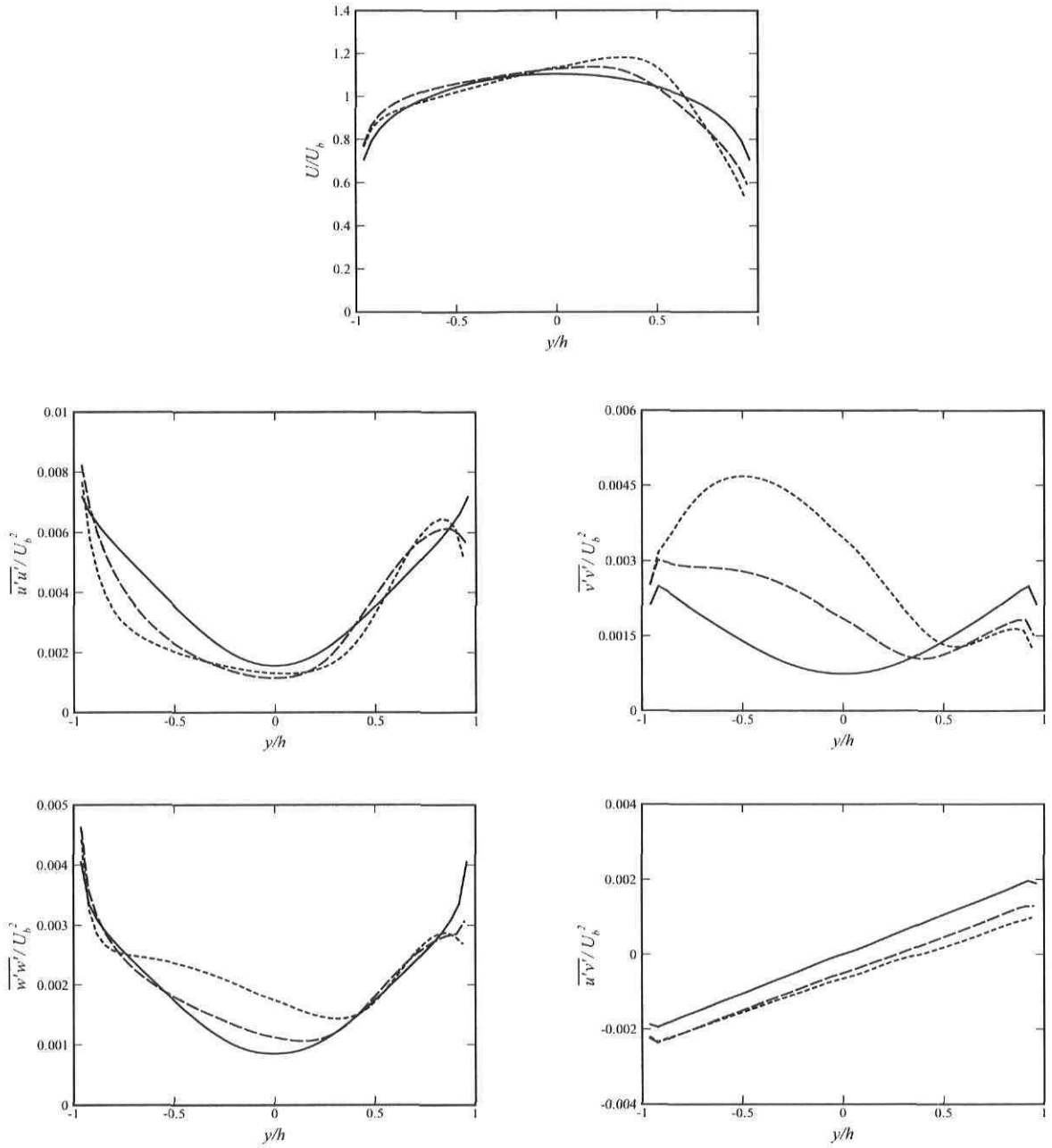

Figure 5.1: Fully developed solution in a rotating channel at $Re = 40000$. Normalized mean streamwise velocity and Reynolds stress components. ——, $Ro = 0$; – –, $Ro = 0.11$; - - -, $Ro = 0.22$.

increases, the slope of the velocity profile near the suction side decreases and this results in a lower value for the shear stress at the boundary (TABLE 5.1). Near the pressure side wall, the behaviour appears to be non-monotonous since the value of τ_w increases when $Ro = 0.11$, but it begins to decrease at $Ro = 0.22$. In the central portion of

Ro	Re_τ^s	Re_τ^p	Re_τ
0	1843.9	1843.9	1843.9
0.11	1538.6	2003.6	1771.1
0.22	1354.1	1986.8	1670.4

Table 5.1: Rotation effect on wall shear stress at $Re = 40000$.

the channel, the region where the slope of the mean velocity profile is constant, and approximately twice the value of the system angular velocity, becomes wider as the Rotation number increases.

The effect of rotation is even greater on the Reynolds stresses where the asymmetry between the suction and pressure sides is more pronounced. The shear stress $\overline{u'v'}$ becomes lower with increasing Ro and its slope in the central region of the channel slightly decreases. The transverse fluctuations ($\overline{v'v'}$) are amplified on the unstable side and are reduced on the stable side with increasing rotation. It is interesting to note that the maximum fluctuation of $\overline{v'v'}$ is relatively distant from the pressure side wall. The behaviour of the streamwise fluctuations ($\overline{u'u'}$) near the suction side is distinct since at low rotation rates ($Ro = 0.11$) the peak value decreases but it increases at higher rotation ($Ro = 0.22$). A possible explanation is that the total production $P_{11} + R_{11} = -2\overline{u'v'}\,dU/dy + 4\Omega\,\overline{u'v'}$ is dominated by the mean shear production (P_{11}) and that the contribution of R_{11} is small. It is also worth mentioning that, although P_{33} and R_{33} are both null, the $\overline{w'w'}$ profile is greatly affected by system rotation because of pressure-strain redistribution.

The effect of the Reynolds number on the streamwise velocity profile is shown in FIG. 5.2. Since the Rotation number is kept constant at $Ro = 0.22$, the velocity gradient in the central portion of the channel remains the same in all three cases ($dU/dy \approx 0.22$). However, as the Reynolds number increases, the velocity profile is stretched toward the walls and the region of constant slope becomes wider.

Although the values of TABLE 5.2 should be taken with caution, since shear stresses are

Re	Re_τ^s	Re_τ^p	Re_τ	Re_τ/Re	$(Re_\tau^p - Re_\tau^s)/Re_\tau$
10000	414.7	575.1	494.9	0.0495	0.324
20000	734.2	1061.0	897.6	0.0449	0.364
40000	1354.1	1986.8	1670.4	0.0418	0.379

Table 5.2: Reynolds effect on wall shear stress at $Ro = 0.22$.

computed via a wall function, they indicate that the relative difference ($[Re_\tau^p - Re_\tau^s]/Re_\tau$) between the wall shear stress on the pressure and suction side of the channel decreases as the Reynolds number becomes smaller.

The effect of the Reynolds number is particularly visible on the diagonal terms of the Reynolds stress tensor. The amplitude of all three stresses increases with decreasing

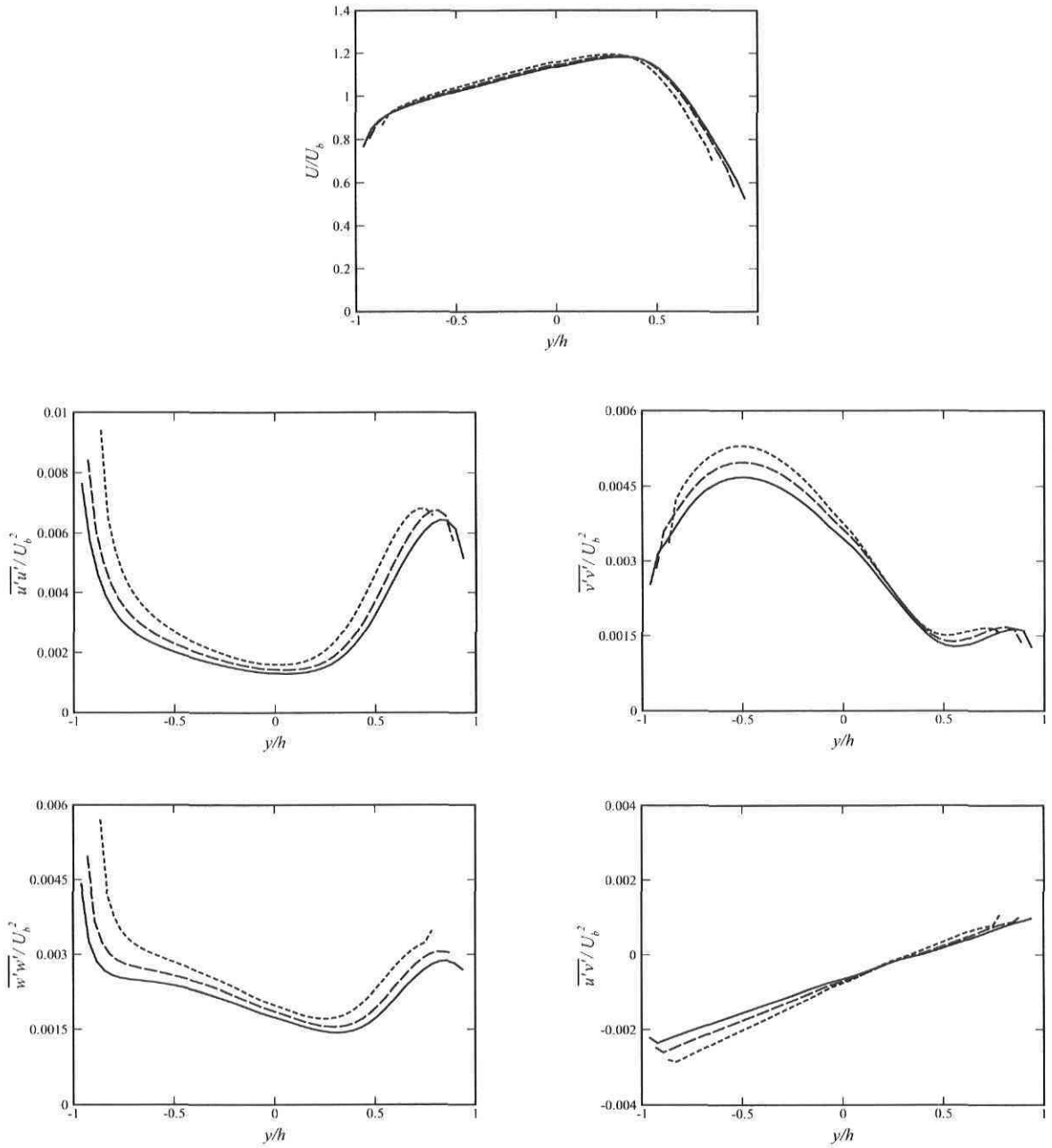

Figure 5.2: Fully developed solution in a rotating channel at $Ro = 0.22$. Normalized mean streamwise velocity and Reynolds stress components. ——, $Re = 40000$; – –, $Re = 20000$; - - -, $Re = 10000$.

Reynolds number, especially near the pressure side. However, the overall shape of the Reynolds stress profiles is maintained since the Reynolds number has an even effect across the entire domain. Finally, the Reynolds number has a impact on the distribu-

tion of $\overline{u'v'}$ since the slope of the stress term is significantly enhanced at lower Re.
In conclusion, the plots of FIG. 5.1 suggest that the effect of rotation is localized and distinctive between the pressure and suction side of the channel. In the range of flow regimes studied here, the stress terms are damped by rotation near the suction side of the channel and amplified on the opposite side, at the exception of the streamwise fluctuation. In contrast, the effect of the Reynolds number (FIG. 5.2) appears somewhat more uniform throughout the entire duct and all the stress terms are damped with increasing Reynolds number.

5.2 Fully developed flow in a rotating duct

In this section, 3D computations of a fully developed flow in a rotating duct of finite aspect ratio ($AR = 11$) are performed at different Reynolds and Rotation numbers. Particular attention is given to the impact of the end-wall generated cross-stream current on the two-dimensionality of the flow. Moreover, the previous 2D calculations of a rotating channel will serve as reference cases in order to better account for the end-wall effects in a rotating duct.
The three-dimensional simulations were run by my colleague S. Julien (see Julien *et al.*, 2006) and I take the opportunity to underline once more his contribution to the present work.
Normally, the fully developed flow in a rotating duct would be computed with a two-dimensional domain (i.e., a yz plane with the rotation axis aligned in the z-direction) since fully developed conditions imply that $\partial/\partial x = 0$. Unfortunately, as mentioned previously, *Fluent* does not offer the possibility to specify a flow rate in a direction normal to the 2D plane (x-direction). Consequently, a three-dimensional domain must be used.
The preferred approach to reproduce fully developed flow conditions in this work is to have a very short domain ($L = 0.1h$) and to apply periodic conditions in the streamwise direction (FIG. 5.3a). The width of the computational domain is kept at $2h$ and the height is $11h$ in order to have the desired aspect ratio of 11. The mesh has 11475 elements: 5 cells in the streamwise direction, 51 in the transverse direction and 45 in the spanwise direction. As for the 2D case, the size of the wall adjacent cells is adjusted for each regime in order to maintain a $y^+_{\text{fc}} \approx 40$.

5.2.1 Mesh independence

Before studying the end-wall effects at various flow regimes, a series of tests were performed in order to insure mesh independence. The case chosen for this purpose is the flow in a rotating duct at $Re = 40000$ and $Ro = 0.22$. The choice is justified by the fact that the Ekman vorticity, and associated secondary flow phenomena, will be more intense at this rotation rate. Therefore, if no variations are observed at this regime after a mesh refinement, it is reasonable to assume that the initial discretization will also be adequate at lower rotation rates. The same argument stands for the Reynolds number.
The refined domain has the same dimensions but twice the discretization in each direction with respect to the one of FIG. 5.3. In order to verify mesh independence, the flow

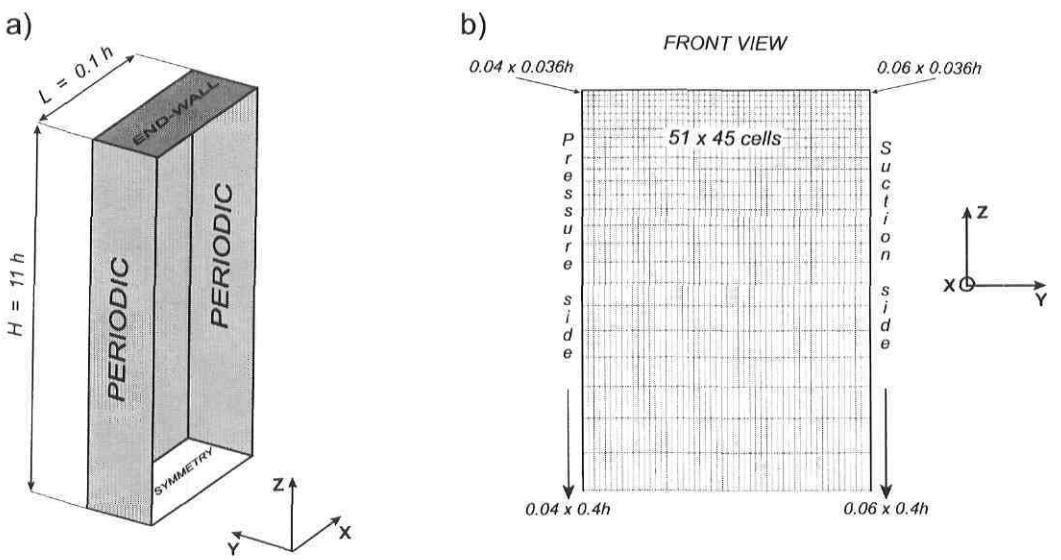

Figure 5.3: (a): Computational domain of 3D fully developed duct. (b): Mesh distribution in the yz plane; size of wall-adjacent cells corresponds to case at $Re = 40000$ and $Ro = 0.22$.

solutions of the standard and refined meshes are compared (FIG. 5.4 and 5.5) and the RMS norm of the difference is computed. The results are shown in TABLE 5.3 and 5.4, where the fine mesh is used as the reference case. At least qualitatively, the contours of FIG. 5.4a and 5.4b are very similar and no major differences are observed. However, a small divergence is observed for the contours of turbulent viscosity ratio and streamwise vorticity. Such a behaviour is not alarming since the differences are mainly localized near the upper-wall of the duct, whereas the region of interest is situated close to the symmetry plane. At this location (FIG. 5.5), the profiles of streamwise velocity and the non-null Reynolds stress terms show good agreement between the standard and refined cases. Once again, the streamwise velocity is the quantity showing the best match.

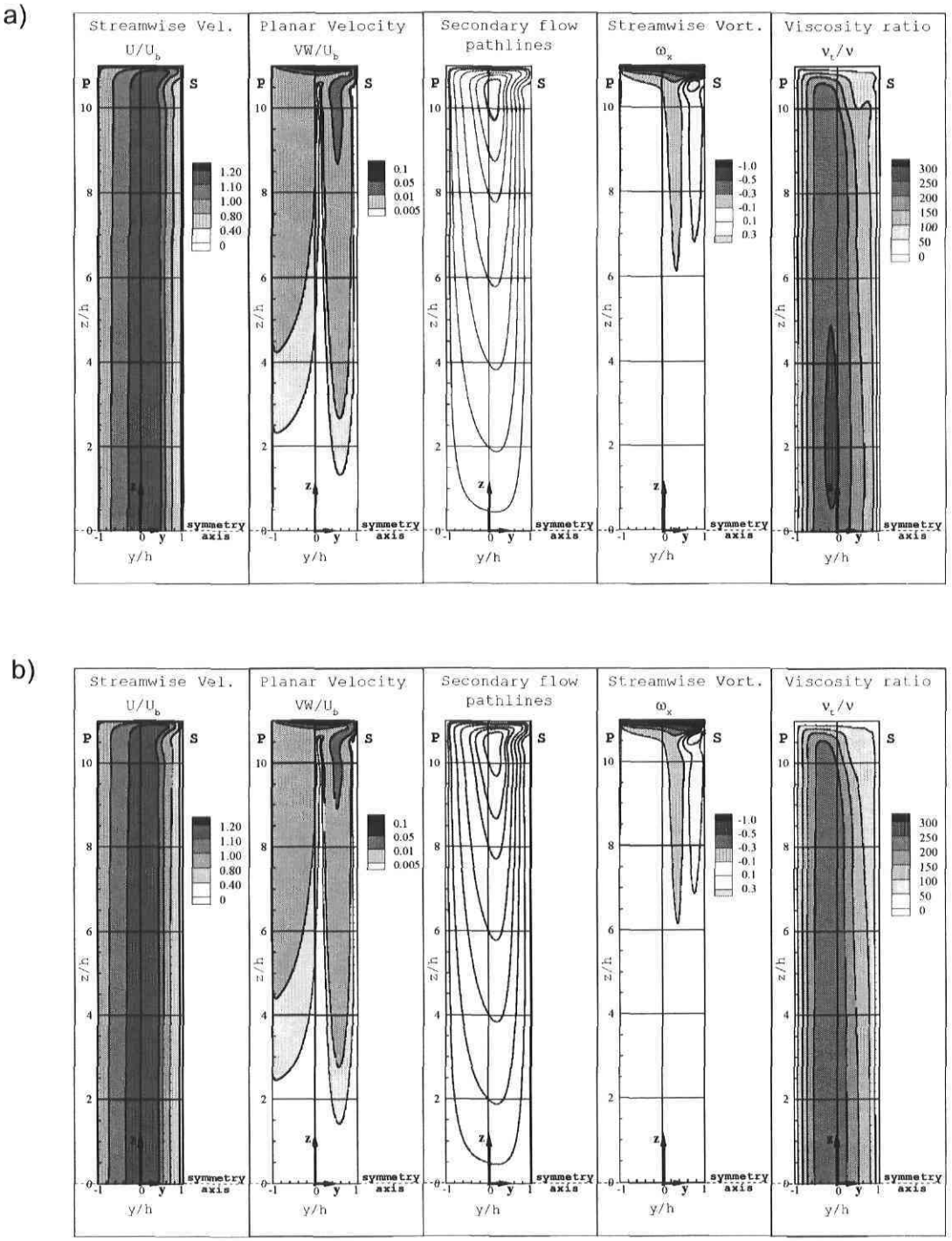

Figure 5.4: Plane contours of a rotating duct at $Re = 40000$ and $Ro = 0.22$. (a): Standard mesh; (b): fine mesh. Flow direction toward the observer.

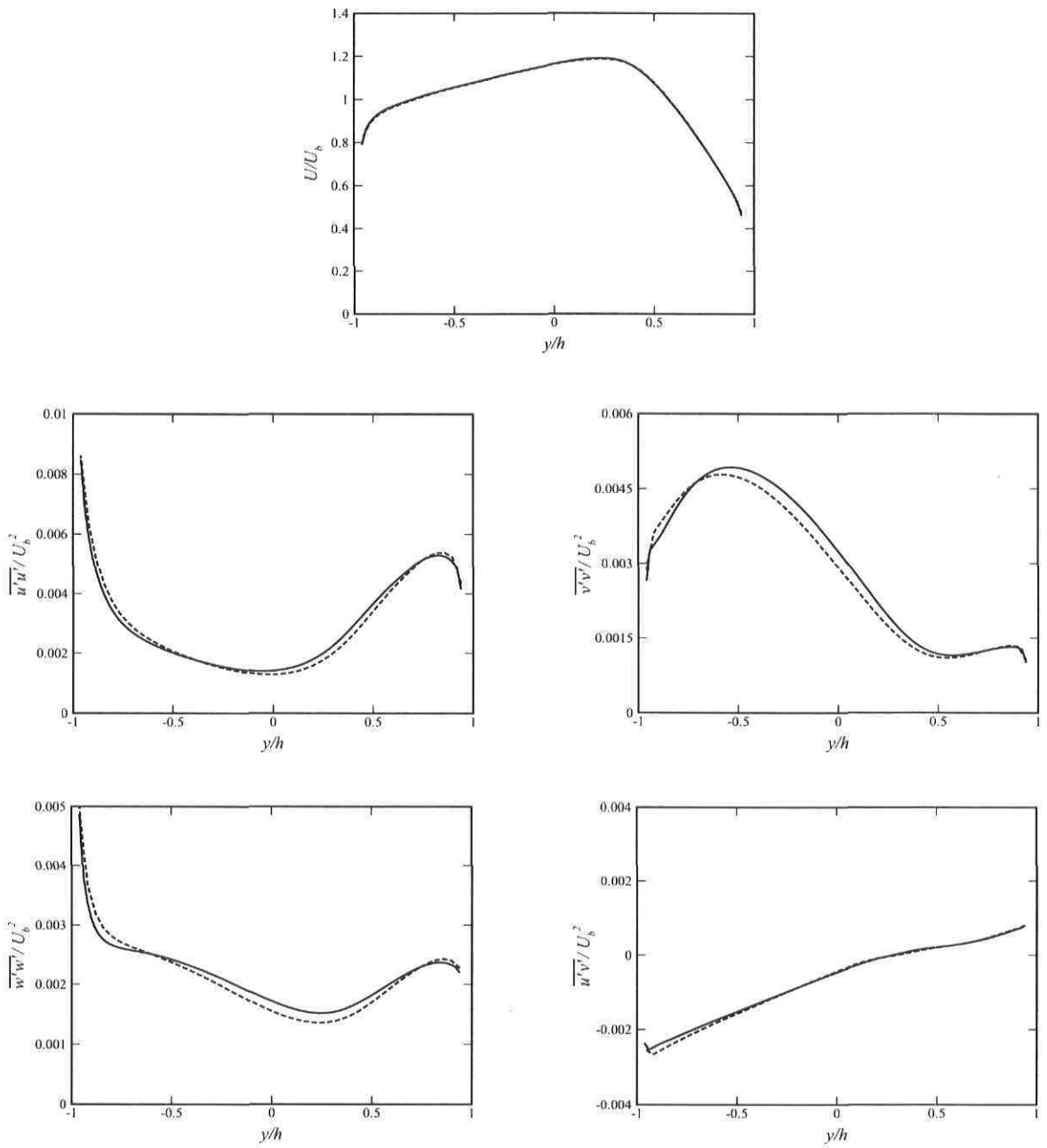

Figure 5.5: Profiles at symmetry axis of a rotating duct at $Re = 40000$ and $Ro = 0.22$. ——, Fine mesh; – –, standard mesh.

A more accurate way of evaluating the degree of mesh independence is to calculate the RMS norm of the difference. It should be noted that our approach of computing this norm excludes all comparison points where the values are judged too small. If the solution in the entire yz plane is considered, the RMS values vary from 0.6% to 29% for U and ω_x respectively. The relatively high RMS value for the streamwise vorticity is due to the fact that, with the coarse mesh, the Ekman layer (associated with negative vorticity) extends over the entire width of the duct whereas a zone of positive vorticity exists near the suction side of the refined domain.

	RMS norm
Streamwise velocity (U/U_b)	0.0058
Planar velocity (VW/U_b)	0.105
Streamwise vorticity (ω_x)	0.291
Viscosity ratio (ν_t/ν)	0.115

Table 5.3: $\|\triangle\|_{RMS}$ values in the central yz plane of a rotating duct at $Re = 40000$ and $Ro = 0.22$.

As it was mentioned earlier, the slight divergences near the upper wall of the duct do not affect the solution at the symmetry plane. In fact, at this position the RMS norm ranges from 0.3% to 7%. Different variables are selected for evaluating the RMS norm at the symmetry axis since the streamwise vorticity and the planar velocity are either null or very small at this boundary.

	RMS norm
Streamwise velocity (U/U_b)	0.00290
Stress term $(\overline{u'u'}/U_b^2)$	0.0696
Stress term $(\overline{v'v'}/U_b^2)$	0.0665
Stress term $(\overline{w'w'}/U_b^2)$	0.0685
Stress term $(\overline{u'v'}/U_b^2)$	0.0483

Table 5.4: $\|\triangle\|_{RMS}$ values at symmetry axis of a rotating duct at $Re = 40000$ and $Ro = 0.22$.

In conclusion, since the primary variable of interest in the present study is the streamwise velocity, and this quantity is most certainly mesh independent, the initial mesh discretization is judged adequate and future calculations will be carried using the domain and grid of FIG. 5.3.

5.2.2 End-wall effects on two-dimensionality

As explained in chapter 2, the presence of an horizontal wall boundary causes an imbalance between the Coriolis and pressure forces which results in the generation of a secondary flow. In this section, the impact of the end-wall generated secondary flow on the velocity and turbulent profiles at the central plane of the duct is discussed. The study focuses primarily on the basic configuration ($AR = 11$, $Re = 40000$ and $Ro = 0.22$), but rotation and Reynolds number effects are also presented.

FIG. 5.6 shows the intensity of the secondary flow and associated streamwise vorticity in a plane normal to the main flow direction. The maximum of planar velocity ($VW \approx 10\% U_b$) is observed in a thin zone near the upper wall, where the Ekman pumping is active. As indicated by the streamlines, the particles of fluid descend near

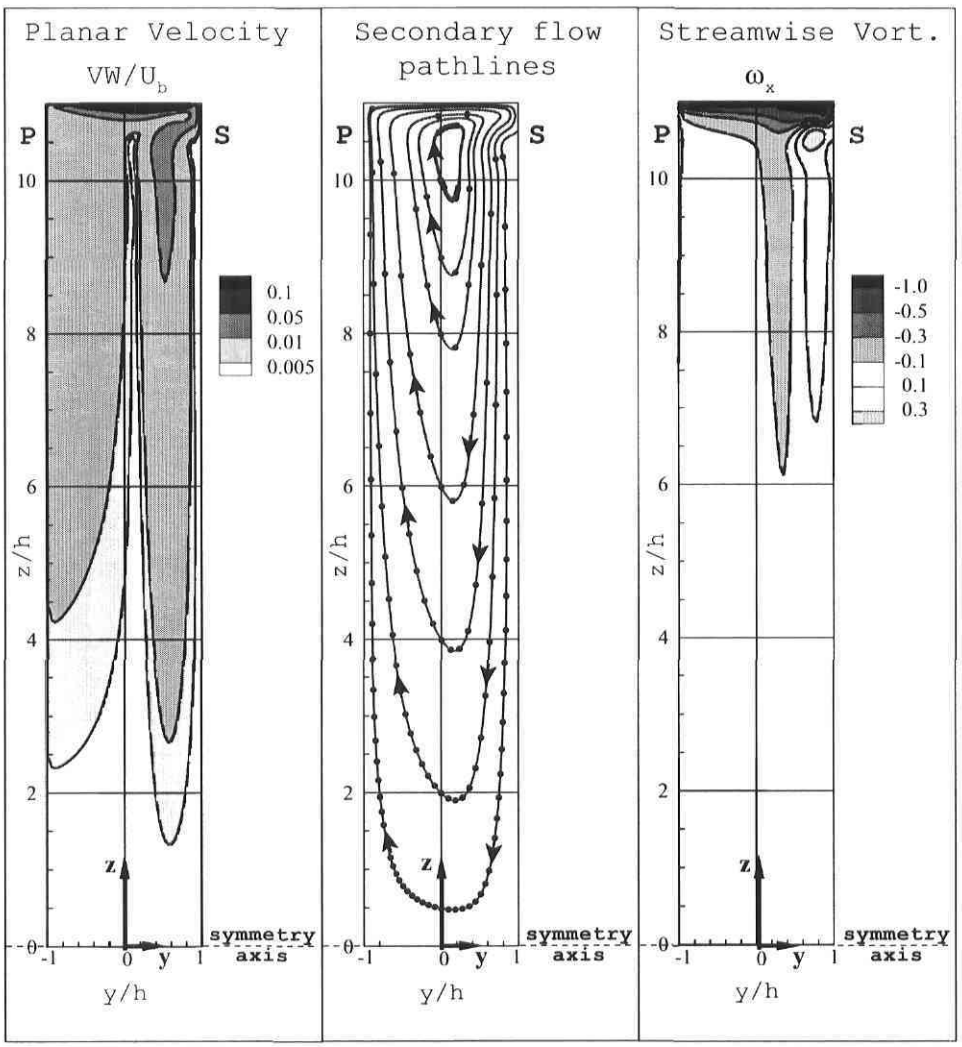

Figure 5.6: End-wall effects in a rotating duct at $Re = 40000$ and $Ro = 0.22$. Flow direction toward the observer.

the suction wall until they reach the symmetry plane, and then they ascend along the pressure side toward the upper wall in a circular motion.
Even though the secondary flow velocity at the symmetry plane is very small compared to the streamwise component ($V \approx 0.1\% U_b$), it has a non-negligible contribution to the x-momentum balance. As shown in FIG. 5.7, the streamwise velocity profiles of the 2D and 3D rotating ducts clearly differ. To better understand the effect of the secondary

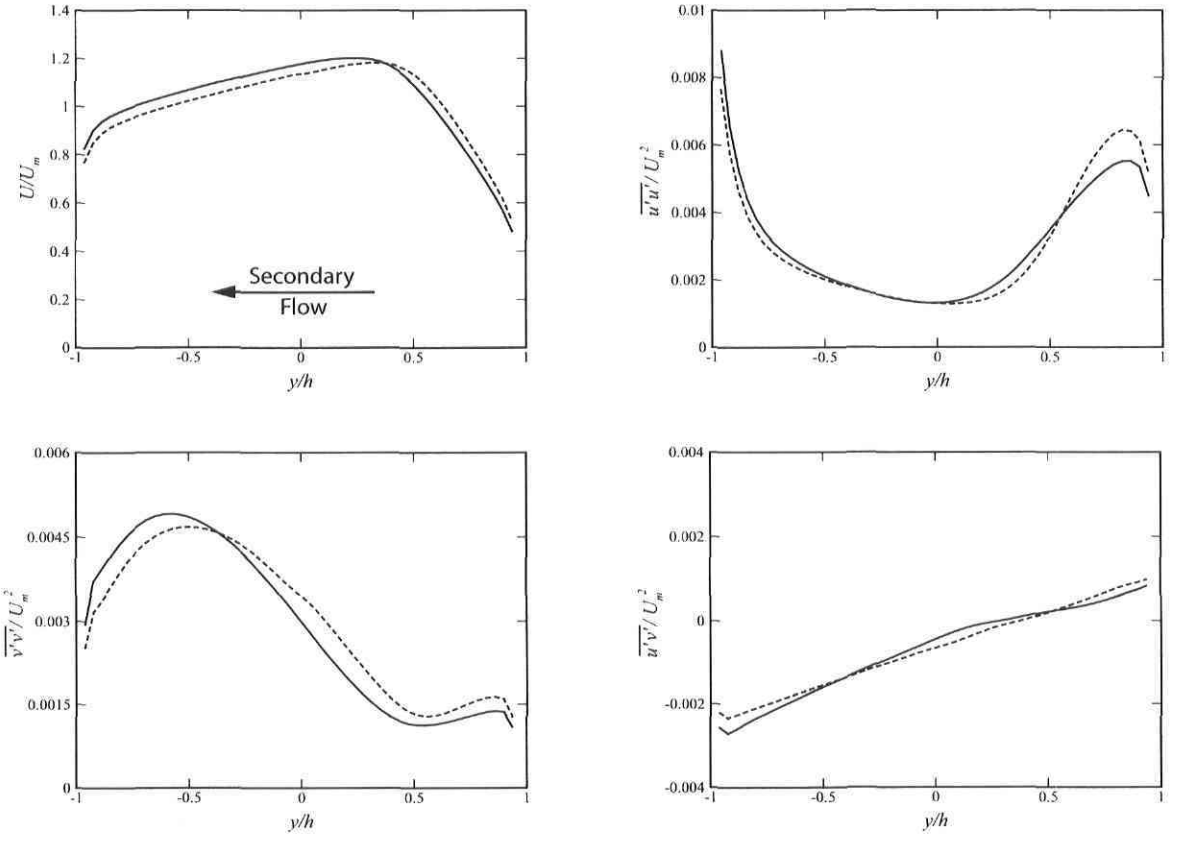

Figure 5.7: Velocity and Reynolds stress profiles of a rotating duct/channel at $Re = 40000$ and $Ro = 0.22$. —, 3D case (at symmetry plane); – –, 2D case. U_m is the mean velocity at the symmetry plane.

flow on U, it is necessary to analyze the streamwise mean momentum equation at the symmetry plane of a fully developed duct:

$$0 = -\langle V \frac{\partial U}{\partial y} \rangle - \frac{\partial P}{\partial x} + \frac{1}{Re} \left(\frac{\partial^2 U}{\partial y^2} + \langle \frac{\partial^2 U}{\partial z^2} \rangle \right) - \frac{\partial}{\partial y} \overline{u'v'} - \langle \frac{\partial}{\partial z} \overline{u'w'} \rangle + \langle Ro\, \Omega\, V \rangle \quad (5.1)$$

where the terms in $\langle\ \rangle$ are the additional terms with respect to the 2D case. The magnitude of the main terms for the 3D and 2D cases are plotted in FIG. 5.8. The pressure gradient is not plotted since it is constant across the domain and the viscous terms are omitted since they are negligible everywhere, except close to the walls. Hence, there is only one term left for the 2D channel case.

It should be mentioned that, for the 2D case, the peak of $\partial\overline{u'v'}/\partial y$ at $y/h = 0.4$ is unexpected and originates from a small wiggle in the $\overline{u'v'}$ profile.
From FIG. 5.8, it is clear that the levels of the turbulent transport term $\partial\overline{u'v'}/\partial y$ have varied between the 2D and 3D cases. However, the overall effect of $\overline{u'v'}$ on the streamwise velocity profile remains unchanged since in both cases it transports momentum from the center toward the walls of the duct. Consequently, this term is not responsi-

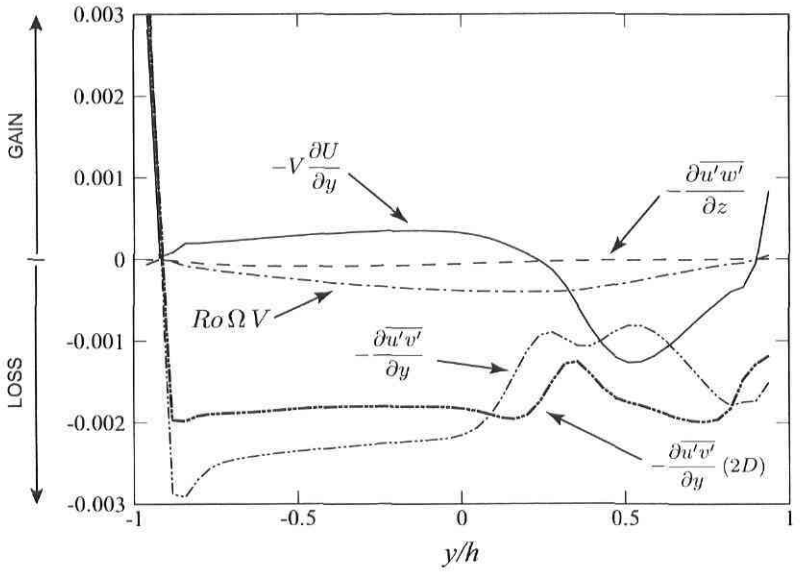

Figure 5.8: Turbulence and secondary flow contributions to the x-momentum equation at the symmetry plane of a rotating duct (thin lines) and rotating channel (thick line); $Re = 40000$ and $Ro = 0.22$.

ble for the change in the velocity profile. A similar argument is valid for $Ro\,\Omega\,V$ since this term subtracts streamwise momentum, but it does so across the entire domain. Therefore, the only element able to generate a discrepancy between the 2D and 3D velocity profiles is the advection term $V\partial U/\partial y$. FIG. 5.8 shows that this term transfers momentum from the suction side to the pressure side of the duct. The direct consequence is a lower velocity near the suction side and a higher velocity on the opposite side, compared to the 2D case. This is exactly the behaviour observed in FIG. 5.7.
In conclusion, even though the secondary flow at the symmetry plane of the duct is very small in intensity, and difficult to detect experimentally, it has a non-negligible impact on the streamwise velocity profile. Therefore, comparisons between experimental results (even for high aspect ratio ducts) and 2D numerical computations should be performed very cautiously.

The second end-wall effect to be discussed here is the extent of the two-dimensional zone $\partial U/\partial z \approx 0$ in a rotating duct of $AR = 11$ (this notion of two-dimensionality is only partial however since, of course, truly 2D flow would also require $\partial V/\partial z = \partial W/\partial z = 0$). While viscous effects in a non-rotating duct cause a spanwise velocity gradient through the entire height of the duct, in the presence of rotation the velocity gradient is confined to a thin region near the upper wall. Consequently, $U(y)$ is practically uniform in the z-direction over most of the central portion of the duct. This aspect is observed in the

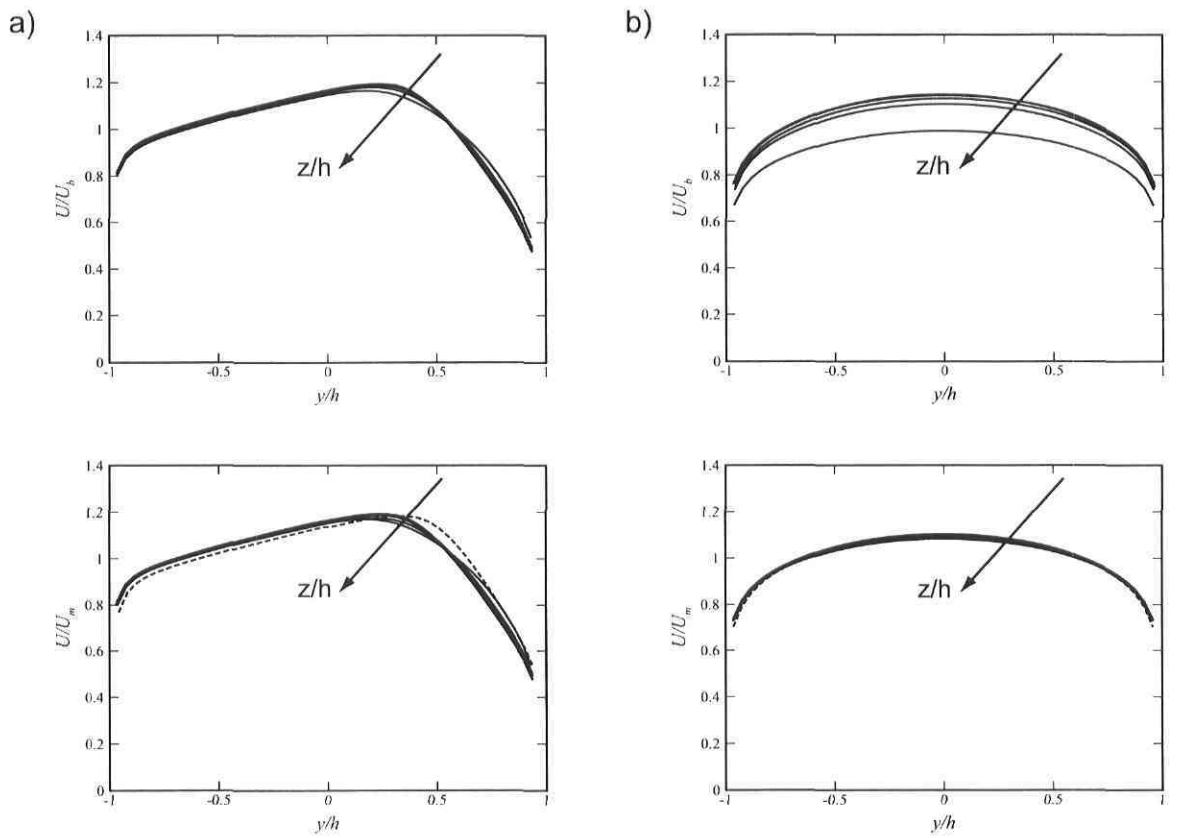

Figure 5.9: Velocity profiles at different spanwise locations of a duct at $Re = 40000$: $z/h = 0$, $z/h = 2$, $z/h = 4$, $z/h = 6$, $z/h = 8$, $z/h = 10$. (a): $Ro = 0.22$; (b): $Ro = 0$. ——, 3D case; – –, 2D case. The direction of the arrows indicates increasing z.

plots of FIG. 5.9 where the streamwise velocity profiles (normalized either with the bulk velocity of the duct $U_b = Q/A$ or the mean velocity at the plane $U_m(z) = \frac{1}{2h}\int_{-h}^{h} U dy$) are traced at different heights along the duct. For the rotating case, $U(y)/U_b$ remains constant on a greater portion of the domain compared to the non-rotating case. The RMS norm of the difference (TABLE 5.5) indicates that, even at a distance of h from the upper wall, the asymmetric velocity profile shows a small variation whereas the symmetric profile is greatly affected by the presence of an upper wall. Consequently, through the action of the Coriolis force (Taylor-Proudman type regime), rotation increases the extent of the zone $\partial U/\partial z \approx 0$ in the duct and limits the viscous effects to

a thin layer, namely the Ekman layer.

Position	RMS norm ($Ro = 0$)	RMS norm ($Ro = 0.22$)
$z/h = 0$	—	—
$z/h = 2$	0.00274	0.00227
$z/h = 4$	0.00537	0.00550
$z/h = 6$	0.0145	0.0111
$z/h = 8$	0.0438	0.0212
$z/h = 10$	0.131	0.0427

Table 5.5: $\|\triangle_{z/h=0}\|_{RMS}$ values of streamwise velocity at different spanwise locations (from symmetry plane at $z/h = 0$ toward the end wall of a rotating and non-rotating duct at $Re = 40000$.

However, as it was previously shown, the end-wall generated secondary flow causes a momentum transport at the symmetry plane of the duct which alters the streamwise velocity profile. This effect is visible on the lower plots of FIG. 5.9, where the velocity profiles, normalized with the mean velocity at the plane (U_m), are plotted. Clearly, the $U(y)$ profile in the central portion of the duct is much closer to the 2D profile when the system is non-rotating since the secondary flow is then much less intense and is confined to the upper corners of the duct (see FIG. 5.10). This trend is confirmed by the RMS norm of the difference of TABLE 5.6, where the 2D profile is compared with the U(y) profile (normalized with the mean velocity at the plane). In conclusion, the secondary

Position	RMS norm ($Ro = 0$)	RMS norm ($Ro = 0.22$)
$z/h = 0$	0.00864	0.0470
$z/h = 2$	0.00741	0.0441
$z/h = 4$	0.00750	0.0412
$z/h = 6$	0.00792	0.0365
$z/h = 8$	0.00769	0.0298
$z/h = 10$	0.0124	0.0249

Table 5.6: $\|\triangle_{2D}\|_{RMS}$ values of streamwise velocity at different locations of a rotating and non-rotating duct at $Re = 40000$.

flow in a rotating duct has a twofold effect: to create a region where $\partial U/\partial z \approx 0$ but also to alter the streamwise velocity profile in such a way that it differs noticeably from the 2D case of infinite aspect ratio. Consequently, the presence of a "two-dimensional zone" in the rotating duct does not guarantee that the solution corresponds to the theoretical 2D case.

5.2.3 Reynolds and Rotation number effects

In the previous section, very interesting observations about the effect of the secondary flow on the two-dimensionality of the solution have been made. However, the discussion was based on a single calculation performed at $Re = 40000$ and $Ro = 0.22$. In order to extend the validity of the concluding remarks, computations are now performed on a broader range of Reynolds and Rotation numbers. Particular attention is given to the intensity of the secondary flow and to its effect on the velocity profile at the symmetry plane of the duct.

At first, the Reynolds number is kept constant at 40000 and the Rotation number is varied between 0 and 0.22. If the graphs of FIG. 5.10 and 5.4a are compared, the first observation is that, as expected from eq. 2.10, the intensity of the Ekman vorticity diminishes as the Rotation number decreases, and it becomes null in the non-rotating case.

However, the magnitude of the secondary flow across the duct remains practically constant between the cases at $Ro = 0.22$ and 0.11. This phenomenon can be explained by looking at the conditions necessary to generate the cross-stream current. As it was mentioned in chapter 2, rotation causes a pressure gradient in the transverse direction ($\partial p/\partial y$). In the central portion of the duct the pressure force is balanced by the Coriolis force, but near the upper boundary this condition is not respected anymore and the intensity of the end-wall generated secondary flow will be proportional to the magnitude of the disequilibrium between the two forces. As stated by equation (2.7), for a higher Rotation number the pressure gradient increases. However, the streamwise velocity remains constant on a larger spanwise portion of the duct. In consequence, the disequilibrium between the pressure and Coriolis forces is more intense but it is confined to a smaller region as rotation increases. Since the two phenomena balance each others, the overall effect is that the intensity of the secondary flow is independent of the rotation rate (at least between $Ro = 0.11$ and $Ro = 0.22$).

For the non-rotating case, the solution is symmetric and no Ekman vorticity is present. The streamwise vorticity of FIG. 5.10b is associated with corner effects and its intensity is one order of magnitude smaller than the Ekman vorticity. As indicated by the contours of planar velocity, the secondary flow is very weak and confined to the upper region of the duct. Finally, the contours of streamwise velocity confirm that the extent of the two-dimensional zone ($\partial U/\partial z \approx 0$) increases as the Rotation number increases.

The effect of the secondary flow, at different rotation rates, on the streamwise velocity profile is illustrated in FIG. 5.11. At $Ro = 0.11$, the variation between the 2D and 3D velocity profiles is slightly reduced but it is still noticeable. As it was stated before, the quantity responsible for the differences between the 2D and 3D velocity profiles is the advection term ($V\partial U/\partial y$). Since the transverse velocity (V) at the symmetry plane is around $0.1\%U_b$ for both rotating cases, the small reduction in the momentum transport

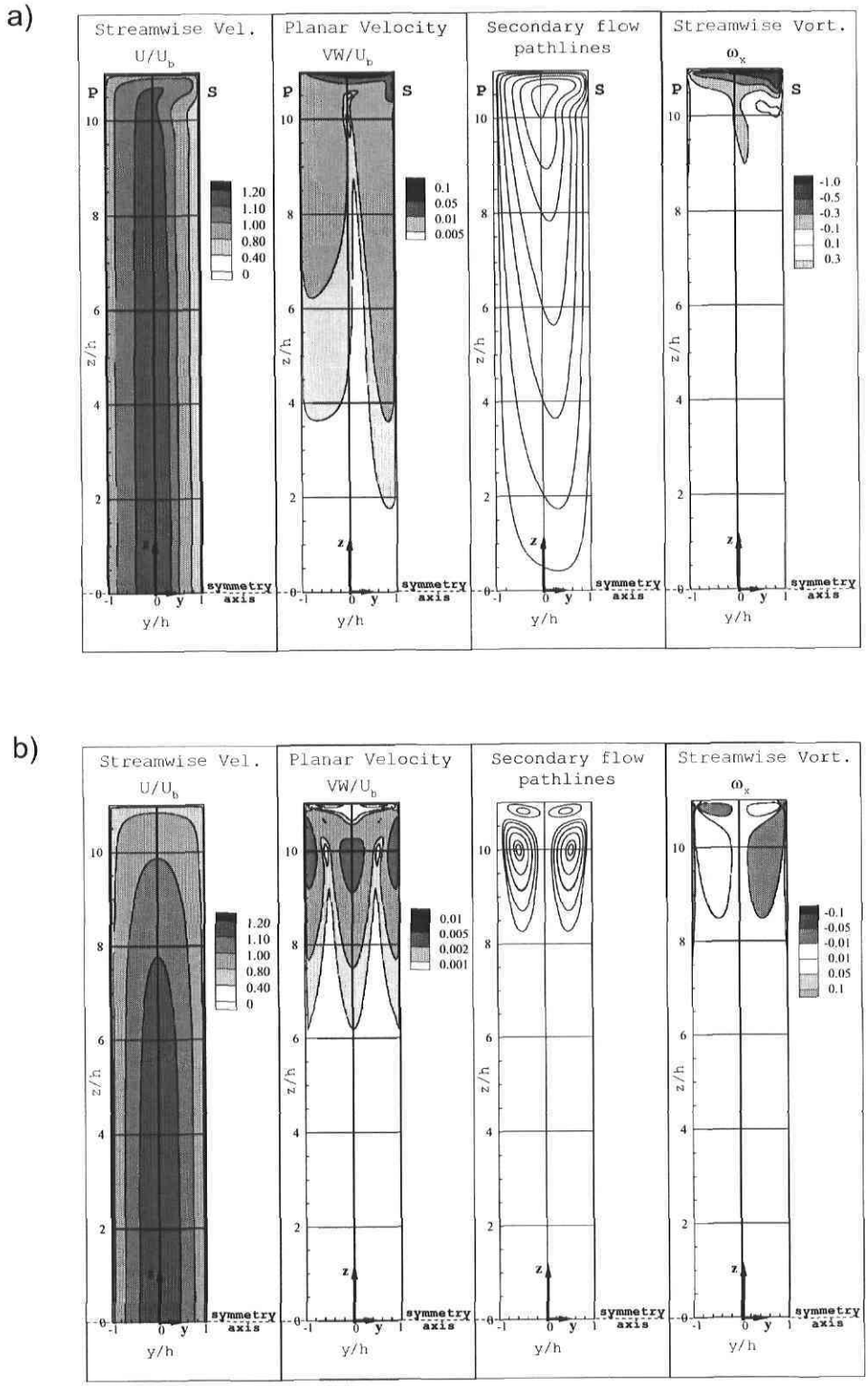

Figure 5.10: Plane contours of a duct at $Re = 40000$. (a): $Ro = 0.11$; (b): $Ro = 0$. Flow direction toward the observer.

by the secondary flow is due to the fact that the velocity gradient ($\partial U/\partial y$) in the central portion of the duct is lower at $Ro = 0.11$.

In the non-rotating case, the secondary flow effects on the streamwise velocity profile are negligible since the transverse velocity at the symmetry plane is close to being null ($V \approx 0.001\%U_b$). The effect of the secondary flow on the turbulent quantities is not discussed here since it is addressed in the paper by Julien *et al.* (2006).

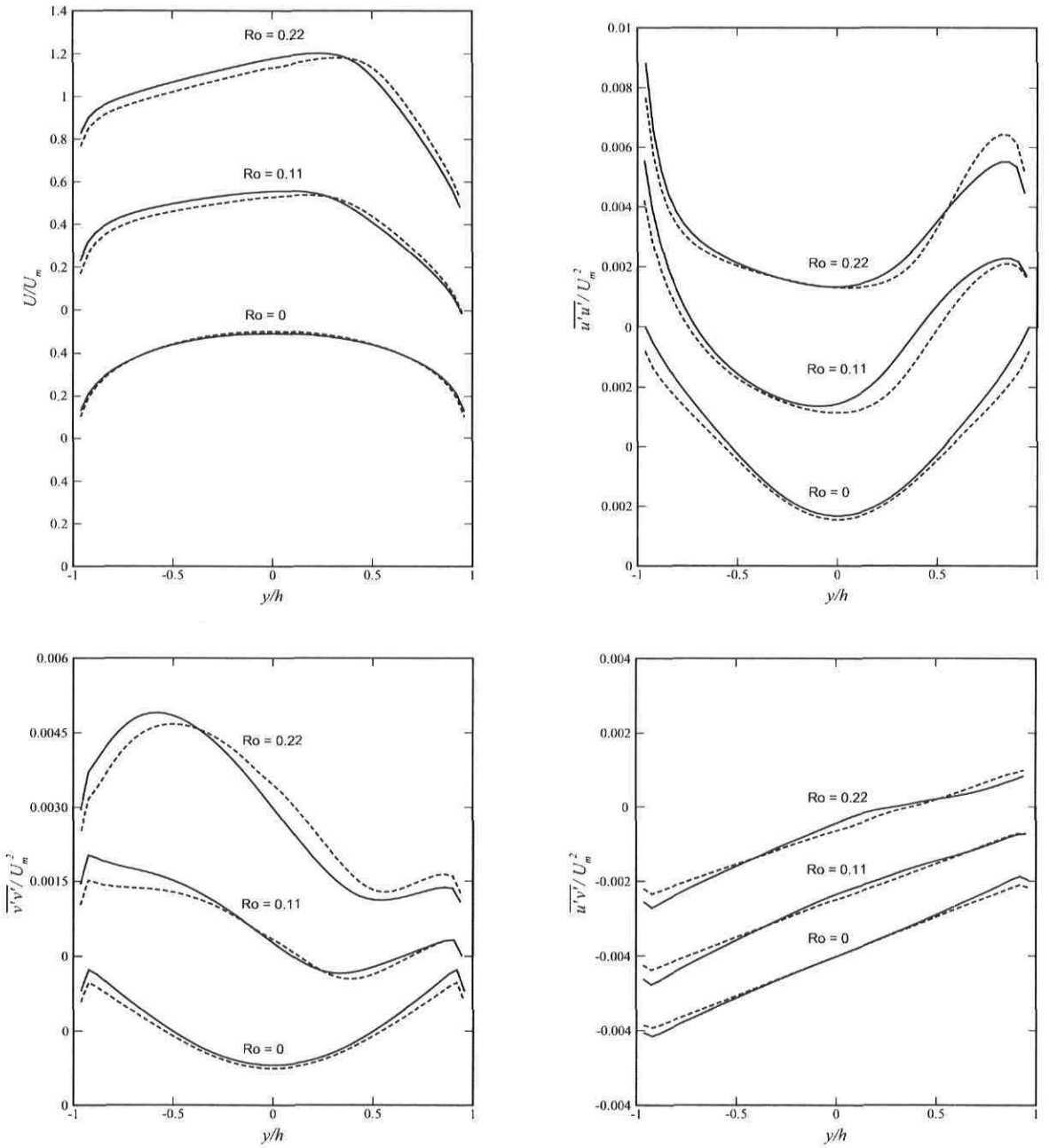

Figure 5.11: Velocity and Reynolds stress profiles of a duct and channel at $Re = 40000$. —, 3D case (at symmetry plane); – –, 2D case. U_m is the mean velocity at the symmetry plane.

It has been shown previously that even for moderate rotation rates, the secondary flow has a noticeable effect on the streamwise velocity profile at the symmetry plane of the duct. It is now important to verify if the Reynolds number has a significant impact on the dynamics of the cross-stream current. In order to do so, the Rotation number is kept constant at 0.22 and the Reynolds number is varied between 10000 and 40000.
The contours of streamwise vorticity of FIG. 5.13 suggest that, as the Reynolds number decreases, the Ekman layer becomes thicker and the maximum of ω_x decreases. The reduction in the maximum intensity of the streamwise vorticity is due to the fact that the spanwise velocity gradient is smaller at lower Reynolds. The thickening of the Ekman layer is expected for lower Reynolds numbers since diffusion becomes more important.
The force driving the secondary flow ($\partial p/\partial y$) has the same intensity in all three flows since the Rotation number is kept constant, but the velocity gradient becomes smaller for decreasing Reynolds. Consequently, the disequilibrium between the Coriolis and pressure forces persists on a larger portion of the duct. This results in a small increase in the flow rate associated with the secondary flow, but has a negligible repercussion on the velocity of the cross-stream current at the symmetry plane of the duct ($V/U_b \approx 0.1\%$). Therefore, the Reynolds number does not have a significant impact on the dynamics of the secondary flow.
Even though the transverse velocity (V) at the symmetry plane is similar at all three

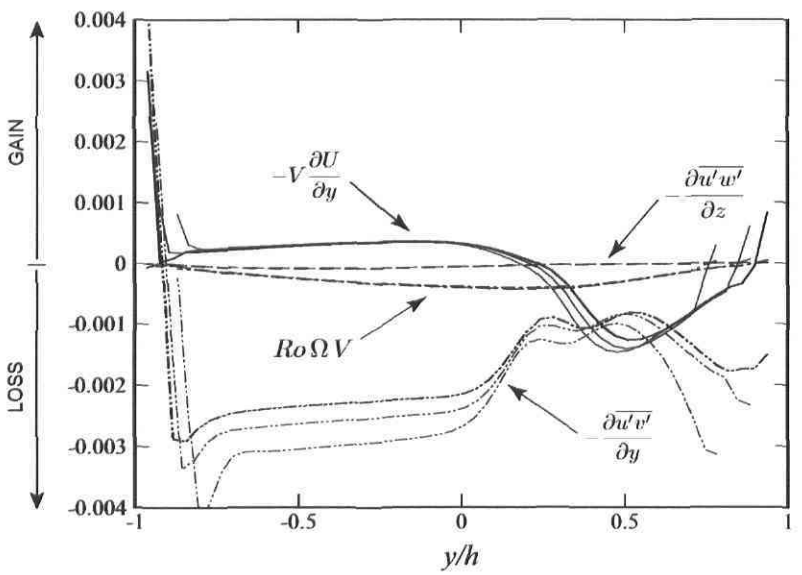

Figure 5.12: Turbulence and secondary flow contributions to the x-momentum equation at the symmetry plane of a rotating duct at $Ro = 0.22$. Black lines: $Re = 40000$; red lines: $Re = 20000$; green lines: $Re = 10000$.

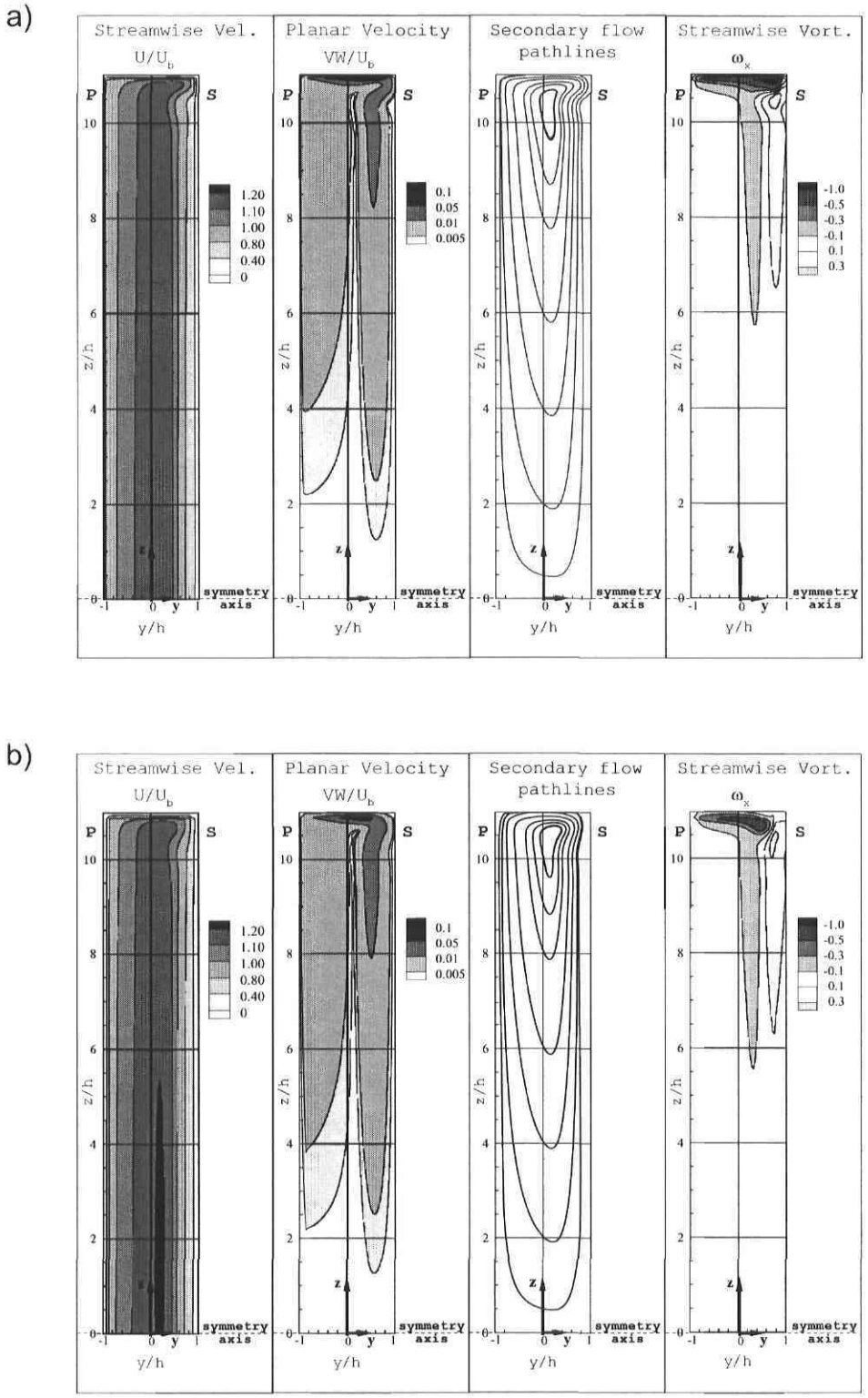

Figure 5.13: Plane contours of a duct at $Ro = 0.22$. (a): $Re = 20000$; (b): $Re = 10000$. Flow direction toward the observer.

flow regimes, the effect of the secondary flow on the streamwise velocity profile differs (see FIG. 5.14). As illustrated in FIG. 5.12, the advection term $V\partial U/\partial y$ responsible for the transport of momentum, becomes smaller on the suction side of the duct as the Reynolds number decreases, and its minimum value shifts toward the center of the duct.

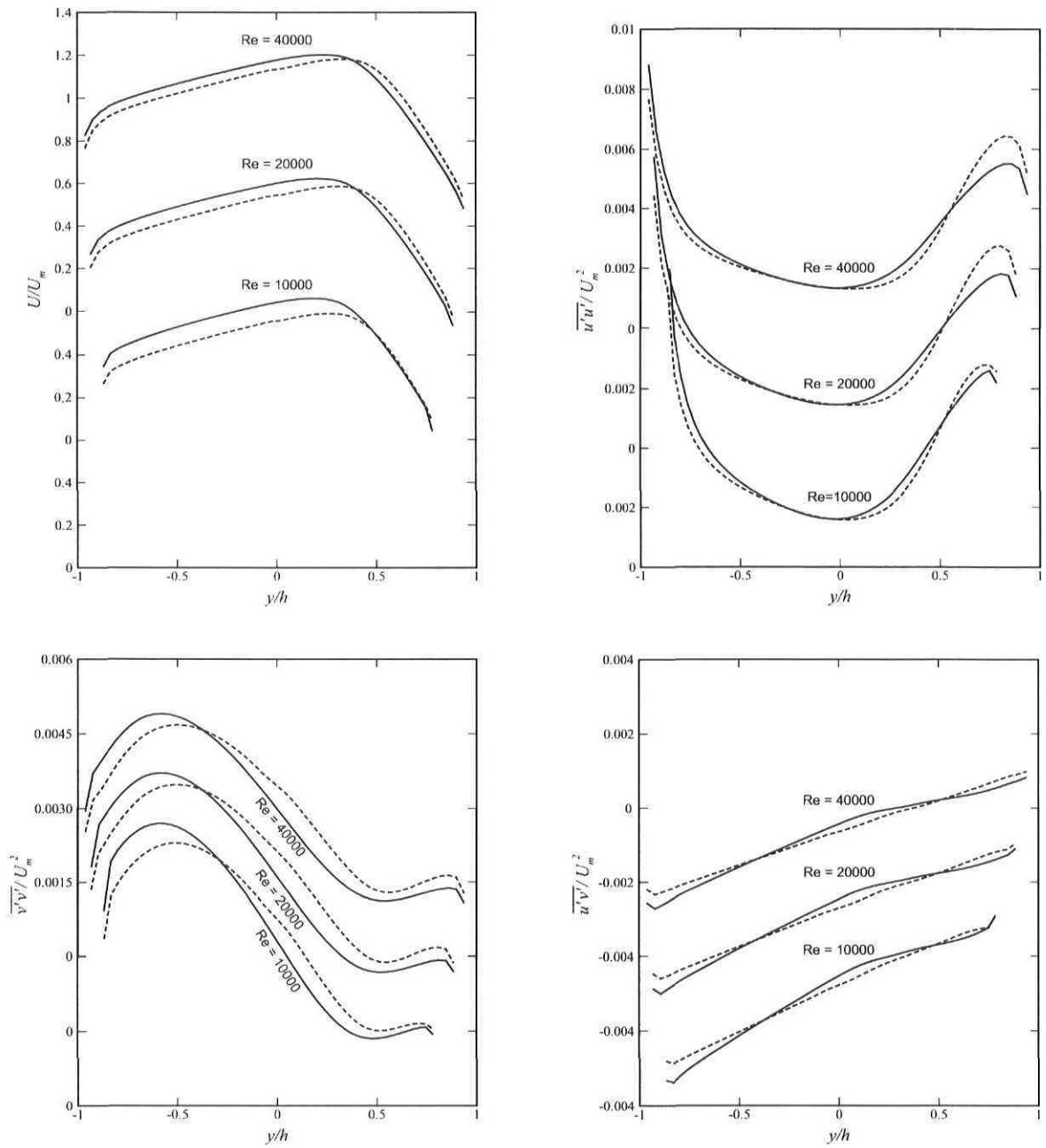

Figure 5.14: Velocity and Reynolds stress profiles of a duct and channel at $Ro = 0.22$. ——, 3D case (at symmetry plane); – –, 2D case. U_m is the mean velocity at the symmetry plane.

On the opposite, the advection term remains the same for all three regimes in the region of constant slope ($\partial U/\partial y \approx 2\Omega$).

Reynolds number	RMS norm
10000	0.0656
20000	0.0529
40000	0.0470

Table 5.7: $\|\triangle_{2D}\|_{RMS}$ values of streamwise velocity at the symmetry plane of a rotating duct at $Ro = 0.22$.

The RMS values of TABLE 5.7 indicate that the difference between the velocity profile of the 2D and 3D ducts increases as the Reynolds decreases. Therefore, the global effect of the secondary flow on the streamwise velocity weakens with increasing Reynolds number.
In conclusion, the Reynolds number does not have a direct impact on the intensity of the secondary flow (especially at the symmetry plane), but it does affect the degree of discrepancy between the 2D and 3D velocity profiles.

5.2.4 Comparison between experimental and DNS data

As it was mentioned in the introduction of chapter 5, one of the goals of this numerical study is to help explain the discrepancies between the experimental results (Maciel *et al.*, 2003) and the DNS data (Alvelius *et al.*, 1999). The DNS simulation is performed on a hexahedral domain where periodic conditions are applied in both the streamwise and spanwise direction in order to compute the fully developed solution in a rotating duct of infinite aspect ratio. In the experimental setup (FIG. 1.1), the duct has a finite aspect ratio ($AR = 11$) and it has a length of $160h$.
Even though the numerical simulation and the experiment are performed at the same Reynolds and Rotation numbers, the streamwise velocity profiles at the symmetry plane of the two ducts do not match perfectly (FIG. 5.15). This discrepancy is not caused by a lack of flow development in the experimental duct since the evolution of the velocity profiles between the stations at $x/h = 80$ and $x/h = 135$ is very small ($\partial U/\partial x \approx 0$). Therefore, it is reasonable to suppose that even at a distance greater than $135h$, the experimental profile will still differ from the DNS results.
The reason for this divergence is that the experimental duct is bounded by upper and lower walls and consequently a secondary flow is generated. As it was demonstrated in the previous sections, the intensity of the cross-stream current at the symmetry plane is very small ($V \approx 0.1\%U_b$ at $Re = 10000$) and difficult to detect experimentally,

but it is sufficient to cause a noticeable momentum transport in the velocity profile. Consequently, experimentalists should be aware of the presence of a secondary flow in a rotating duct, and be careful when comparing experimental data with results obtained

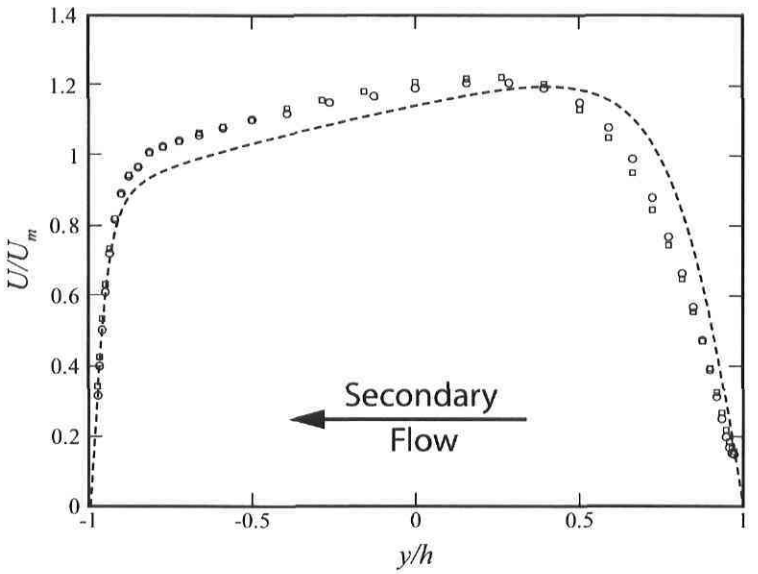

Figure 5.15: Experimental streamwise velocity profile at the symmetry plane of a rotating duct at $Re = 2897$ and $Ro = 0.22$ (Maciel *et al.*, 2003). $\square, x/h = 80$; $\bigcirc, x/h = 135$; – –, DNS (Alvelius *et al.*, 1999).

from numerical simulation of theoretical 2D ducts. Moreover, the presence of a quasi two-dimensional zone ($\partial U/\partial z \approx 0$) in a rotating duct of finite aspect ratio should not be taken as a proof that the solution corresponds to the theoretical 2D case.

Chapter 6

Flow development in a rotating channel

At first, the effect of rotation on the flow development in a channel ($AR = \infty$) is investigated, and the development length for a non-rotating and a rotating channel at $Re = 40000$ is compared.
Then, the design of the experimental setup is tested by comparing the development length between a rotating channel having uniform inlet conditions (same as in a settling chamber) and a more realistic 2D model of the actual experimental duct. In the latter, two lateral feeding channels, merging after a 180° turn, are placed upstream of the main channel (FIG. 1.1) in order to "pre-develop" the flow in terms of its z-vorticity and turbulence. The use of a settling chamber at the entrance of the main channel was discarded because of strong centrifugal forces and size restrictions.

6.1 Effect of rotation on flow development

The main objective is to determine whether rotation has a beneficial or a detrimental effect on the flow development. To verify that, a long channel ($L = 350h$) having a uniform velocity inlet with no turbulence is considered. The degree of flow development is estimated by comparing the streamwise velocity and turbulent viscosity profiles at different stations along the channel with the fully developed solution. Moreover, the RMS norm of the difference is computed at each position.
The study is performed for a turbulent flow at $Re = 40000$ and the Rotation number is fixed at 0.22, for the rotating case.

6.1.1 Mesh independence

Mesh independence is tested in order to insure that the chosen discretization in the transverse and streamwise directions is adequate. The investigation is carried on the flow development in a long rotating channel at $Re = 40000$ and $Ro = 0.22$. Two grids on a domain having a length of $250h$ and a uniform velocity inlet with no turbulence are built.
The standard mesh has 51 and 770 cells in the transverse and streamwise direction respectively. The size of the cells in the x-direction varies from $0.1h$ (at the inlet) to $0.4h$ (at the outlet). This mesh is shown in FIG. 6.1. The refined domain has 77 and 1160 cells in the transverse and streamwise direction respectively and the cell size in the x-direction varies from $0.07h$ to $0.27h$.

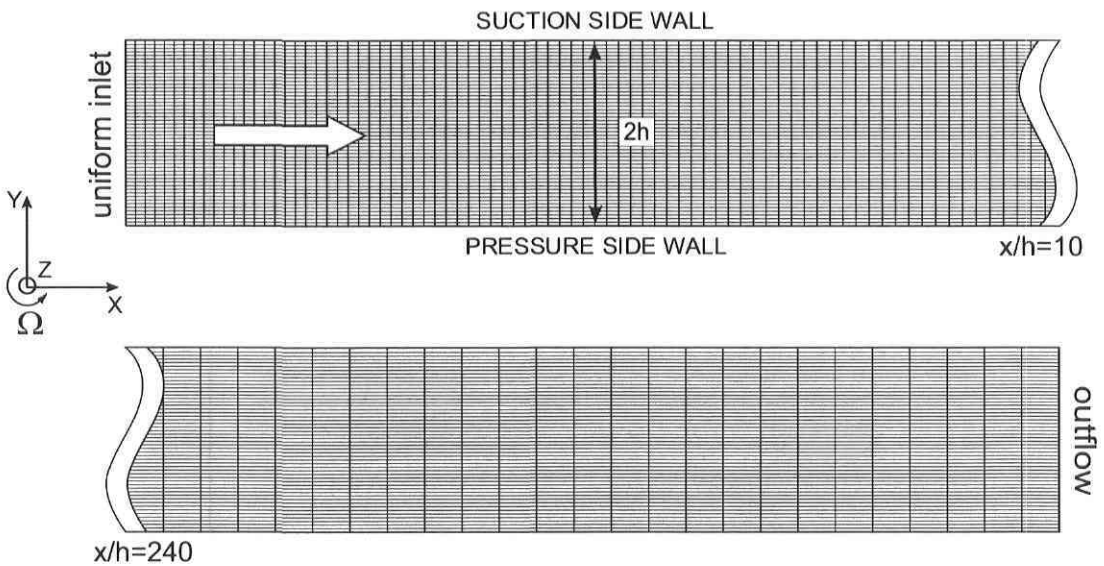

Figure 6.1: Standard mesh for studying the flow development in a rotating channel at $Re = 40000$ and $Ro = 0.22$.

To validate mesh independence, the streamwise velocity and the turbulent viscosity ratio are plotted at different stations along the rotating channels. As indicated by FIG. 6.2, there is an excellent agreement between the results obtained with the standard and

RMS norm	$x/h = 10$	$x/h = 50$	$x/h = 100$	$x/h = 200$
Streamwise velocity (U/U_b)	0.00151	0.00191	0.00163	0.00282
Viscosity ratio (ν_t/ν)	0.085	0.047	0.0088	0.014

Table 6.1: $\|\triangle\|_{RMS}$ values at different stations along a rotating channel at $Re = 40000$ and $Ro = 0.22$.

refined meshes, since the profiles are practically superimposed.
The RMS norm of the difference is also computed at each position for the two quantities (see TABLE 6.1), and it confirms the similarity between the two solutions. The high value of the RMS norm at $x/h = 10$ (for the turbulent viscosity ratio) is due to the small sampling size. In fact, a large portion of the ν_t/ν profile is null at this position, and is not included in the RMS calculation.

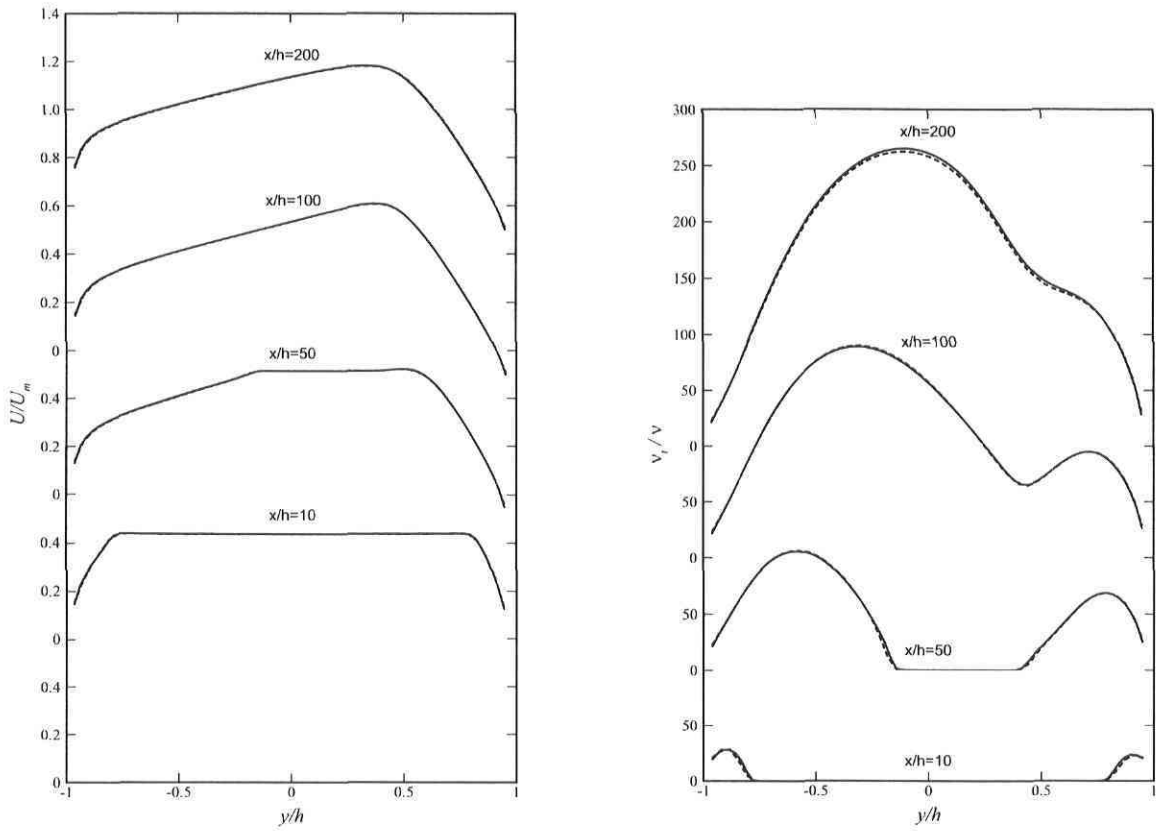

Figure 6.2: Streamwise velocity and turbulent viscosity ratio profiles at different stations along a rotating channel at $Re = 40000$ and $Ro = 0.22$. ——, Fine mesh; – –, standard mesh.

In conclusion, it has been proven that the standard mesh (with 39270 elements) is adequate for studying the flow development in a rotating channel. This mesh discretization will be used in subsequent 2D flow development calculations for both rotating and non-rotating cases.

6.1.2 Flow development in a rotating and non-rotating channel

In this section, the development length in a rotating and non-rotating channel at $Re = 40000$ is compared. In both cases, the total length of the channel is $350h$ ($250h + 100h$). The first section has a uniform velocity profile with no turbulence as inlet condition and an *outflow* as exit condition. The $100h$ extension has the flow solution from the first section (at $x/h = 240$) as inlet condition and an *outflow* condition at the exit. The meshes for the rotating and non-rotating cases have the same discretization: 39270 elements in the first section (see FIG. 6.1), and 12750 elements in the $100h$ extension. However, the size of the wall adjacent cells differ in order to have a $y^+_{\text{fc}} \approx 40$ on both walls. This implies a symmetric grid for the non-rotating case but an asymmetric one for the rotating case.

The evolutions of the velocity profiles for the rotating and non-rotating channels are compared in FIG. 6.3. The first remark is that, for the rotating case, the rotational zone develops much faster on the pressure side than on the suction side of the channel. For example, at $x/h = 50$ the irrotational portion of the asymmetric profile extends from $-0.06 < y/h < 0.32$ whereas it ranges from $-0.17 < y/h < 0.17$ in the non-rotating case. At this rotation rate ($Ro = 0.22$), the Coriolis force has a destabilizing effect on the pressure side of the channel. Therefore, the turbulent activity is amplified on the pressure side, and it causes a faster growth of the boundary layer. On the opposite, the boundary layer develops more slowly on the suction side because in this region the Coriolis force has a stabilizing effect.

A parameter often used to measure the distance required for turbulence effects to cover the entire width of the channel is the entrance length (L_e). This length is estimated to be $72h$ and $64h$ for the rotating and non-rotating cases respectively. Hence, the flow reaches full development faster in the non-rotating case than in the rotating one. This result can be explained by computing the rate of development of the boundary layer. In order to do so, the thickness of this layer (δ) is compared at two different stations along the channel, $x/h = 10$ and $x/h = 50$ respectively. On the pressure side of the rotating channel $\delta_{x=50h}/\delta_{x=10h} = 2.98$, whereas it is equal to 2.35 on the suction side. In the non-rotating case, $\delta_{x=50h}/\delta_{x=10h} = 2.91$ on both sides. It is clear that, overall, the boundary layer develops at a slower rate in the rotating case, thus resulting in a longer entrance length.

The rate of development of the boundary layer in the rotating and non-rotating channel can be compared with the development of a boundary layer on a flat plate. For a turbulent flow, the thickness of the boundary layer is approximately proportional to $x^{4/5}$. Between $x/h = 10$ and $x/h = 50$, this estimate gives $\delta_{x=50h}/\delta_{x=10h} = 3.62$. This ratio is significantly higher than the one computed for the non-rotating channel. It is important to remember that the formula for the flat plate implies a zero pressure gradient ($\partial p/\partial x$=0), whereas the flow in the channel is pressure driven.

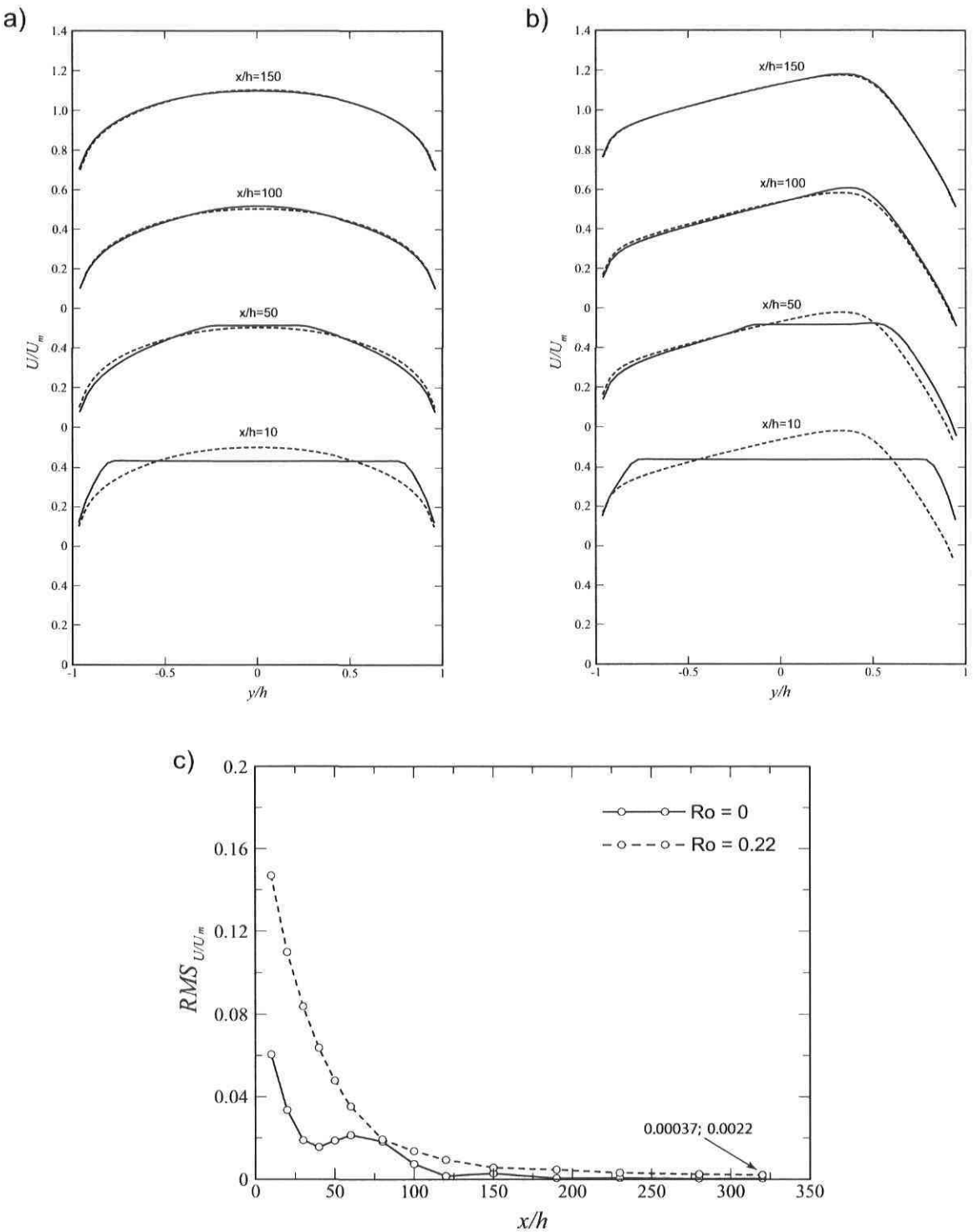

Figure 6.3: Streamwise velocity profiles at different stations along a channel at $Re = 40000$. ——, Solution at measurement station; – –, fully developed solution. (a): $Ro = 0$; (b): $Ro = 0.22$. (c): $\|\triangle_{FD}\|_{RMS}$ norm of the difference.

Moreover, in the channel, the pressure gradient is favourable ($\partial p/\partial x < 0$) and such gradients tend to reduce the growth of the boundary layer. For the rotating channel, the growth rate of the boundary layer on the pressure side is very close to the rate in the non-rotating channel ($\propto x^{0.68}$), but on the suction side this rate is much smaller ($\propto x^{0.53}$). If the latter is compared with the growth rate of a laminar boundary layer on a flat plate ($\delta_{x=50h}/\delta_{x=10h} \propto x^{1/2} = 2.24$), the values are found to be analogous. Even though relaminarization has not occurred on the suction side of the channel (see profiles of ν_t/ν in FIG. 6.4), the stabilizing effect of rotation combined with the favourable pressure gradient produce a growth rate similar to the one found in a laminar boundary layer.

Although the previous method allows to estimate the flow development in a channel, a more accurate approach is to compute the RMS norm of the difference between the fully developed solution and the solution at a given downstream section. The criteria chosen here for stating that the flow is fully developed is a RMS value smaller than 0.5%. The evolution of the RMS norm is plotted in FIG. 6.3c for the velocity profile in the rotating and non-rotating channels. The fully developed (f.d.) criteria is reached after a length of $175h$ and $105h$ for the rotating and non-rotating case respectively. These results confirm once again that the flow development in the rotating channel is slower than in a non-rotating channel.

The evolution of the turbulent viscosity was also investigated in the present study, and is shown in FIG. 6.4. The first observation is that, at both Rotation numbers, the turbulent viscosity develops more slowly than the streamwise velocity. Consequently, the turbulent quantities require a greater distance to reach a fully developed state. If the same f.d. criteria is considered, turbulence has not attained the fully developed state even after a length of $320h$. The second remark is that the turbulent region grows faster on the pressure side than on the suction side of the rotating channel. As expected, the level of turbulent viscosity near the pressure side is higher than on the suction side and, in the f.d. state, is almost twice the value obtained for $Ro = 0$. The turbulent viscosity has a direct effect on the thickness of the boundary layer. Even though the boundary layer on the pressure side develops at a rate similar to the one found in the non-rotating case, its thickness is greater in the rotating case ($\delta = 0.94h$ instead of $0.83h$ at $x/h = 50$). If the analogy with the flat plate is considered once again, it indicates that the thickness of the turbulent boundary layer diminishes as the Reynolds number increases. Since the effective Reynolds number ($Re_{eff} = 1/(\nu_t + \nu)$) is smaller at $Ro = 0.22$, the boundary layer will be thicker in the rotating case.

In conclusion, the results have shown that the development of a turbulent flow in a rotating channel (at $Ro = 0.22$) is slower than in a non-rotating channel. At high Ro, where rotation has a stabilizing effect on both the pressure and suction sides of the channel, the difference in the development lengths should become even greater. It was also noted that the distance required to reach full development is much longer for

turbulence than for mean momentum.

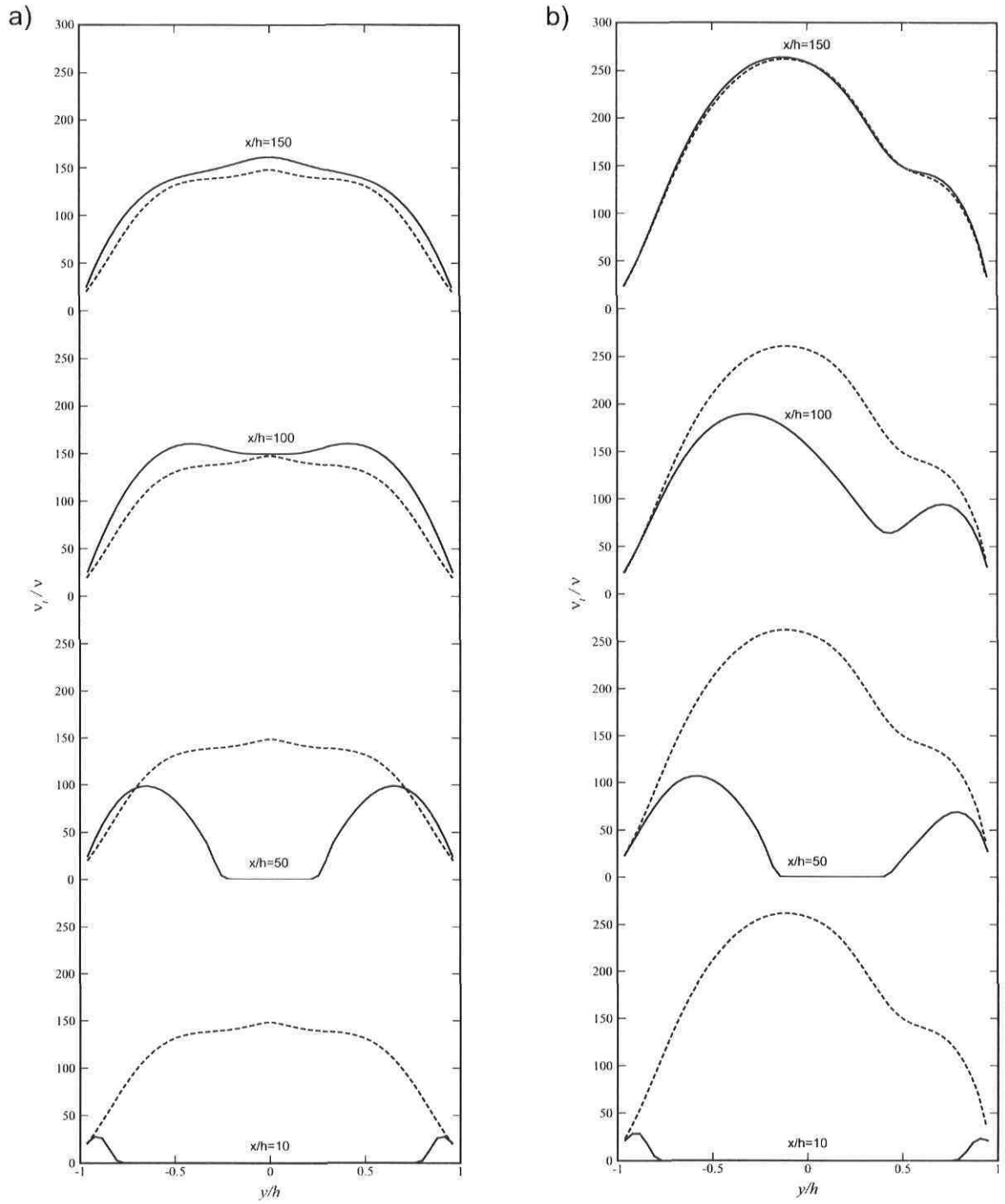

See caption next page.

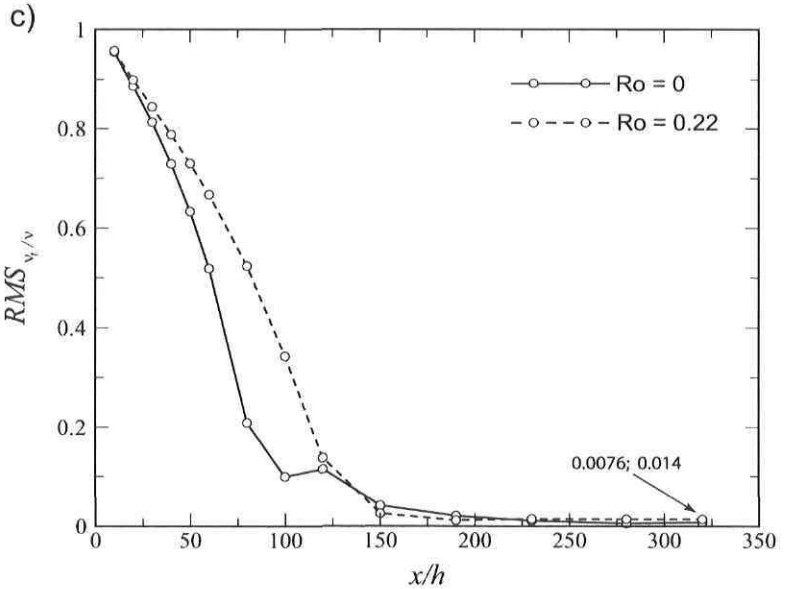

Figure 6.4: Turbulent viscosity ratio profiles at different stations along a channel at $Re = 40000$. ——, Solution at measurement station; – –, fully developed solution. (a): $Ro = 0$; (b): $Ro = 0.22$. (c): $\|\triangle_{FD}\|_{RMS}$ norm of the difference.

6.2 Validation of the design hypothesis

An experimental rotating duct was built in the Experimental Fluid Mechanics Laboratory at Laval University in order to study the effects of the Coriolis force on turbulence. During the design process, the use of a settling chamber at the entrance of the main channel was discarded because of strong centrifugal forces and size restrictions. Instead, two lateral feeding channels, merging after a 180° turn, were placed at the entrance of the main channel. The setup is illustrated in FIG. 1.1.

The hypothesis behind such a design is that the secondary channels will contribute to "pre-develop" the flow in terms of its z-vorticity and turbulence. In the following section, the validity of this hypothesis is tested via numerical simulations.

The tests are first carried on a 2D version of the actual 3D setup in order to determine if the pre-development is beneficial in the case of a duct with an infinite aspect ratio. To reduce the complexity of the problem, the domain considered here includes only the last portion of the lateral channels ($4h$), the bends, the merging area and the first $140h$ of the main channel. As shown in FIG. 6.5, the location of the rotation axis in the computational domain is placed at the channel exit (as required by *Fluent*), whereas in the experimental setup it is situated at the center of the channel. This modification

is not problematic since the flow solution is independent of the location of the rotation axis. Finally, in the computational domain the reference axis is placed at the inlet of the main channel.

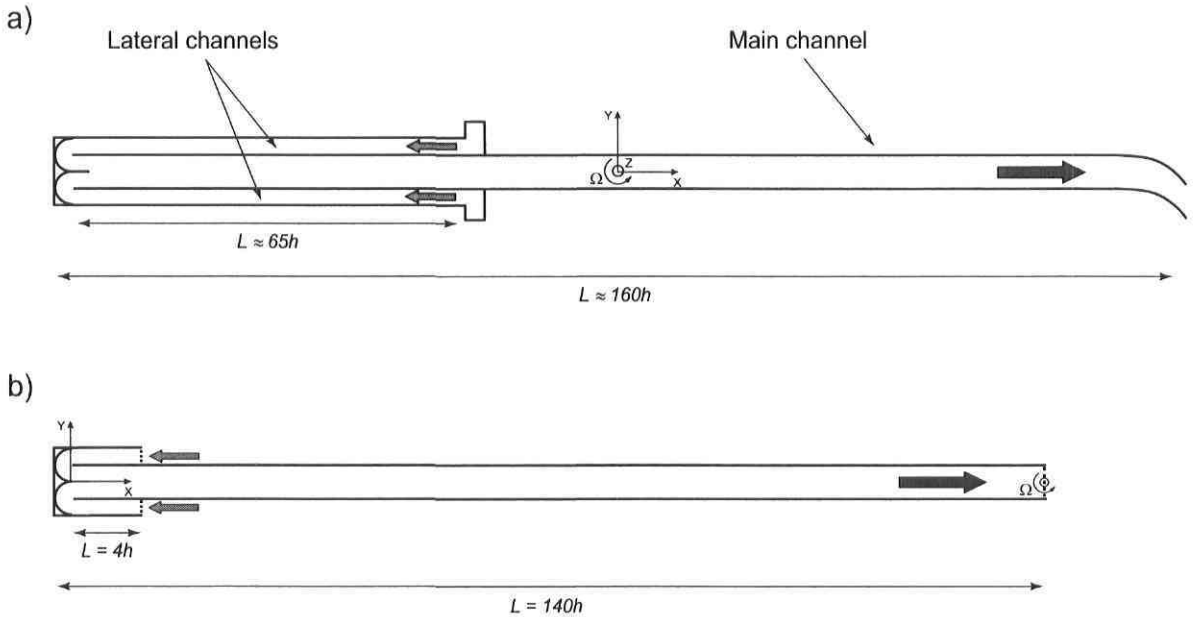

Figure 6.5: (a): Top view of experimental setup; (b): 2D computational domain.

The mesh discretization in the actual rotating channel is illustrated in FIG. 6.6. The grid has about 37000 cells. The main channel has 51 cells in the transverse direction whereas in the streamwise direction the cell size varies from $0.03h$ at the inlet to $0.4h$ at the outlet. Each 180° turn has 90 and 21 cells in the tangential and radial directions respectively. The size of the wall adjacent cells is adjusted to have a y^+_{fc} value close to 40.

As it was mentioned previously, only the last portion of the lateral channels is modeled in order to simplify the computational problem. Fully developed conditions, obtained from prior Poiseuille flow calculations with corresponding rotation, are set at the entrance planes of the domain. In the experimental setup, the flow has probably not reached the state of full development in the lateral channels at a distance of $4h$ from the 180° turn. However, it is not possible to set the "real" inlet conditions since no experimental data is available.

The numerical simulations are performed at a Reynolds number of 40000 and 20000 for a Rotation number of 0.22. The Reynolds numbers differ from experiments ($Re \approx 3000$), but they are chosen in order to have a reasonable wall-element size. It should be mentioned that, in the experimental setup, the maximum achievable Reynolds number at $Ro = 0.22$ is around 10000.

The evolution of the streamwise velocity along the straight channel (with a uniform inlet) and the actual channel is plotted in FIG. 6.7. The U profiles at $x/h = 5$ show

that, at both Reynolds numbers, there is a separation bubble on the suction side of the actual channel. The presence of actually two separations zones is best seen with the

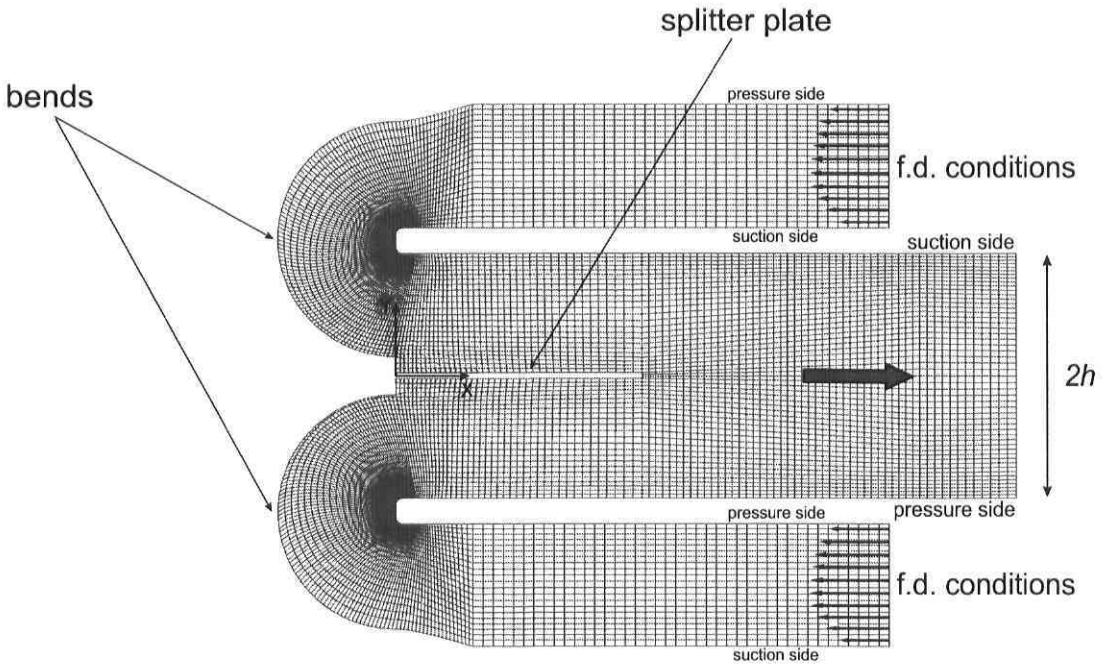

Figure 6.6: Inlet section of computational domain. Mesh discretization for case study at $Re = 40000$ and $Ro = 0.22$.

streamlines contours of FIG. 6.8. As expected, the 180° turn is too sharp and the flow cannot remain attached to the inner side walls. The length of the separation bubbles is about $6h$ and $2.5h$ on the suction and pressure sides respectively. Since rotation has a stabilizing effect on the suction side of the channel, it is normal to have a larger separation zone in that region. At $Re = 20000$, the separation bubbles are longer (i.e., $7.5h$ and $2.8h$ on the stabilized and destabilized sides respectively), and they occupy a wider section of the main channel.

The recirculating regions cause a large momentum surplus in the central portion of the channel. However, the diffusion process is quite rapid, and around $x/h = 20$ the velocity profile nears the fully developed shape. The RMS norm of the difference even suggests that, at $Re = 40000$, the flow development is slightly better in the actual channel. At the last station ($x/h = 140$), the flow is very close to satisfying the fully developed criteria ($RMS < 0.5\%$) in both the straight and actual channels.

At the lower Reynolds number, the flow development in the actual channel is somewhat slower than in the straight channel because there is a greater velocity surplus in the central portion of the channel that must be diffused.

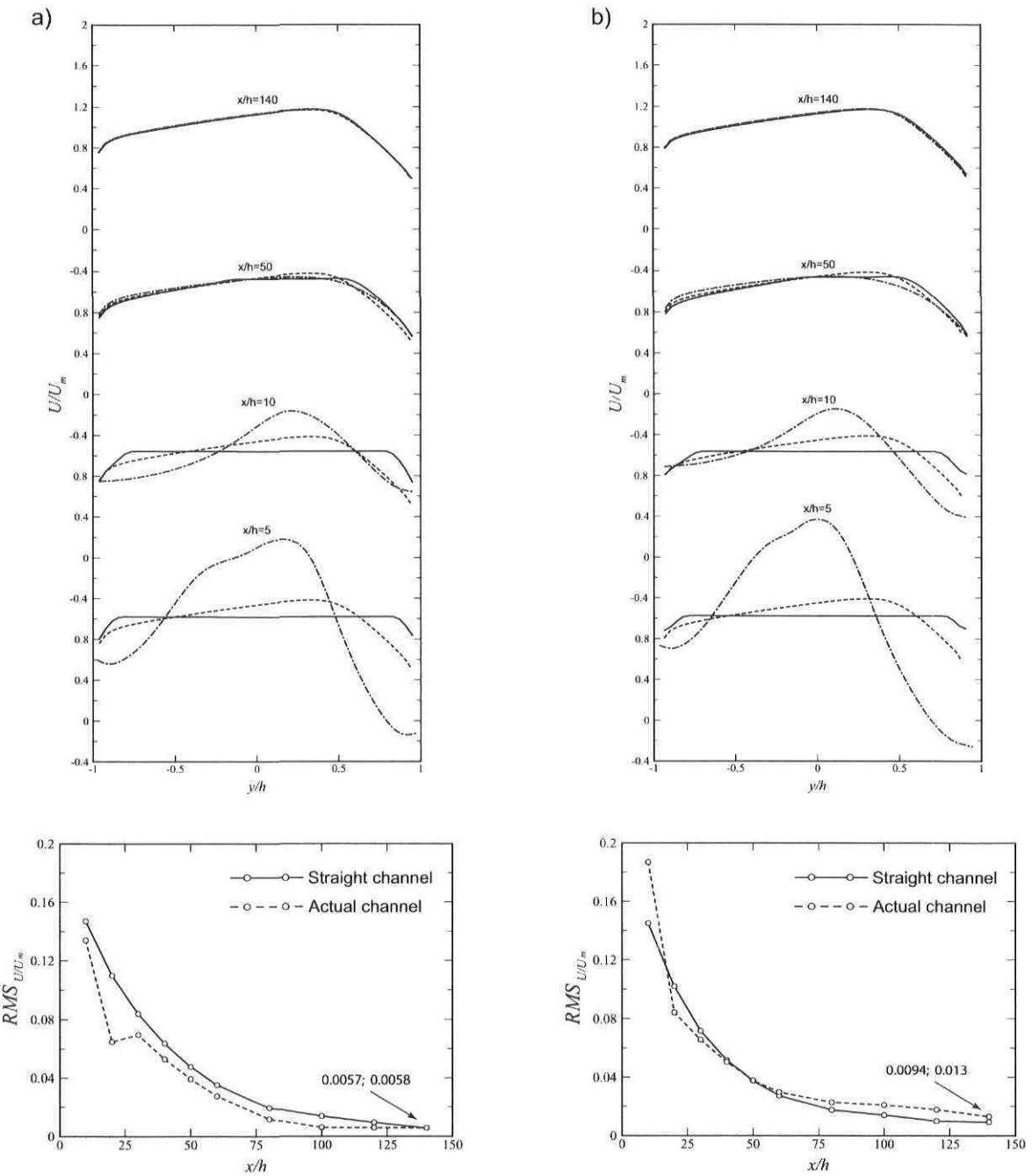

Figure 6.7: Streamwise velocity profiles and $\|\triangle_{FD}\|_{RMS}$ values at different stations along a rotating channel at $Ro = 0.22$. ——, Straight channel; — - —, actual channel; – –, fully developed solution. (a): $Re = 40000$; (b): $Re = 20000$.

The plots of turbulent viscosity at $x/h = 5$ and $x/h = 10$ (FIG. 6.9) may seem odd since they indicate a higher value of turbulent viscosity on the suction (stabilized) side than on the pressure (destabilized) side of the channel. Such behaviour is due to the large separation bubble on the suction side, which causes the shear layer to be still detached at $x/h = 5$, whereas it has reattached on the pressure side. In general, a detached shear layer is very unstable and is a source of turbulence.

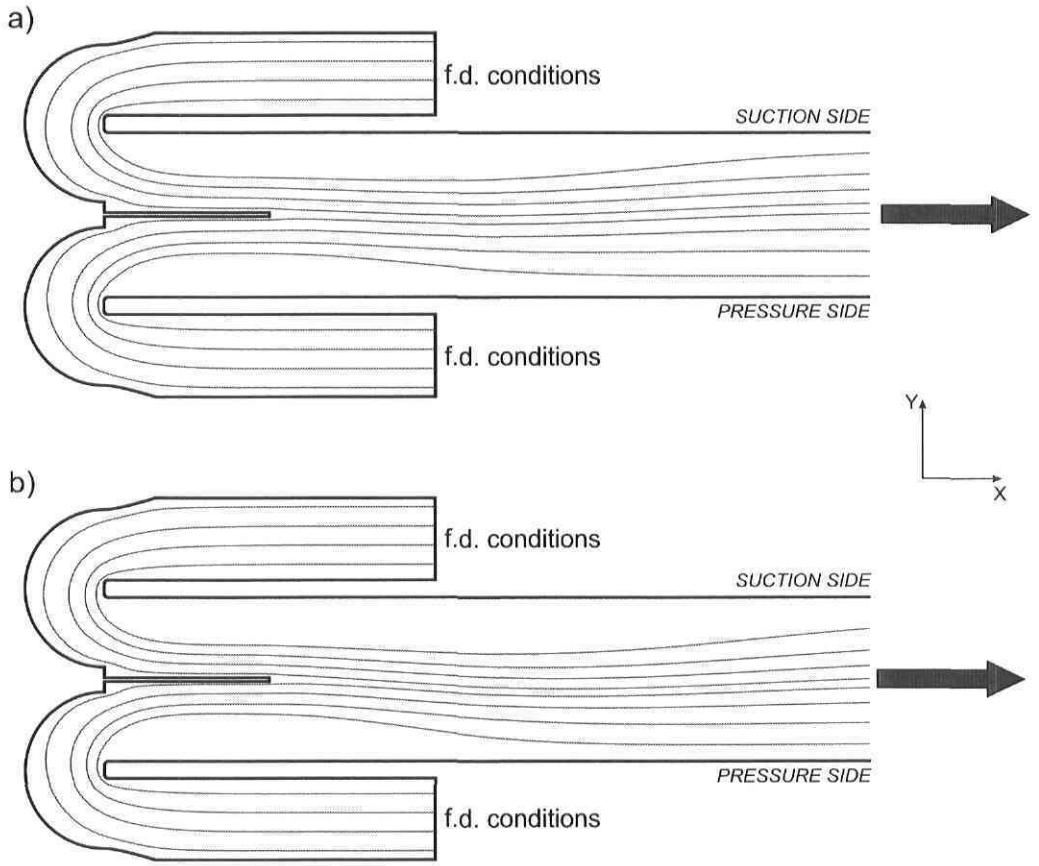

Figure 6.8: Streamlines in the entrance region of the actual channel at $Ro = 0.22$. (a): $Re = 40000$; (b): $Re = 20000$.

Overall, the development lengths in the straight channel with a uniform inlet and in the actual channel are very similar. The presence of lateral channels is indeed favourable to the turbulence production and to the pre-development of the velocity profiles, but most of the benefits are lost because of two large separation bubbles at the entrance of the main channel.

As it was mentioned in the introduction of this section, the flow in the lateral channels of the experimental setup is probably not fully developed at a distance of $4h$ from the 180° turn. However, the previous calculations were performed by setting a fully developed profile at the inlet of both channels. Hence, it is necessary to verify if the flow development is significantly affected when uniform conditions are applied instead. The computational domain and mesh discretization are the same as before (FIG. 6.6)

but a uniform velocity profile with a moderate level of turbulence ($\nu_t/\nu \approx 30$) is set as inlet conditions for the lateral channels.

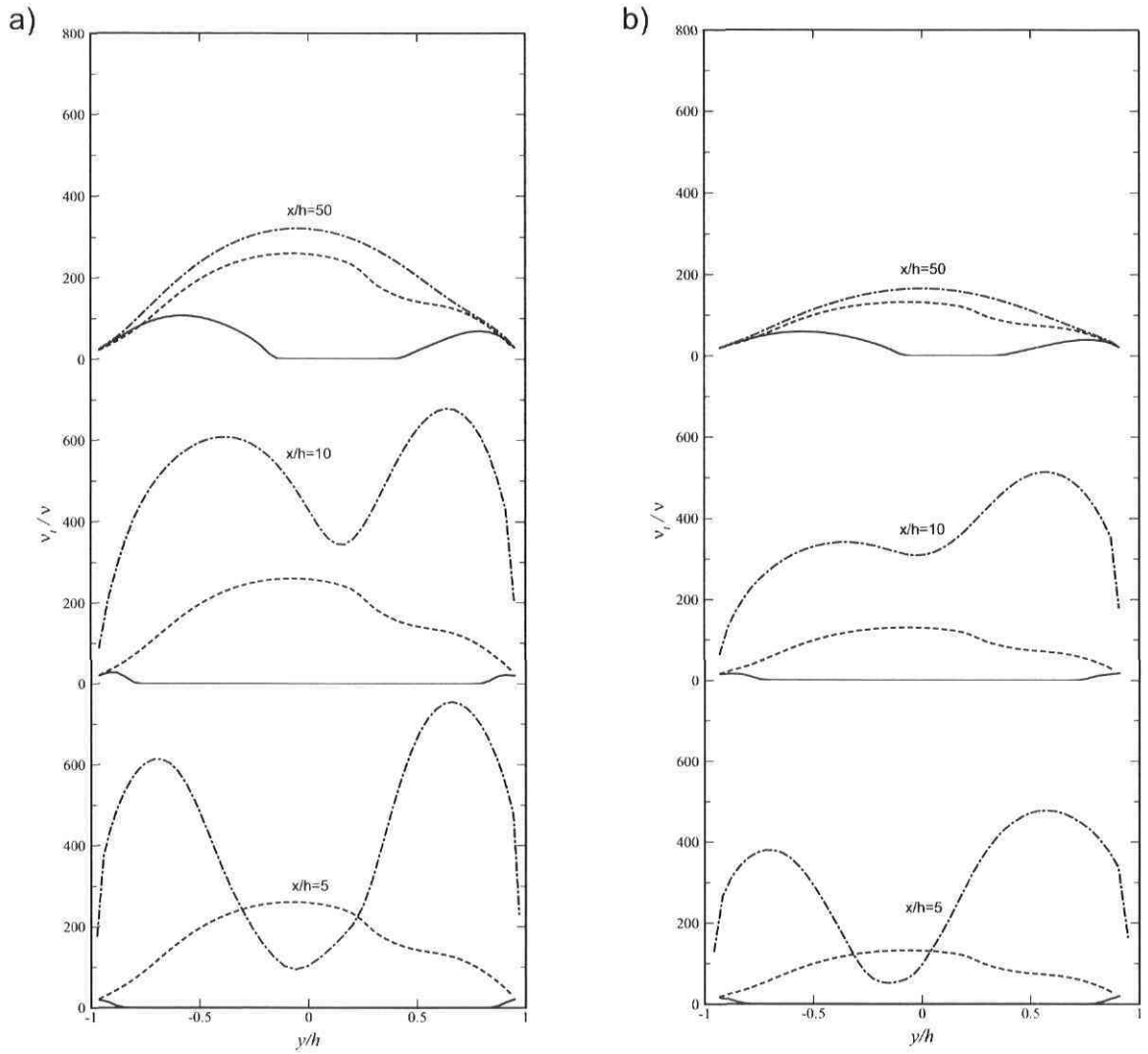

Figure 6.9: Turbulent viscosity ratio profiles at different stations along a rotating channel at $Ro = 0.22$. ——, Straight channel; — – —, actual channel; – –, fully developed solution. (a): $Re = 40000$; (b): $Re = 20000$.

The streamwise velocity is plotted in FIG. 6.10 at the same stations as before. At least qualitatively, the evolution of U is very similar to the previous case. At both Reynolds, two large separations bubbles appear near the entrance of the main channel and they persist over a length of $5.8h$ and $2.3h$ on the suction and pressure side respectively. They cause once again a flow acceleration in the central portion of the domain and this momentum surplus then diffuses throughout the channel.

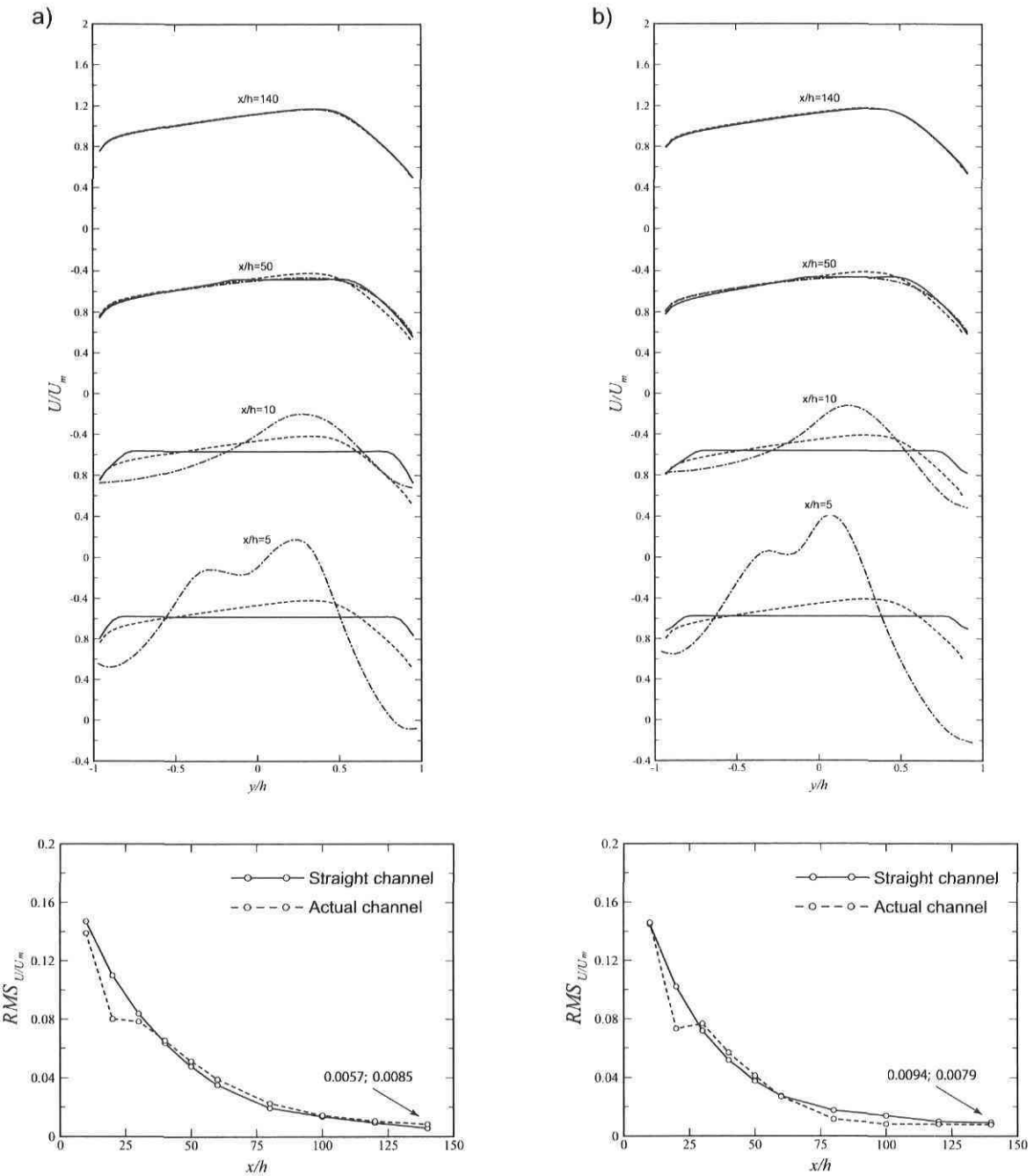

Figure 6.10: Streamwise velocity profiles and $\|\triangle_{FD}\|_{RMS}$ values at different stations along a rotating channel at $Ro = 0.22$. ——, Straight channel; — – —, actual channel; – –, fully developed solution. (a): $Re = 40000$; (b): $Re = 20000$.

The graphs of the RMS value show that, with the uniform inlet conditions, the flow development is slightly worse at $Re = 40000$ but it improves at $Re = 20000$, compared to the straight channel. One should remember that, when f.d. conditions were used, the opposite behaviour was observed. Nevertheless, the reader should keep in mind that the variations discussed here are very small (within 1%) and it is difficult to truly identify a pattern.

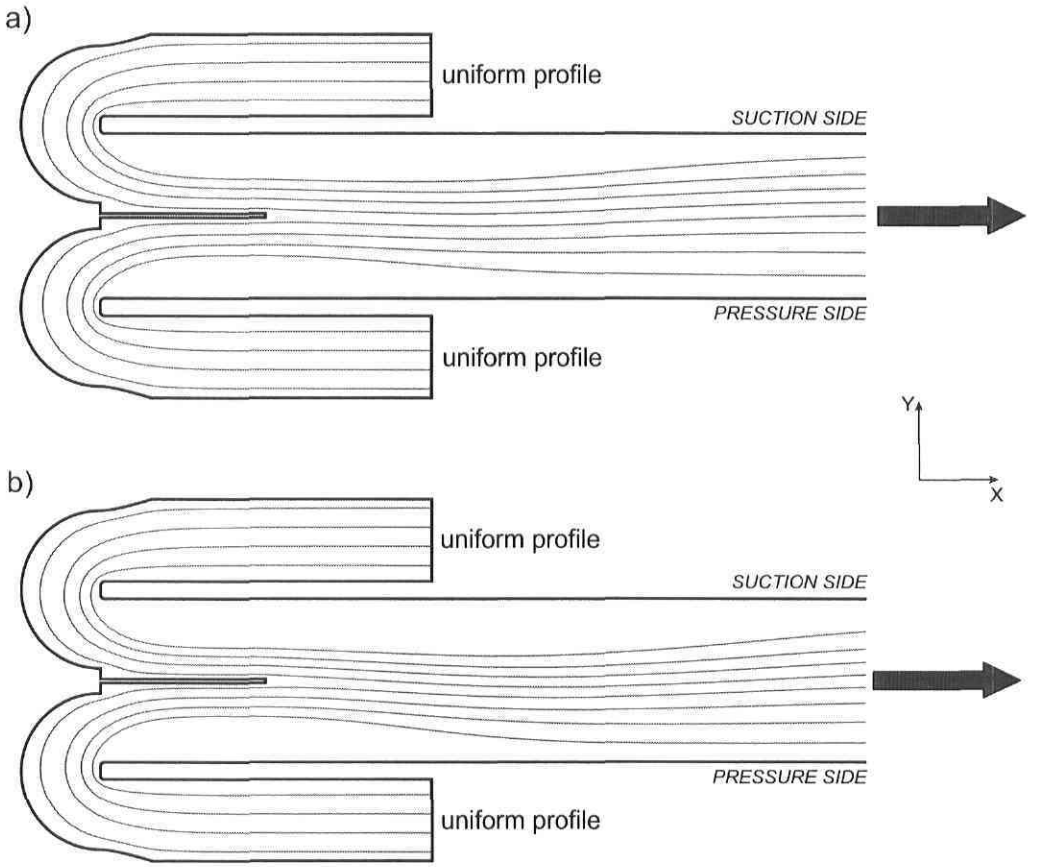

Figure 6.11: Streamlines in the entrance region of the actual channel at $Ro = 0.22$. (a): $Re = 40000$; (b): $Re = 20000$.

In summary, the flow development in the actual channel is much influenced by the presence of the 180° turns and the state of development in the lateral channels does not play a major role. The reason being that the centrifugal effect in the bends is very strong and it significantly deforms the velocity profile. Moreover, the separation bubbles cause a large flow acceleration in the center portion of the duct. The combination of those two effects cancels most of the benefits of having a pre-development in the lateral channels.

The computed results suggest that the flow development in the 2D version of the actual duct is very similar to the one that would be obtained by placing a settling chamber at the entrance of the main channel. The design hypothesis is not strictly verified in the sense that the pre-development in the lateral channel does not significantly reduce the

development length. However, at this stage, the design remains valid since it satisfies both size and force constraints, without deteriorating the flow development.

6.3 Improvements on the actual design

As it was stated in the previous section, 2D computations have shown that the flow development in the actual channel is not significantly better than the development from a settling chamber. However, certain modifications can be made to the present setup in order to reach the fully developed state more rapidly.
The main objective is to promote the flow development in the experimental setup, but also to eliminate all sources that may cause a pulsating flow (separations bubbles, wakes, etc.). Moreover the new design must satisfy the following conditions: 1) be symmetrical since the experimental setup may rotate in either the clockwise or counter clockwise direction during the data acquisition process; 2) be simple and easy to implement in the actual setup.

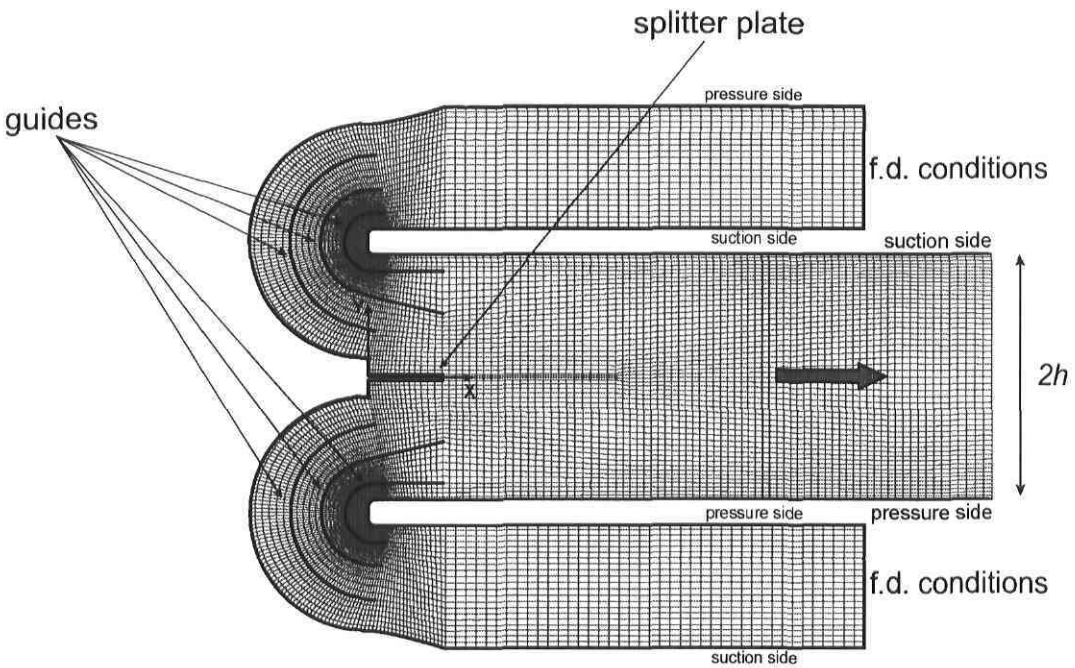

Figure 6.12: Inlet section of computational domain. Mesh discretization for case study at $Re = 40000$ and $Ro = 0.22$.

During the process of "trial and error", many configurations were tested, but only one respected all criteria. The final design is illustrated in FIG. 6.12, while others are presented in Appendix B. The selected configuration has a set of three circular guides placed in each 180° turn. The function of the guide closest to the interior of the bend

is to better redirect the incoming flow, and to eliminate the separation bubbles. The middle guide makes the flow slightly converge toward the splitter plate in order reduce the wake caused by the step and the outer guide is strategically placed in order to have a proper momentum balance across the channel. Finally, the splitter plate is shortened ($L = 0.6h$ instead of the previous $2h$) since it caused a momentum deficit in the center of the channel.

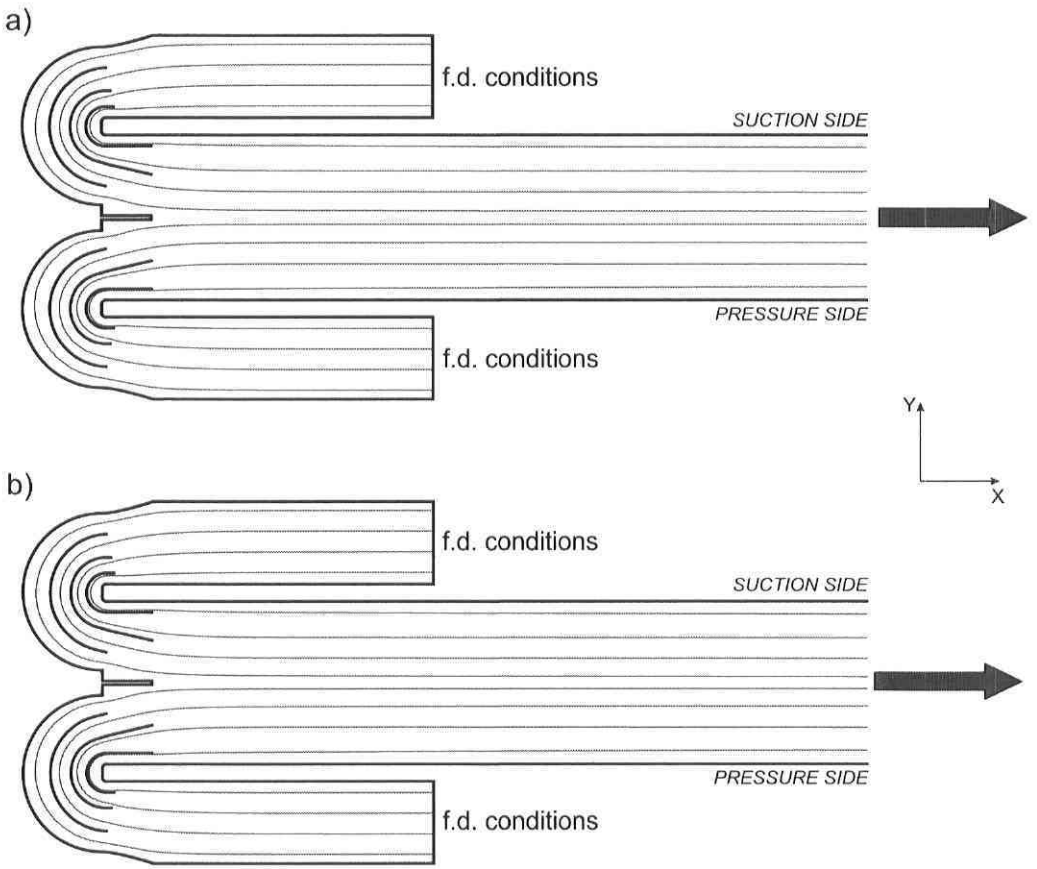

Figure 6.13: Streamlines in the entrance region of the modified channel at $Ro = 0.22$. (a): $Re = 40000$; (b): $Re = 20000$.

The new configuration is tested for the rotating case ($Ro = 0.22$) at two Reynolds numbers ($Re = 40000$ and $Re = 20000$) to insure that the design performs well over a reasonable range of flow regimes. The stream traces of FIG. 6.13 show that, at both Reynolds numbers, the guides are able to completely eliminate the separation bubbles at the entrance of the main channel. Moreover, the flow reattaches very quickly after the step thus reducing noticeably the wake size. As shown in FIG. 6.14, the removal of the two large separation regions has a profound effect on the shape of the velocity profile. In fact, momentum is now more uniformly distributed across the channel.

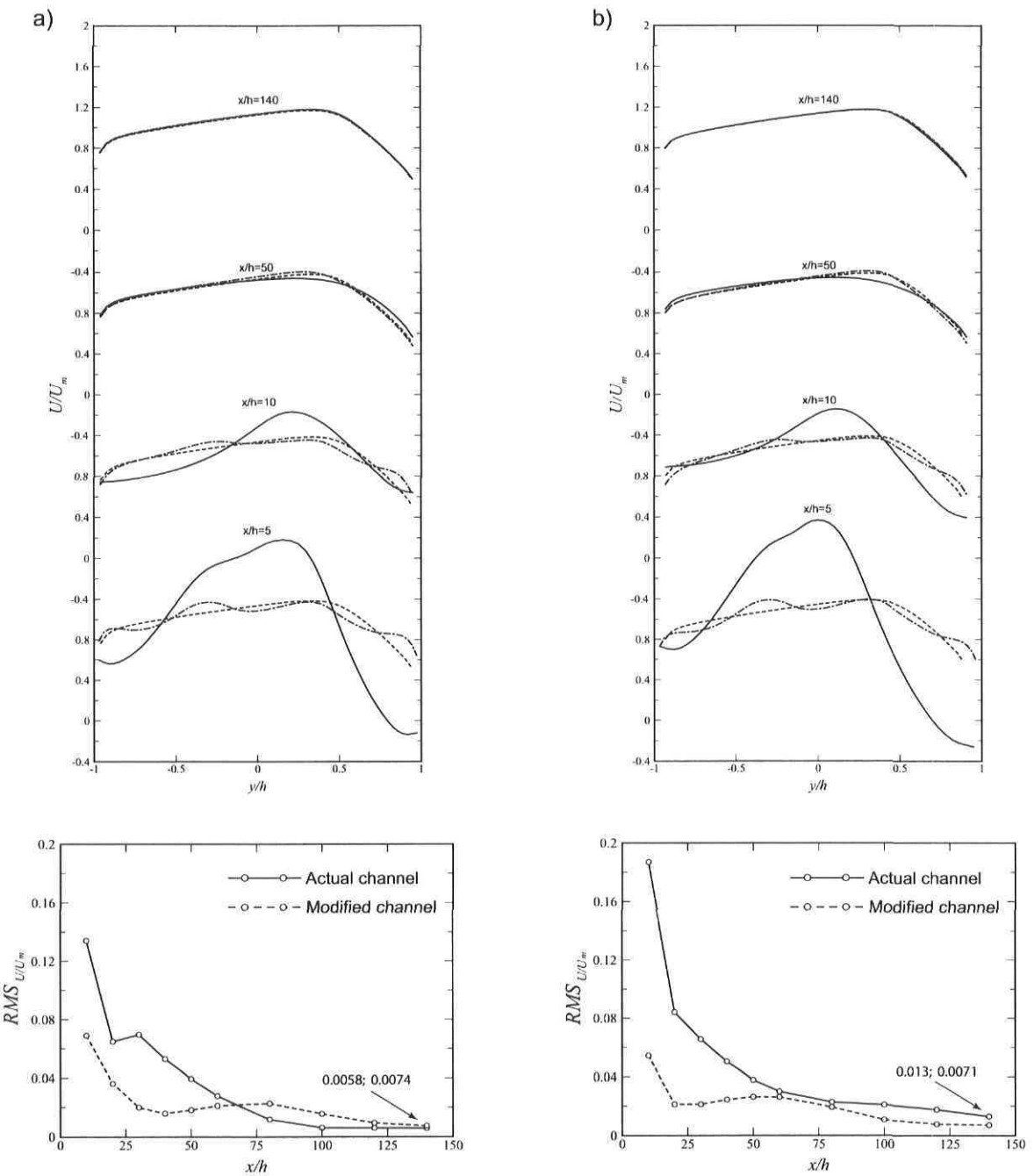

Figure 6.14: Streamwise velocity profiles and $\|\triangle_{FD}\|_{RMS}$ values at different stations along a rotating channel at $Ro = 0.22$. ——, Actual channel; — - —, modified channel; – –, fully developed solution. (a): $Re = 40000$; (b): $Re = 20000$.

At least qualitatively, the guides seem to aid the flow development in the rotating channel. However, the evolution of the RMS value indicates that the velocity profile slows down its approach toward the fully developed solution over a region of approximately $30h$. The increase in the RMS norm is caused by a small momentum surplus near $y/h = 0.25$ which is quite long to redistribute. A possible cause for such a slow recovery is the very low level of turbulence in the inlet region of the channel (see FIG. 6.15). Without the separation bubbles, a useful mechanism of turbulence production is suppressed.

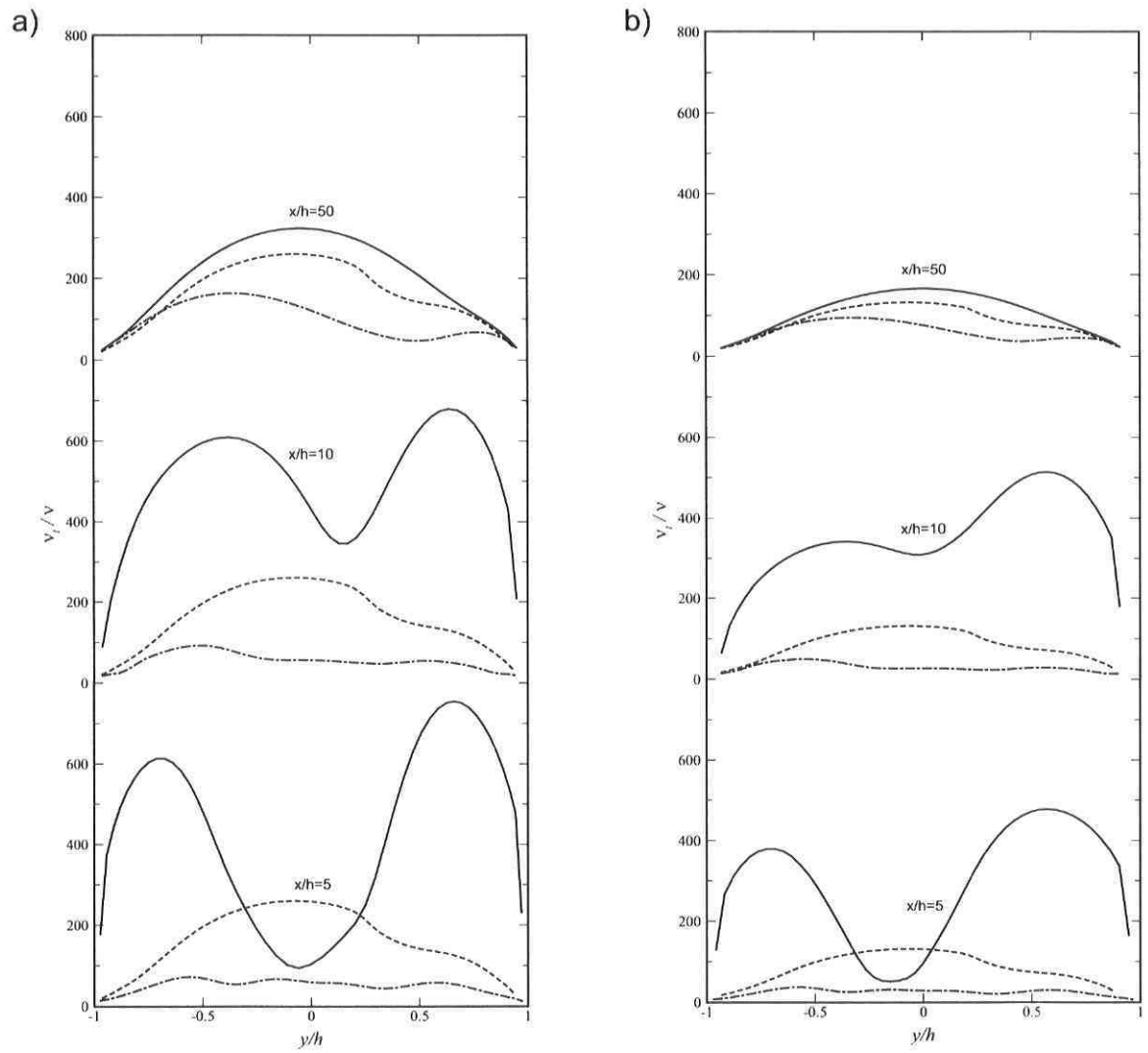

Figure 6.15: Turbulent viscosity ratio profiles at different stations along a rotating channel at $Ro = 0.22$. ——, Actual channel; — – —, modified channel; – –, fully developed solution. (a): $Re = 40000$; (b): $Re = 20000$.

In conclusion, the 2D case study has proven that the proposed design is able to completely remove all potential sources of pulsating flow, thus attaining one of the objec-

tives. Moreover, the guides have a simple shape and can be easily added to the present setup. The main objective is partly reached since the flow development is improved at $Re = 20000$ but no substantial progress is observed at the higher Reynolds number. At this stage, the proposed design is satisfactory, but it still has to be tested in a three-dimensional case. Such investigation is presented in the next chapter.

Chapter 7

Flow development in a rotating duct

The same tests that were performed in the previous chapter for a 2D channel, are now carried on a 3D geometry. The development length in a rotating and non-rotating duct at $Re = 40000$ is compared, and the flow development in the experimental setup is investigated.
Moreover, the end-wall effects on the flow development are examined by comparing the development length of the two-dimensional and three-dimensional channels.

7.1 Effect of rotation on flow development

The objective is to determine whether the development is faster in a rotating ($Ro = 0.22$) or a non-rotating duct of aspect ratio 11 at $Re = 40000$. Both calculations are performed using a very long domain ($L = 360h$), where a uniform velocity profile with no turbulence is set as inlet condition. To determine the degree of flow development, the streamwise velocity profiles at different stations along the channel are compared with the fully developed solution, and the RMS norm of the difference is computed at each position.

7.1.1 Mesh independence

Mesh independence tests are done using a $160h$ long duct of aspect ratio 11. Since 3D computations are very expensive it is not possible to simulate the entire duct in

a single calculation. Instead, the domain is divided in two sections of length $60h$ and $100h$ respectively. The first section has a uniform velocity profile with no turbulence as inlet condition and an *outflow* as exit condition. The $100h$ extension has the flow solution from the first section (at $x/h = 50$) as inlet condition and an *outflow* at the exit.

The coarse and fine domains have the same discretization in the x and y-direction, namely 295+250 and 51 cells. The mesh size in the streamwise direction varies between $0.1h$ and $0.4h$. In the z-direction, the coarse mesh has 45 elements and the cell size varies from $0.4h$ at the symmetry plane to $0.044h$ near the upper wall. The refined mesh has 80 elements and the grid size ranges from $0.2h$ to $0.044h$. A view of the two meshes is shown in FIG. 7.1.

Normally, the mesh independence study would be done on a rotating case where secondary flow phenomena are more restrictive on the mesh discretization. However, the calculations are performed at $Re = 40000$ and $Ro = 0$ for reasons that will be explained later in this chapter.

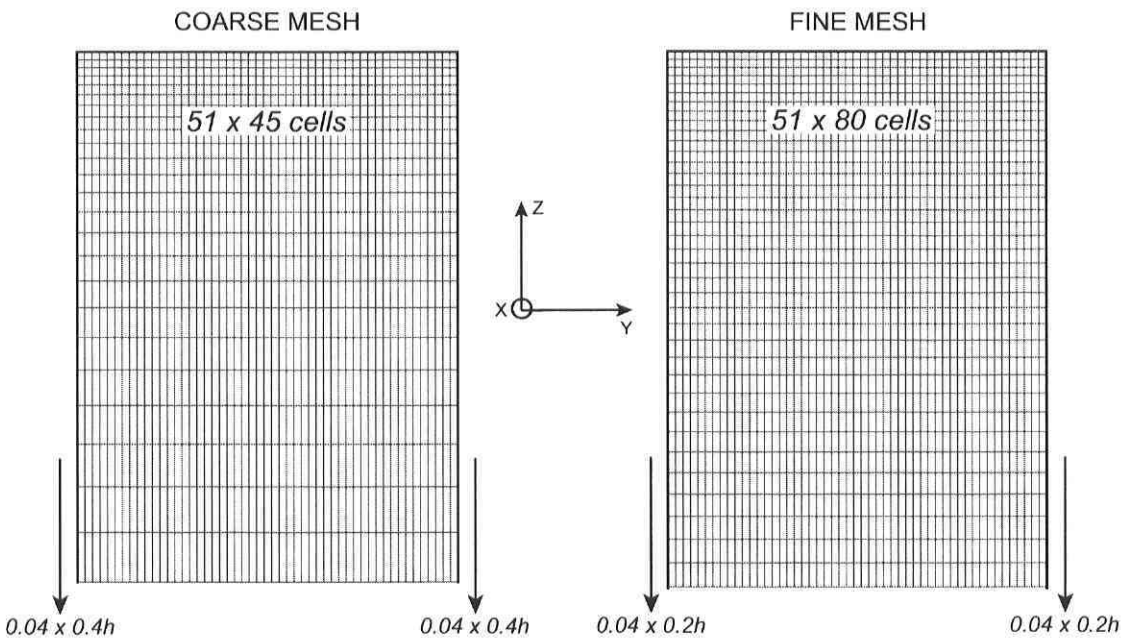

Figure 7.1: Coarse and refined meshes for studying the flow development in a non-rotating duct at $Re = 40000$.

The contours of FIG. 7.2 compare the flow development in the coarse and refined domain at a station situated at $140h$ from the duct inlet. The match between the two solutions is very good for all variables and the standard mesh is able to well capture all flow features. The RMS norm of the difference is also computed at four positions along the duct and the results are presented in TABLE 7.1.

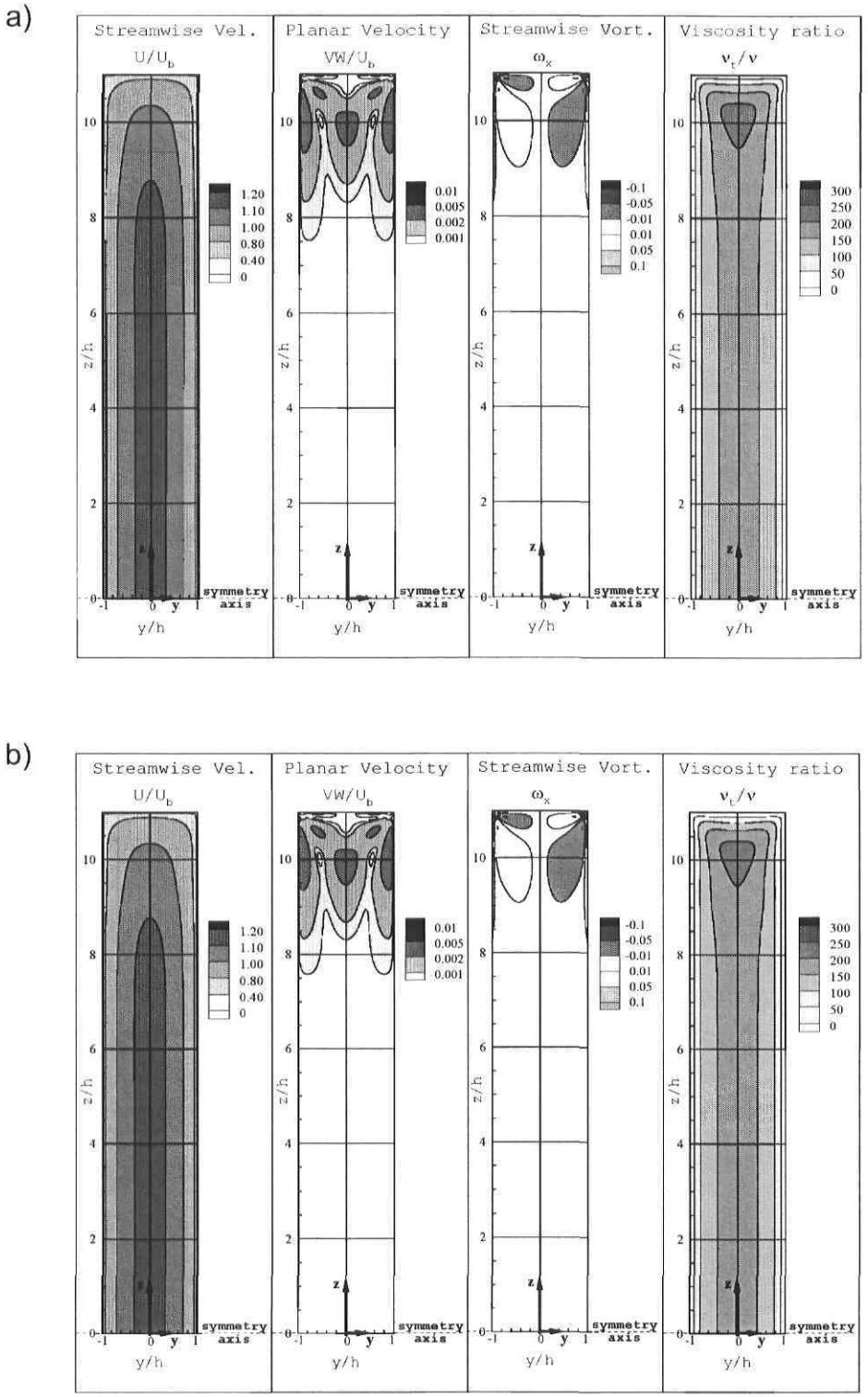

Figure 7.2: Flow development in a duct at $Re = 40000$ and $Ro = 0$. Plane contours at $x/h = 140$. (a): Standard mesh; (b): fine mesh. Flow direction toward the observer.

The relatively high RMS values of the planar velocity and streamwise vorticity, especially at the two most upstream stations, are due to the small magnitude of those two quantities. Consequently, a very small variation between the two solutions can result in a non negligible RMS norm. We recall again that our approach of calculating the norm excluded all comparisons points where the values were judged too small.

RMS norm	$x/h = 10$	$x/h = 50$	$x/h = 100$	$x/h = 140$
Streamwise velocity (U/U_b)	0.00027	0.00041	0.00057	0.00044
Planar velocity (VW/U_b)	0.0048	0.038	0.0154	0.0083
Streamwise vorticity (ω_x)	0.099	0.122	0.062	0.029
Viscosity ratio (ν_t/ν)	0.00274	0.0103	0.0016	0.0013

Table 7.1: $\|\triangle\|_{RMS}$ values at different stations along a duct at $Re = 40000$ and $Ro = 0$.

In conclusion, the coarse mesh is appropriate for studying the flow development in a non-rotating duct, and its validity for the rotating case will be discussed in the next section.

7.1.2 Flow development in a rotating and non-rotating duct

For both the rotating and non-rotating case, the flow development is investigated over a length of $320h$ ($50h+90h+90h+90h$). Since it would be too demanding to perform the study over a single domain, the latter is separated in four different sections. The first domain has a length of $60h$ and the remaining sections have each a length of $100h$. The approach is identical to the one described previously: a uniform velocity profile with no turbulence is set as inlet condition of the first domain whereas each $100h$ extension has the flow solution from the upstream section (at $10h$ from the exit boundary) as inlet condition. All domains have an *outflow* condition at the exit.
The rotating and non-rotating domains have the same discretization in the x and y-direction with 295+250+250+250 and 51 cells respectively. The non-rotating domain has 45 cells in the z-direction (FIG. 7.1a), whereas the rotating domain has 80 cells (FIG. 7.1b). This discretization yields a mesh with 4 260 000 and 2 400 000 cells for the rotating and non-rotating case respectively.
In the previous chapter, it was shown that in a 2D channel the flow development was faster in the non-rotating case since the boundary layer grows more rapidly at $Ro = 0$. However, the channel has now a finite aspect ratio and the boundary layer develops in both the transverse and spanwise directions. Therefore, its development will be affected by the end-wall generated secondary flow. This can be seen by plotting the evolution of U_m at the symmetry plane of the rotating and non-rotating ducts (FIG. 7.3). At

$Ro = 0$, the mean velocity at $z/h = 0$ increases as one travels downstream since the boundary layer near the upper wall grows in thickness, and causes a momentum deficit in that region. Therefore, to obey continuity, there must be a flow acceleration in the lower portion of the duct. At $x/h = 320$, the mean velocity is still evolving and has not reached the fully developed limit. Consequently, a very long distance is required before the presence of the upper wall is felt across the entire duct.

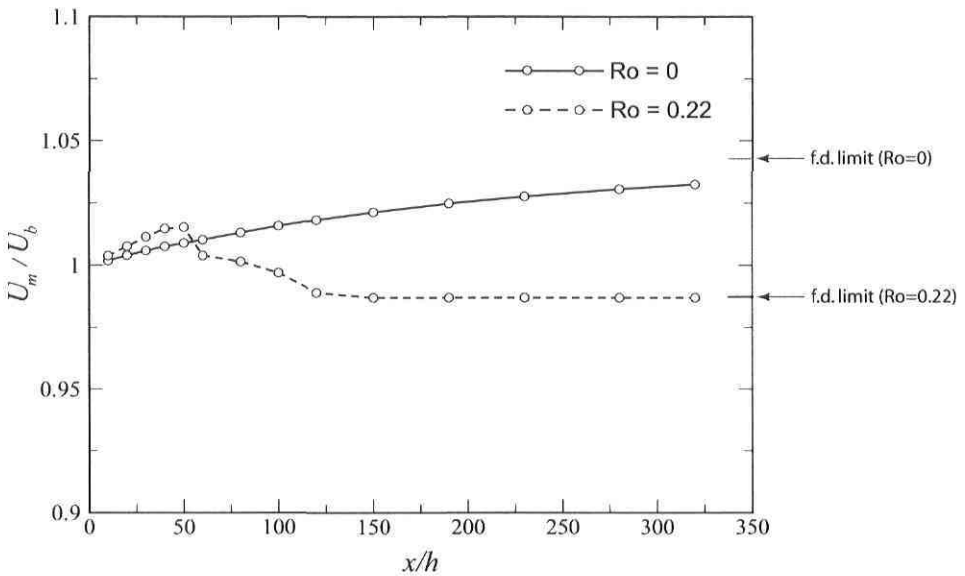

Figure 7.3: Evolution of the mean velocity at the symmetry plane of a duct at $Re = 40000$.

In the rotating case, the evolution of the mean velocity is not monotonous since there is a strong interaction between turbulent transport and rotation effects. Up to a distance of $50h$ from the inlet, transport processes are dominant and they cause a flow acceleration at the symmetry plane of the duct. Further downstream, the inverse phenomenon occurs and the flow starts to decelerate, resulting in a momentum deficit at this location. The latter behaviour is due to the end-wall generated secondary flow, which is now an order of magnitude stronger than it was in the non-rotating case.

As discussed in chapter 5, the cross stream current confines the spanwise velocity gradient to a thin region near the upper wall. By doing so, it regulates the mass flow distribution across the duct and it ensures a constant mean velocity at the symmetry plane. FIG. 7.3 indicates indeed that the mean velocity at the symmetry plane of the rotating duct stops varying after a distance of $150h$ from the duct inlet. However, the flow is not necessarily fully developed at this location.

To assess the state of flow development in the rotating and non-rotating ducts, the evolution of the streamwise velocity profile at $z/h = 0$ is presented in FIG. 7.4. The plots indicate that, in the non-rotating duct, the velocity profile at the most downstream station is close to being fully developed. The small streamwise evolution displayed by the RMS norm is essentially due to the thickening of the shear region near the upper

wall, which alters the mean velocity distribution across the duct. After a distance of approximatively $200h$, the velocity profile has already reached its fully developed shape (see FIG. 7.5a), but it does not have the correct mass flow rate. Consequently, end wall effects are responsible for the notable increase in the development length. One should remember that the non-rotating channel was fully developed (based on a RMS norm of 0.5%) at $x/h = 180h$, whereas the duct flow is still evolving at $x/h = 320h$.

In the rotating case, the RMS value jumps up in the vicinity of $x/h = 110$. This behaviour is caused by the appearance of counter-rotating longitudinal cells along the pressure wall of the duct. As illustrated in FIG. 7.6b, up to a distance of $100h$ no roll cells are present, and the flow evolves toward the fully developed limit (see FIG. 5.4b). However, a short distance further downstream, counter-rotating cells start to appear in the lower portion of the duct and, at $x/h = 150$, three vortex pairs are clearly visible. Very close to the symmetry plane, a vortex of positive signed vorticity is present, and induces a positive velocity in the y-direction. On average, the induced velocity at $z/h = 0$ is $V/U_b = 0.03$, and its peak value is situated at $y/h = -0.5$. At the last measurement station, the number of cell pairs has increased, and they spread over the entire height of the duct. Moreover, there is a strong interaction between the vortices situated in the upper portion of the duct and the Ekman generated secondary flow. The impact of the cross stream current at the symmetry plane is weakened and the value of the transverse velocity at $z/h = 0$ is dictated by the Taylor-Görtler vortex, except close to the suction wall.

The roll cell has a notable impact on the streamwise velocity profile at the symmetry plane since it generates a momentum transport from the pressure side toward the suction side of the duct (see FIG. 7.4b). The reader will remember that this effect is exactly the opposite of the one produced by the secondary flow associated with the Ekman vorticity.

A more detailed description of the impact of the roll cell instability on the flow development, as well as the reason of why no roll cells appeared in the fully developed solution (presented in chapter 5) will be given in section 7.1.4.

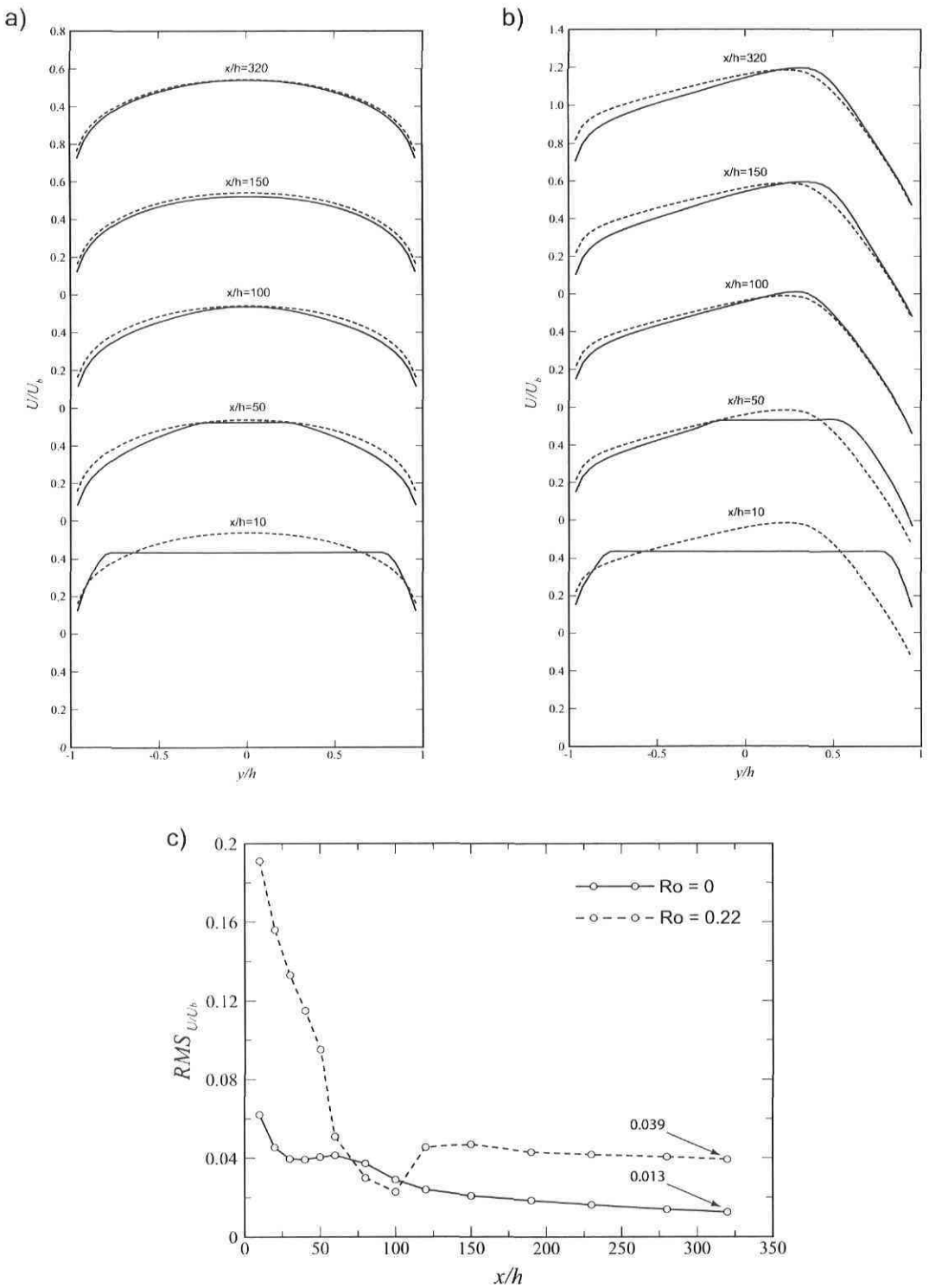

Figure 7.4: Streamwise velocity profiles (normalized with the bulk velocity) at symmetry plane of a duct at $Re = 40000$. ——, Solution at measurement station; – –, fully developed solution. (a): $Ro = 0$; (b): $Ro = 0.22$. (c): $\|\triangle_{FD}\|_{RMS}$ norm of the difference.

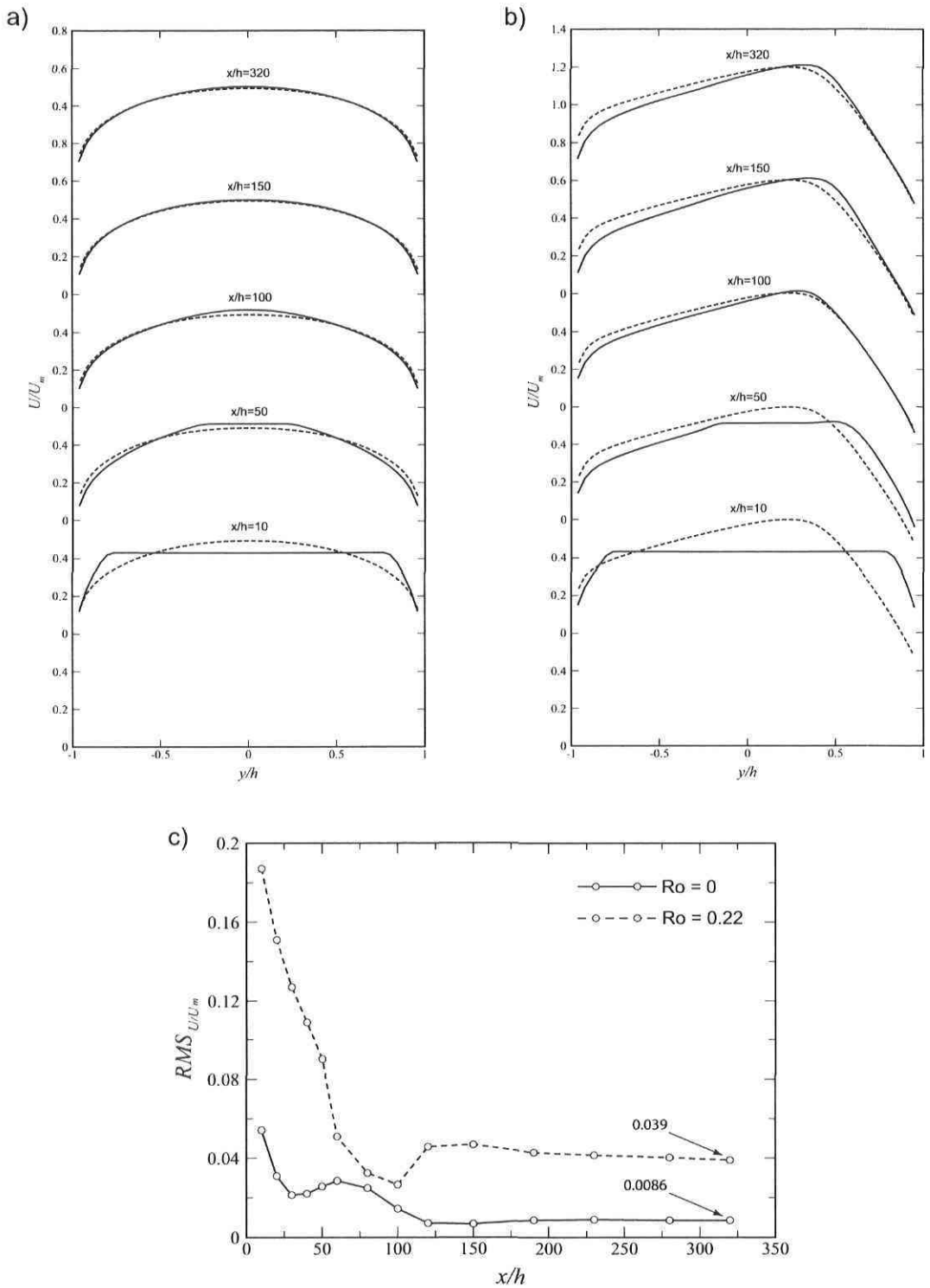

Figure 7.5: Streamwise velocity profiles (normalized with the mean velocity) at symmetry plane of a duct at $Re = 40000$. ——, Solution at measurement station; – –, fully developed solution. (a): $Ro = 0$; (b): $Ro = 0.22$. (c): $\|\triangle_{FD}\|_{RMS}$ norm of the difference.

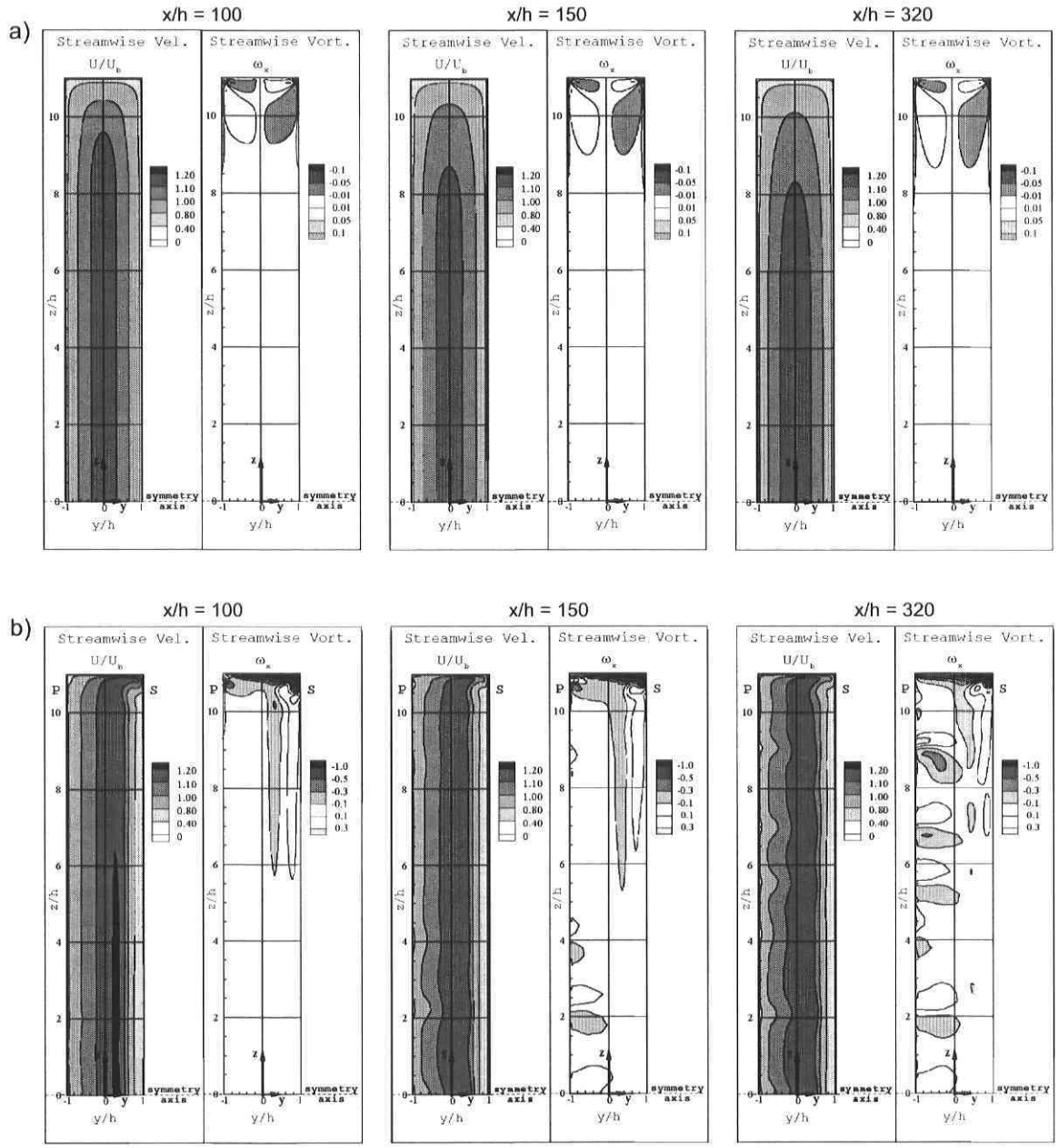

Figure 7.6: Plane contours at different stations along a duct at $Re = 40000$. (a): $Ro = 0$; (b): $Ro = 0.22$. Flow direction toward the observer.

In summary, the 3D flow development in a finite aspect ratio rotating duct involves three simultaneous phenomena, as illustrated in FIG. 7.7. The first process is the growth of the boundary layers along the sides of the duct (i.e., 2D flow development), the second one is the development of the end-wall generated secondary flow and the last one is the development of the longitudinal roll cells along the pressure wall of the duct. Thus, in order to reach a fully developed state in a rotating duct, all three processes must become fully developed.

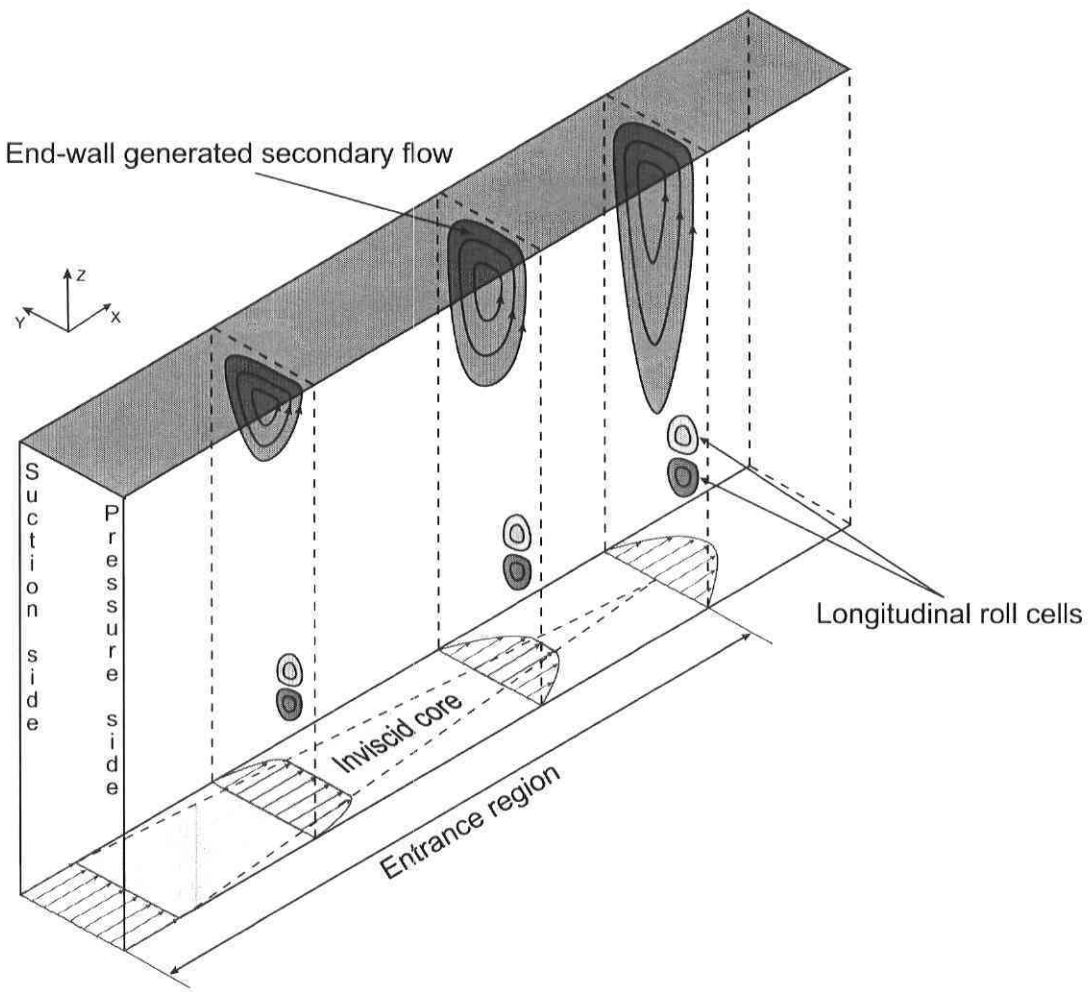

Figure 7.7: Flow development processes in a finite aspect ratio rotating duct.

7.1.3 Effect of mesh discretization on roll cell instability

In the previous section, longitudinal roll cells have been observed along the pressure wall of the rotating duct. With the mesh of FIG. 7.1, a counter-rotating vortex pair in the lower section of the duct ($z/h < 6$) is discretized with 10 spanwise elements, and it is suspected that the grid is not fine enough to capture well the Taylor-Görtler vortices. For this reason, the flow development calculations are now performed on a finer mesh that has 135 elements in the z-direction (the cell size in the lower section is $0.1h$).
The flow solution obtained with the refined mesh is shown in FIG. 7.9. In comparison to the results of FIG. 7.6b, the roll cell instability starts to appear further upstream, and at $x/h = 50$ two vortex pairs are present along the pressure wall (with the coarse grid the first vortices appeared at $x/h = 110$). Moreover, the number of vortex pairs in the duct has increased and their intensity has grown in magnitude. Finally, it is relevant to note than the sign of the streamwise vortex closest to the symmetry plane was positive in the coarse domain, whereas it is now negative.
The latter remark is particularly important since the vortex sign directly affects the direction of the cross stream current at the symmetry plane. As illustrated in FIG. 7.8, the transverse velocity at $z/h = 0$ is positive in the coarse domain and negative in the refined one. The peak of V/U_b is lower in the refined domain because the vortex is situated further from the symmetry plane. Finally, with the coarse mesh, the V/U_b

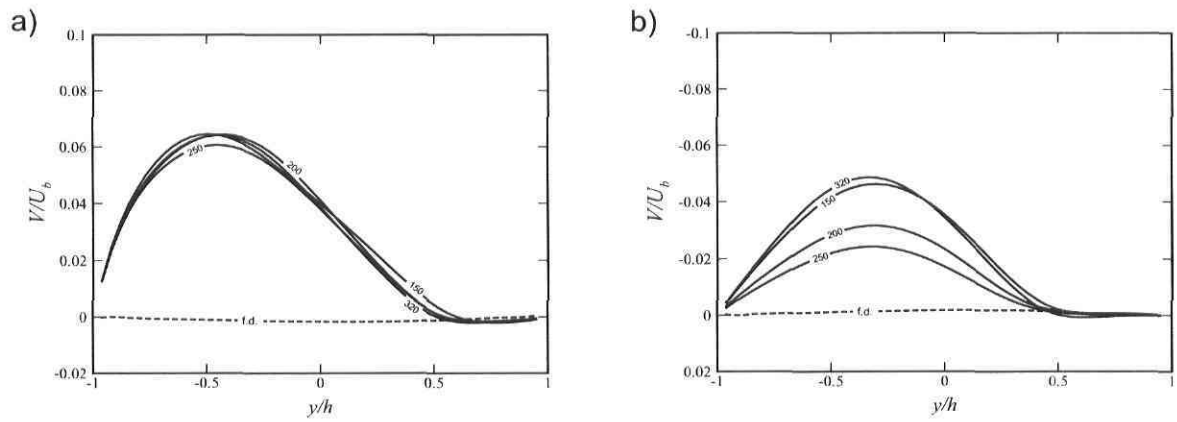

Figure 7.8: Transverse velocity profiles at symmetry plane of a duct at $Re = 40000$ and $Ro = 0.22$. ——, Solution at measurement station; – –, fully developed solution. (a): Coarse mesh; (b): fine mesh.

profile remains essentially constant at all four streamwise stations, whereas its amplitude oscillates in the refined domain since the vortex has moved either toward or away from the symmetry plane.

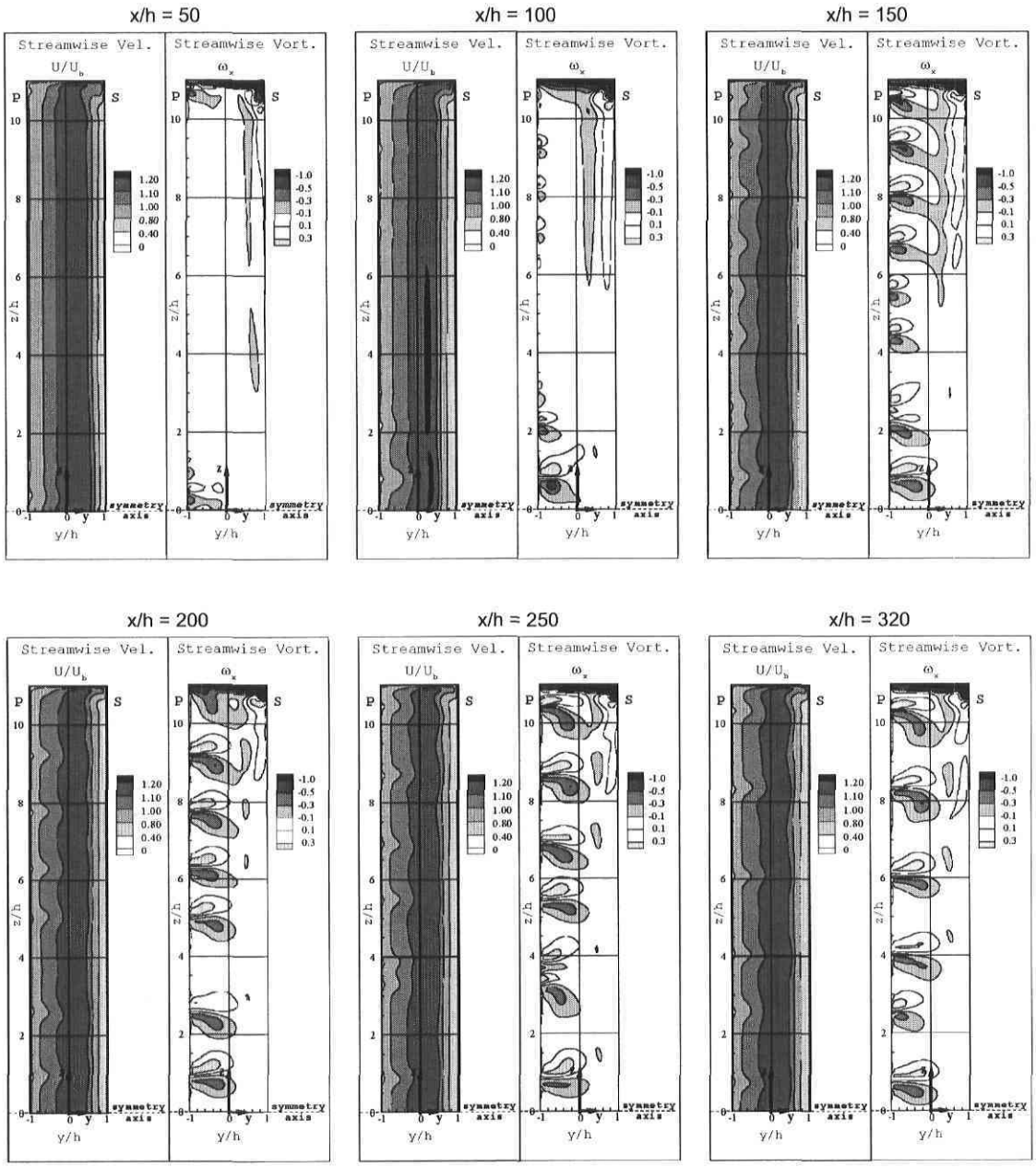

Figure 7.9: Plane contours at different stations along a duct at $Re = 40000$ and $Ro = 0.22$. Flow direction toward the observer.

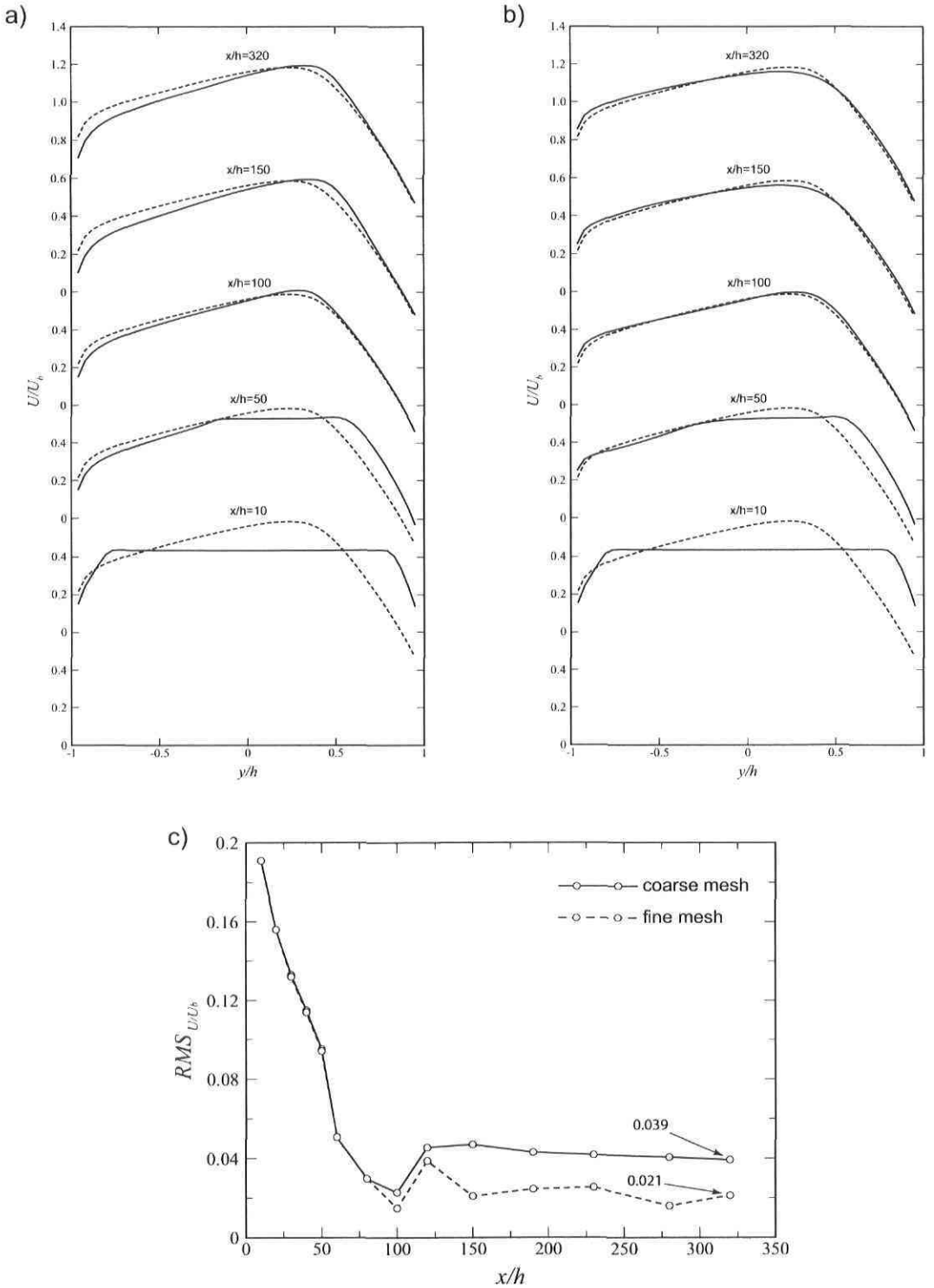

Figure 7.10: Streamwise velocity profiles at symmetry plane of a duct at $Re = 40000$ and $Ro = 0.22$. ——, Solution at measurement station; – –, fully developed solution. (a): Coarse mesh; (b): fine mesh. (c): $\|\triangle_{FD}\|_{RMS}$ norm of the difference.

The variation of the vortex configuration between the coarse and refined domains has a direct impact on the streamwise velocity. FIG. 7.10 compares the evolution of U in the two domains. Up to a distance of $80h$, the velocity profiles evolve in a similar way since the "two-dimensional" development is dominant. However, starting from $x/h = 120$, the instability becomes a key factor in the flow development and, via its momentum transport, modifies the streamwise velocity profile. Depending on the vortex sign, momentum is either transferred from the pressure wall toward the center of the duct or vice versa. In the former case, the velocity profile will show a momentum deficit in the destabilized portion of the duct (FIG. 7.10a).
Although, the solution is still affected by mesh discretization, the overall dynamics of the roll cells is not. Under the action of the end-wall generated secondary flow, the vortex pairs move toward the upper wall, as one goes downstream. When the Taylor-Görtler vortices near the solid boundary, they are quickly dissipated and almost simultaneously new vortex pairs are generated in the lower portion of the duct, thus repeating the cycle.
In conclusion, a change in the vortex pair configuration has been observed with a mesh refinement in the spanwise direction. With a finer grid, the vortex intensity as well as their number have increased. Even though mesh independence has not been formally proven, the instability mechanism is consistent since its presence has been observed with both mesh discretizations, and the dynamics of the vortex pairs is very similar in the two cases. A further mesh refinement would be desirable, but a limit is imposed by the available computational resources.

7.1.4 Effect of roll cell instability on flow development

The flow development computations in a rotating duct have shown the appearance of the roll cell instability mechanism. In this section, the impact of such instability on the flow development is discussed, and the possibility of actually reaching a fully developed steady flow in a rotating duct of finite aspect ratio is investigated.
As shown by the contours of streamwise vorticity and the secondary flow streamlines of FIG. 7.11, the roll cells are present only near the pressure wall of the duct, and their width varies between h and $1.5h$. Therefore, they do not occupy the entire section of the duct, and the end-wall generated secondary flow can still penetrate far into the duct (down to $z/h = 0$) along the suction side wall. This aspect is crucial in the flow dynamics since the returning cross-stream current is able to convect the vortex pairs toward the upper wall of the duct. Consequently, the roll cells move upward as one goes downstream, and they are quickly dissipated when they reach the solid boundary. The spanwise drift is not constant along the duct since the intensity of the end-wall generated secondary flow in greater in the upper region of the domain. Near

the symmetry plane, where the secondary flow is very weak, the vortex pair does not drift, and slightly oscillates around $z/h = 1$. However, in the central portion of the duct the drift velocity becomes close to $W/U_b = 0.01$ and it can reach 2.5% of U_b in the upper region. In consequence, the distance between two counter-rotating pairs is

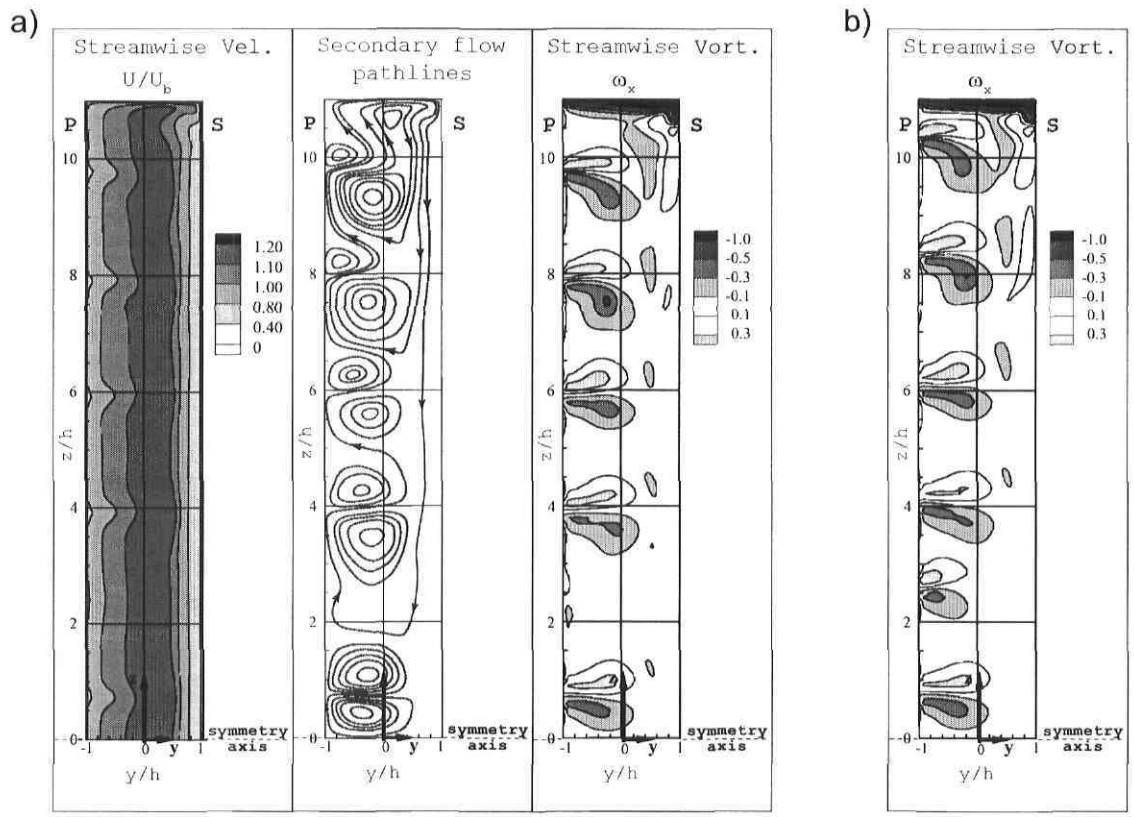

Figure 7.11: Rotating duct at $Re = 40000$ and $Ro = 0.22$. a): Solution in a y-z plane at $x/h = 300$; (b): solution at $x/h = 320$. Flow direction toward the observer.

not quite constant as one goes downstream, except in the lower portion of the domain where it is approximatively $2h$. This wavelength is analogous to the one obtained by Kristoffersen & Andersson (1993) in a DNS calculation of a rotating channel flow at $Re \approx 3000$ and $Ro = 0.2$. The experimental measurements of Johnston *et al.* (1972) also suggest that the roll cells have a wavelength of approximatively $2h$ at $Re \approx 3000$ and $Ro \approx 0.22$.

Because of the presence of the end-wall generated secondary flow, the roll cells are not horizontal (aligned in the x-direction) but instead they are slightly tilted upward. The angle α is proportional to the ratio W/U, and is visible in the plots of FIG. 7.12. For the reasons explained before, the drift angle of the vortex pair increases as the latter moves toward the upper wall of the duct. More importantly, the slant of the counter-rotating vortices necessary implies that no permanent fully developed solution will ever be reached. Thus, a steady fully developed solution for a rotating duct of finite aspect

ratio is not found at this flow regime since tilted roll cells are present in the solution which implies $\partial/\partial x \neq 0$.

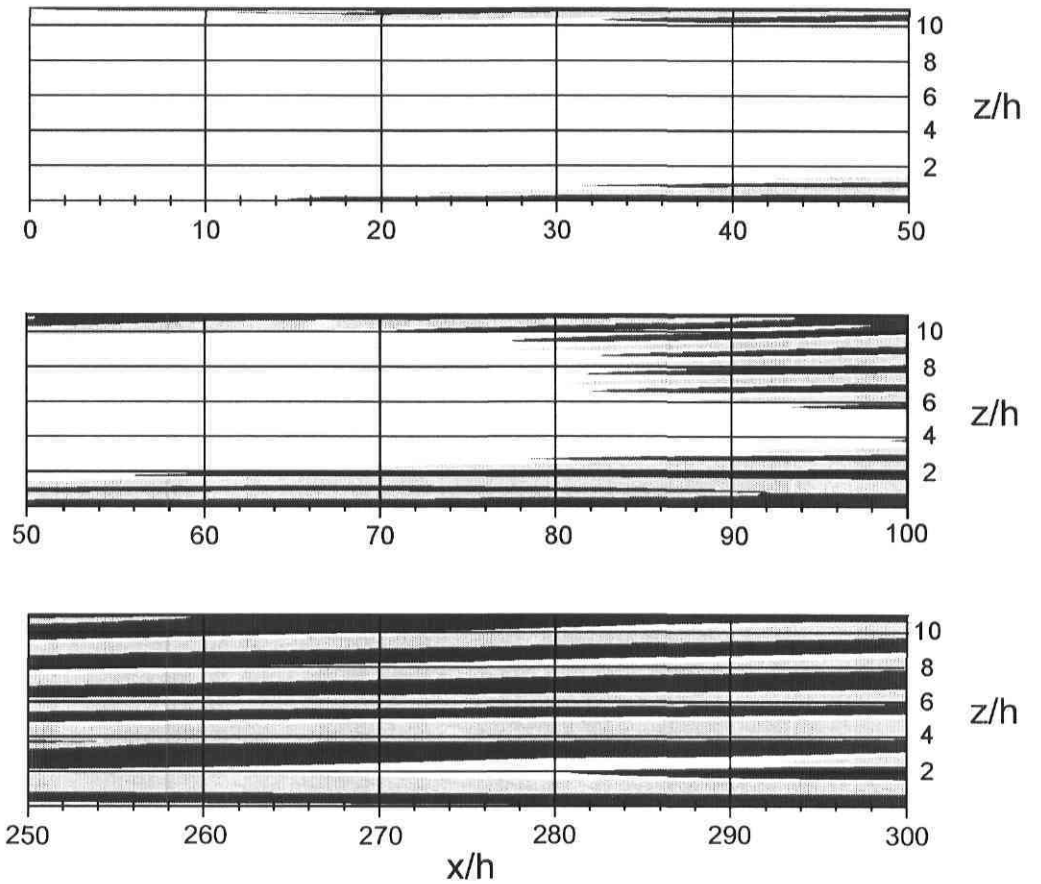

Figure 7.12: Rotating duct at $Re = 40000$ and $Ro = 0.22$. Contours of streamwise vorticity ω_x in a xz plane at 0.25h from the pressure wall. Light gray contours: $\omega_x > 0.01$; dark gray: $\omega_x < -0.01$. Flow direction toward the right.

The latter statement also explains why no trace of counter-rotating vortex pairs was observed in the fully developed steady state solution of chapter 5. The reader will remember that those calculations were carried out on a domain having periodic boundaries on a very short length in the streamwise direction to force a $\partial/\partial x = 0$. In order to satisfy such condition, no Taylor-Görtler cell (which must be tilted as we have just seen) can actually appear in the numerical solution.
In conclusion, a fully developed solution for a rotating duct of finite AR may exist only if unsteadiness is allowed in the simulation. This case will be treated in chapter 8.

7.2 Validation of the design hypothesis

In the previous chapter, the flow development in the experimental and in the straight channels were compared, and it was found that the pre-development did not significantly reduce the development length. Now, the same comparison is performed except that the two channels have a finite aspect ratio ($AR = 11$).
The streamwise and transverse dimensions of the two ducts remain unchanged compared to the 2D case, i.e., a length of $140h$ and a width of $2h$. For computational reasons, each domain is split in two sections of length 60 and $100h$ and the flow solution from the shorter section is set as inlet condition for the $100h$ extension. An isometric view of the actual duct is presented in FIG. 7.13.

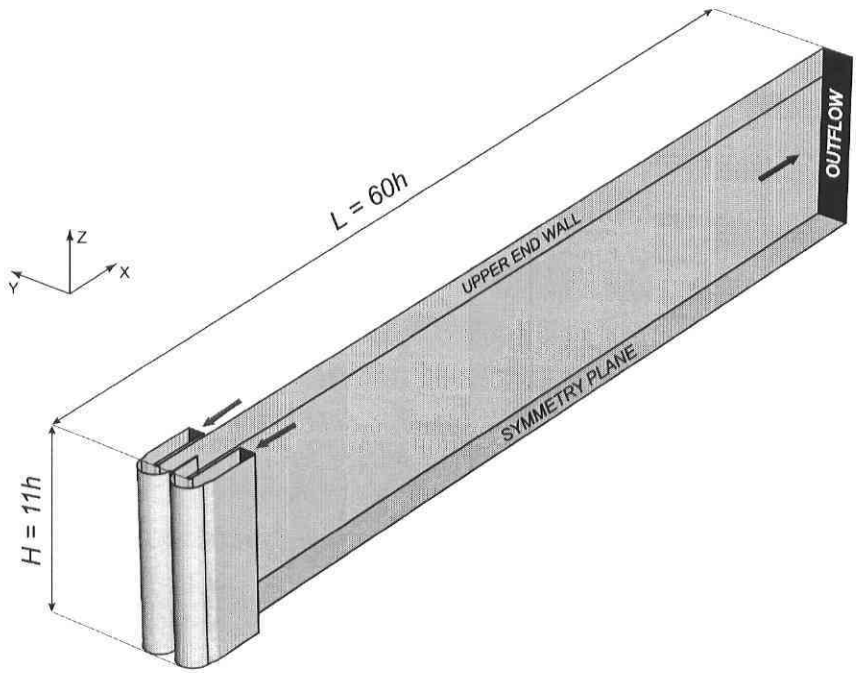

Figure 7.13: Isometric view of the inlet section in the actual duct.

The actual duct has fully developed conditions at the entrance plane of the two lateral channels ($4h$ upstream of the 180° turn), whereas the straight duct has a uniform velocity inlet with no turbulence. As it was mentioned in section 6.2, the "real" inlet conditions in the experimental setup are not known. However, the flow is probably well developed at this location and the fully developed profile is a valid approximation. The outlet condition is an *outflow* for both the actual and the straight ducts.
The mesh discretization in the x and y-direction are identical to the 2D case, and the z-direction is discretized with 80 elements (as in FIG. 7.1). Although it was previously demonstrated that a mesh with 135 elements in the spanwise direction would better capture the longitudinal vortices, it cannot be used in the actual domain for computa-

tional reasons. Overall, the actual and the straight domain have 2 200 000 and 3 000 000 cells respectively.

As it was explained in section 7.1.4, no steady fully developed solution can be reached in a rotating duct because of the slant of the Taylor-Görtler cells. Thus, the following discussion will attempt to evaluate qualitatively the degree of flow development along the duct, and further it will focus on the effect of the 180° turn on the formation of the Ekman layer and on the appearance of the roll cell instability.

As illustrated in FIG. 7.14a, two separation bubbles are present in the entrance portion of the actual duct. At the symmetry plane, the separation region extends over a length of $5.2h$ and $2.0h$ on the suction and pressure side respectively. Those dimensions are very close to the ones that were obtained in the 2D case, and consequently the shape of the separation bubbles at $z/h = 0$ is not affected by the presence of an end-wall. On

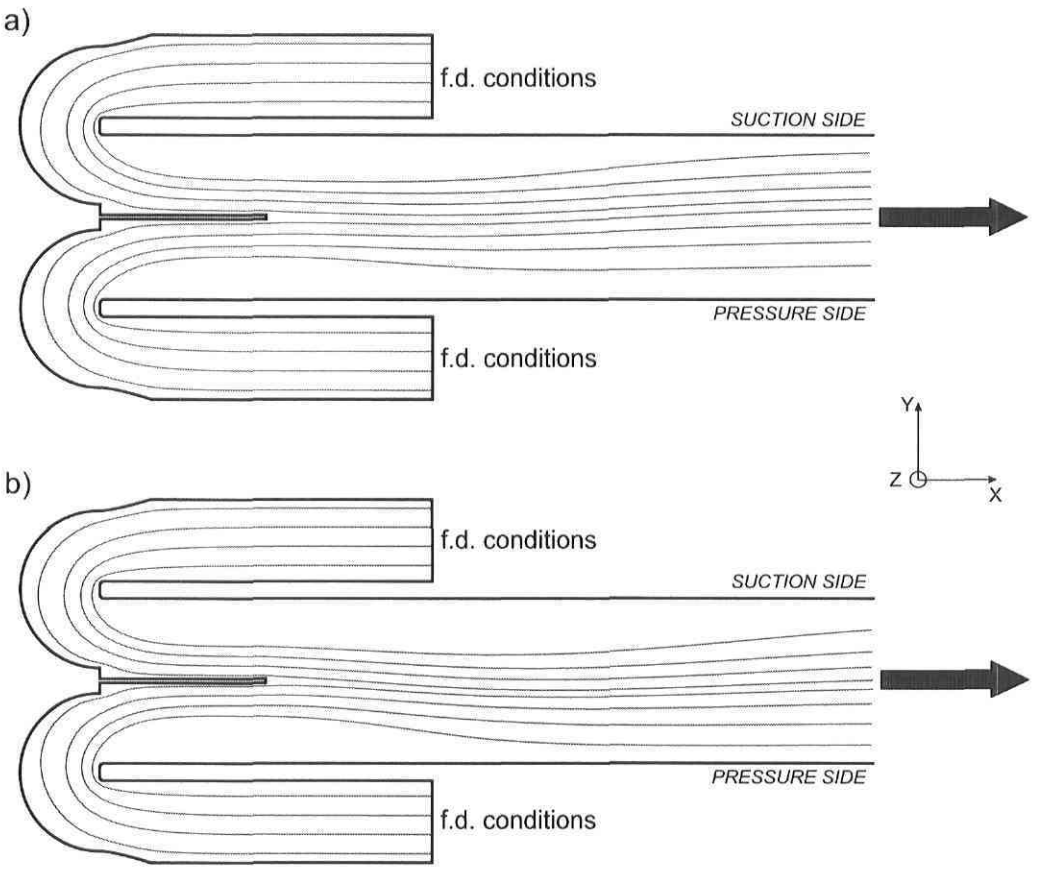

Figure 7.14: Streamlines at the symmetry plane of the actual rotating duct. (a): $Re = 40000$; (b): $Re = 20000$.

the suction side of the duct, the separation zone is essentially constant in the spanwise direction up to a distance of $2h$ from the upper boundary, whereas on the pressure side the uniformity is less marked.

At $Re = 20000$ (FIG. 7.14b), the separation bubble is longer, i.e., $7h$ and $2.6h$ on

the stabilized and destabilized side respectively. Once again, those values are in good agreement with the 2D case, and the spanwise uniformity of the recirculating flow is more pronounced on the suction than on the pressure side.
A more detailed view of the flow development in the actual and straight ducts at $Re = 40000$ is shown in FIG. 7.16 and 7.17. In the entrance region of the actual duct, there is a strong interaction between the centrifugal vortices due to the 180° turns, and the Ekman layer (a view of the centrifugal vortices in the entrance region of the actual duct in the non-rotating case is shown in FIG. 7.15). The two phenomena are of

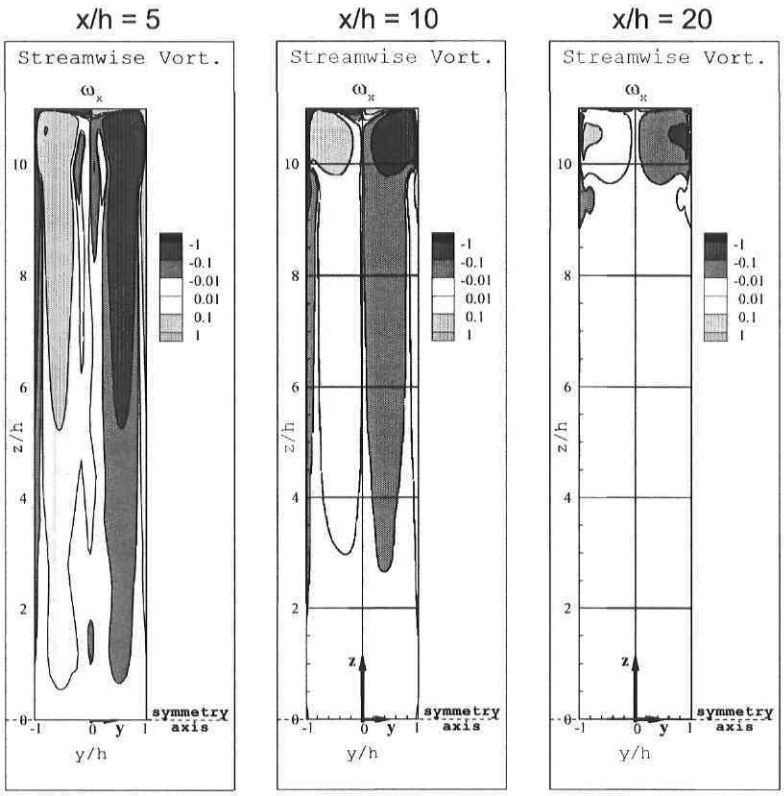

Figure 7.15: Streamwise vorticity contours at different stations along the actual duct at $Re = 40000$ and $Ro = 0$. Flow direction toward the observer.

similar intensity, but in the pressure side of the duct they have the tendency to cancel each others, whereas in the suction side they mutually reinforce. A distance of approximatively $20h$ is required to completely dissipate the centrifugal vortices and to start developing the Ekman layer. Thus, compared to the straight duct, the development of the Ekman layer is hindered, and it takes a longer distance before the presence of the end-wall generated secondary flow is felt across the entire duct.
The latter phenomenon is particularly important since it directly affects the appearance of the first counter-rotating vortex pair. As shown in FIG. 7.16, two pairs have appeared near the pressure side of the duct at $x/h = 5$. Further downstream, the roll cells shift toward the center of the duct, and they occupy the entire width since no

descending secondary flow is present along the suction side yet. At a distance of about $25h$ from the main channel inlet, longitudinal vortices of smaller size are equally visible along the stabilized side. These roll cells are juxtaposed to the ones present along the pressure side, and are of opposite sign. Further downstream ($x/h = 35$), the vortical structures near the upper wall begin to weaken since the Ekman generated secondary flow now occupies the upper section of the duct and, at $x/h = 50$, all roll cells have practically disappeared. A short distance further downstream, the counter-rotating vortices develop once again near the pressure wall but this time their width is smaller (about $1.5h$) since the end-wall generated secondary flow is present along the entire suction wall. Moreover, the Taylor-Görtler vortices are now convected toward the upper boundary, where they dissipate. At $x/h = 140$, six counter-rotating vortex pairs are found across the entire height of the duct.

At $Re = 20000$ (FIG. 7.18), the roll cells behaviour is very similar to the one previously described although the instability mechanism is slightly hindered.

In summary, in the actual duct the roll cell instability appears further upstream than in the straight duct for two main reasons. First, the "pre-development" in the lateral channels allows to already have a sheared velocity profile at the inlet of the main channel, thus satisfying the minimal conditions for the appearance of the instability. Secondly, the centrifugal vortices weaken the Ekman layer, and consequently reduce the intensity of the end-wall generated secondary flow.

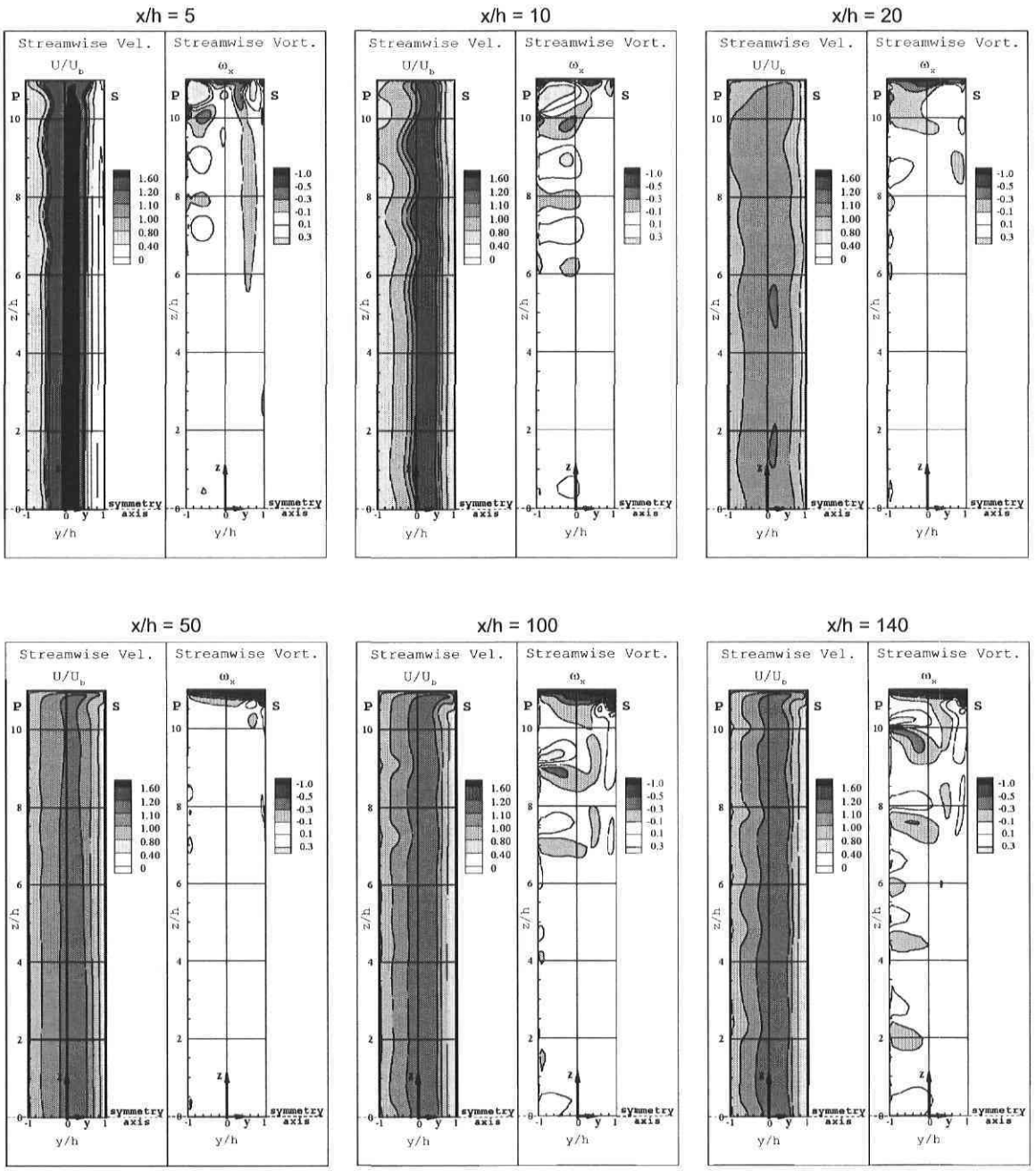

Figure 7.16: Plane contours at different stations along the actual duct at $Re = 40000$ and $Ro = 0.22$. Flow direction toward the observer.

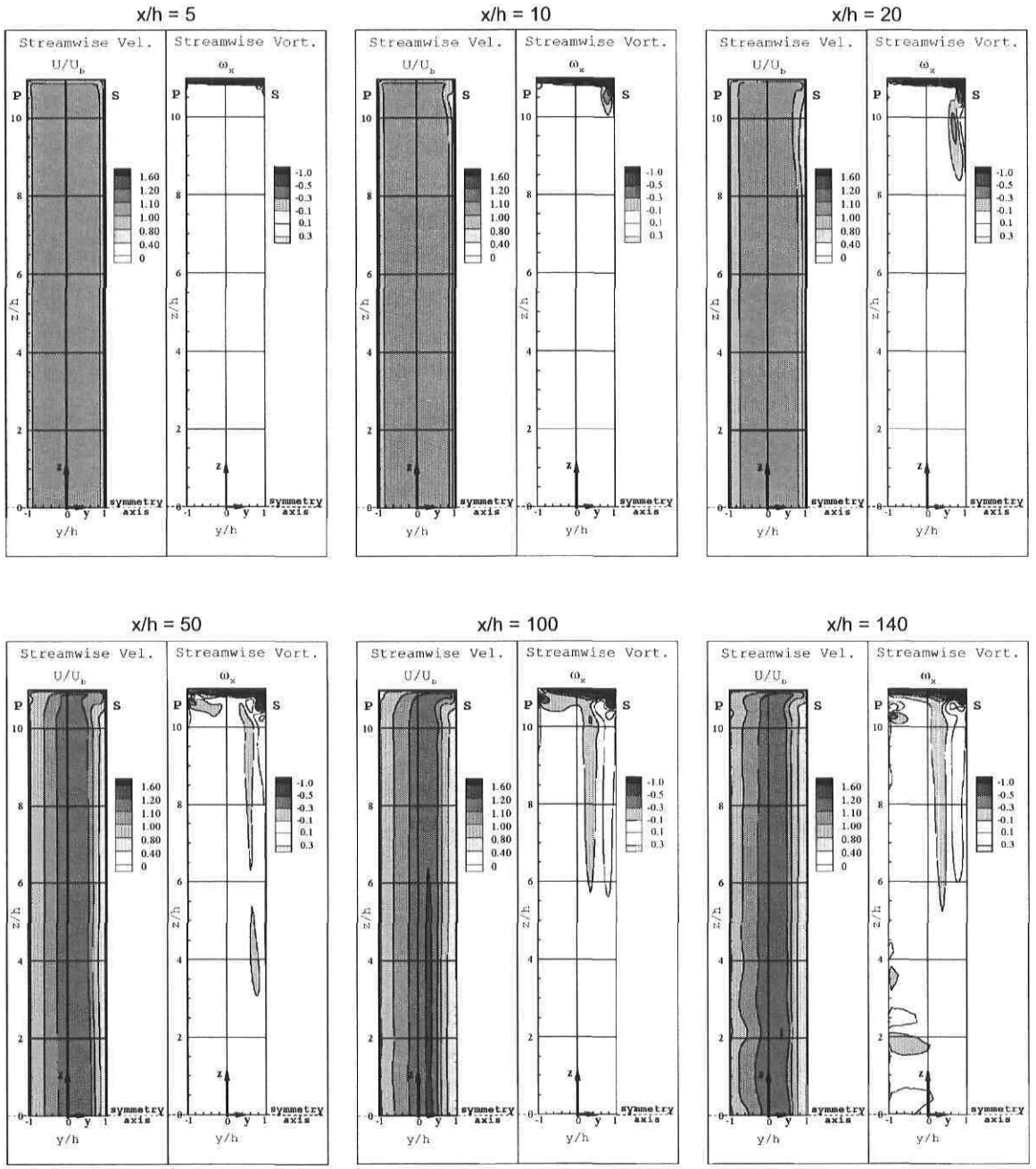

Figure 7.17: Plane contours at different stations along the straight duct at $Re = 40000$ and $Ro = 0.22$. Flow direction toward the observer.

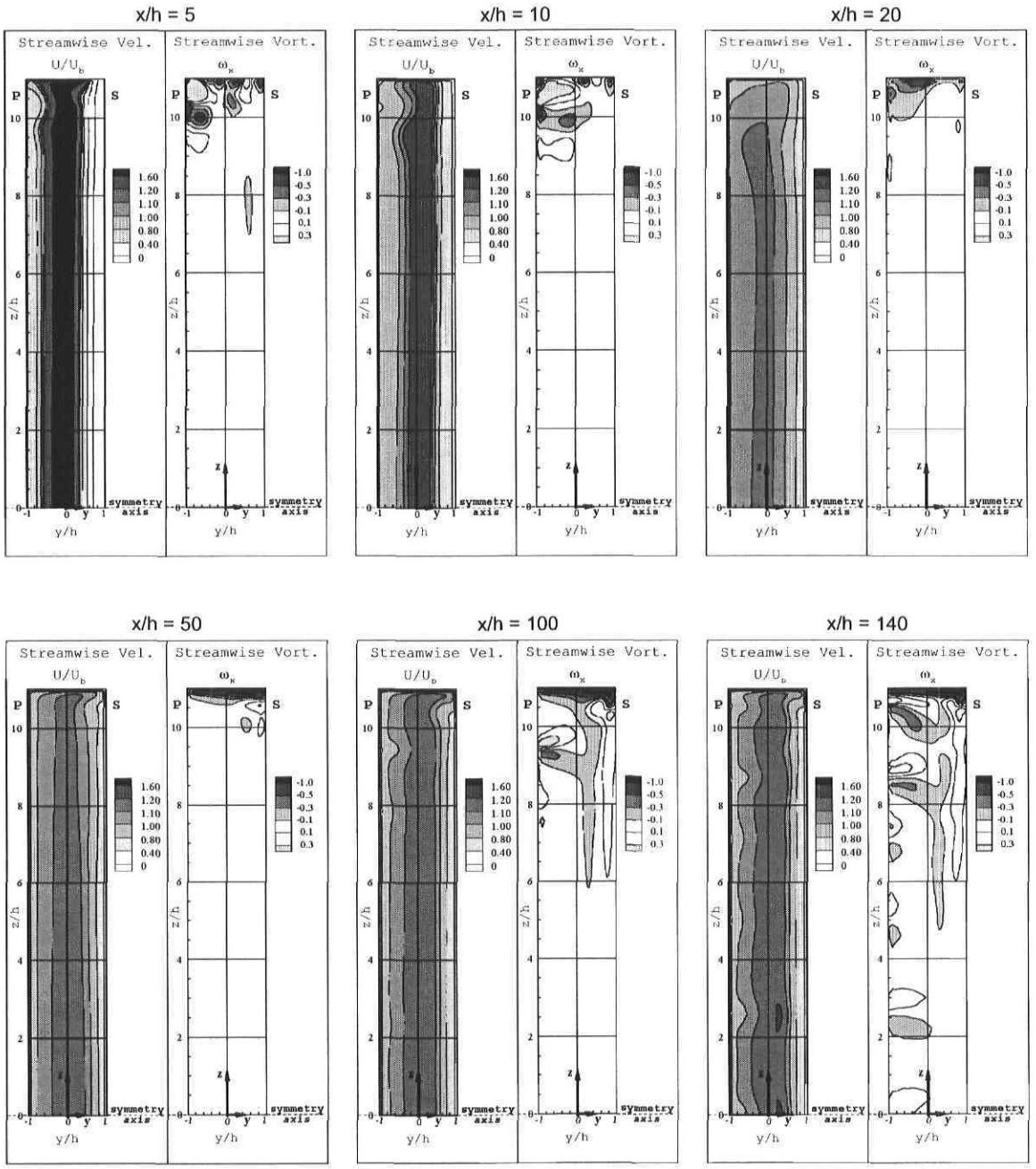

Figure 7.18: Plane contours at different stations along the actual duct at $Re = 20000$ and $Ro = 0.22$. Flow direction toward the observer.

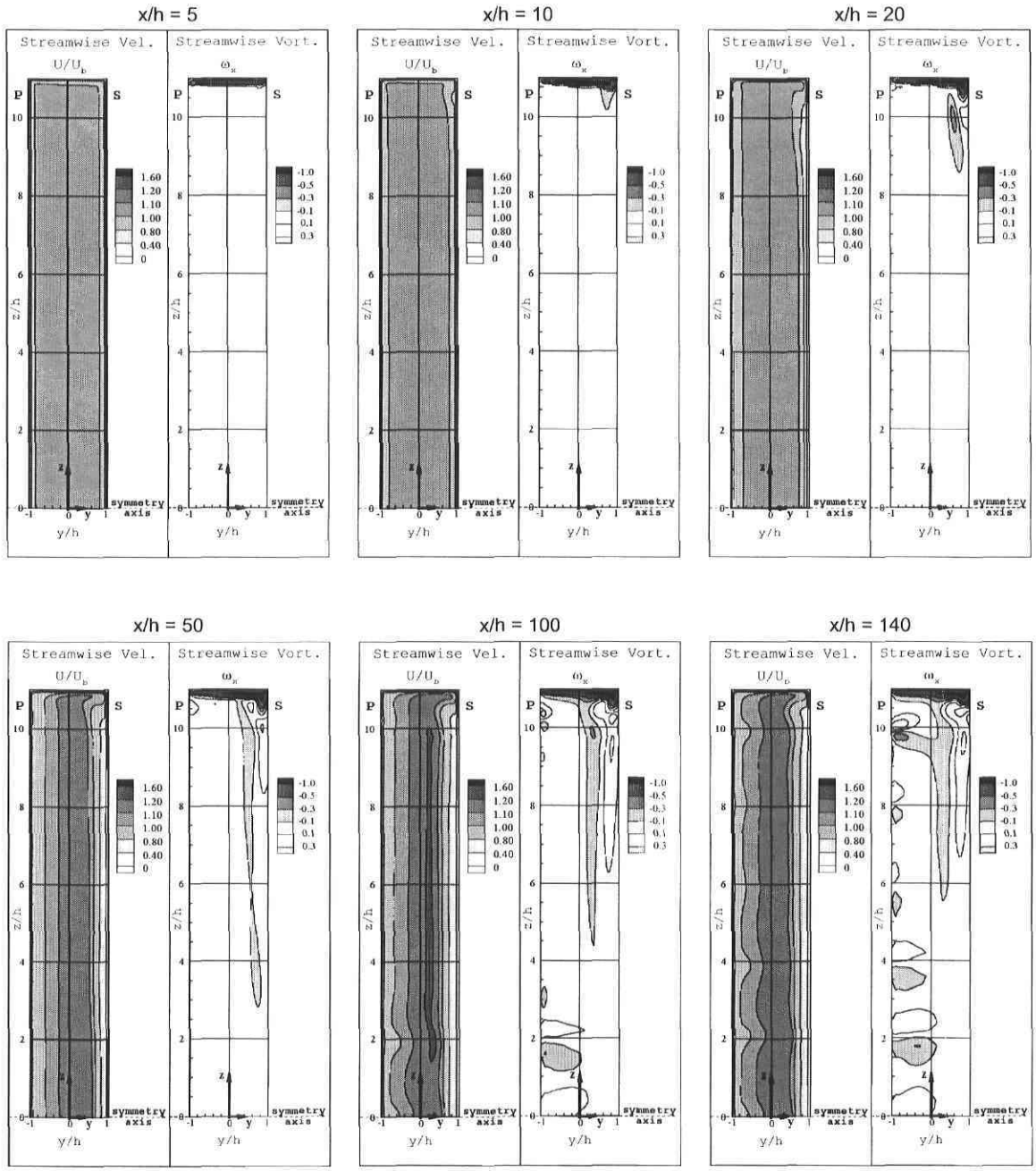

Figure 7.19: Plane contours at different stations along the straight duct at $Re = 20000$ and $Ro = 0.22$. Flow direction toward the observer.

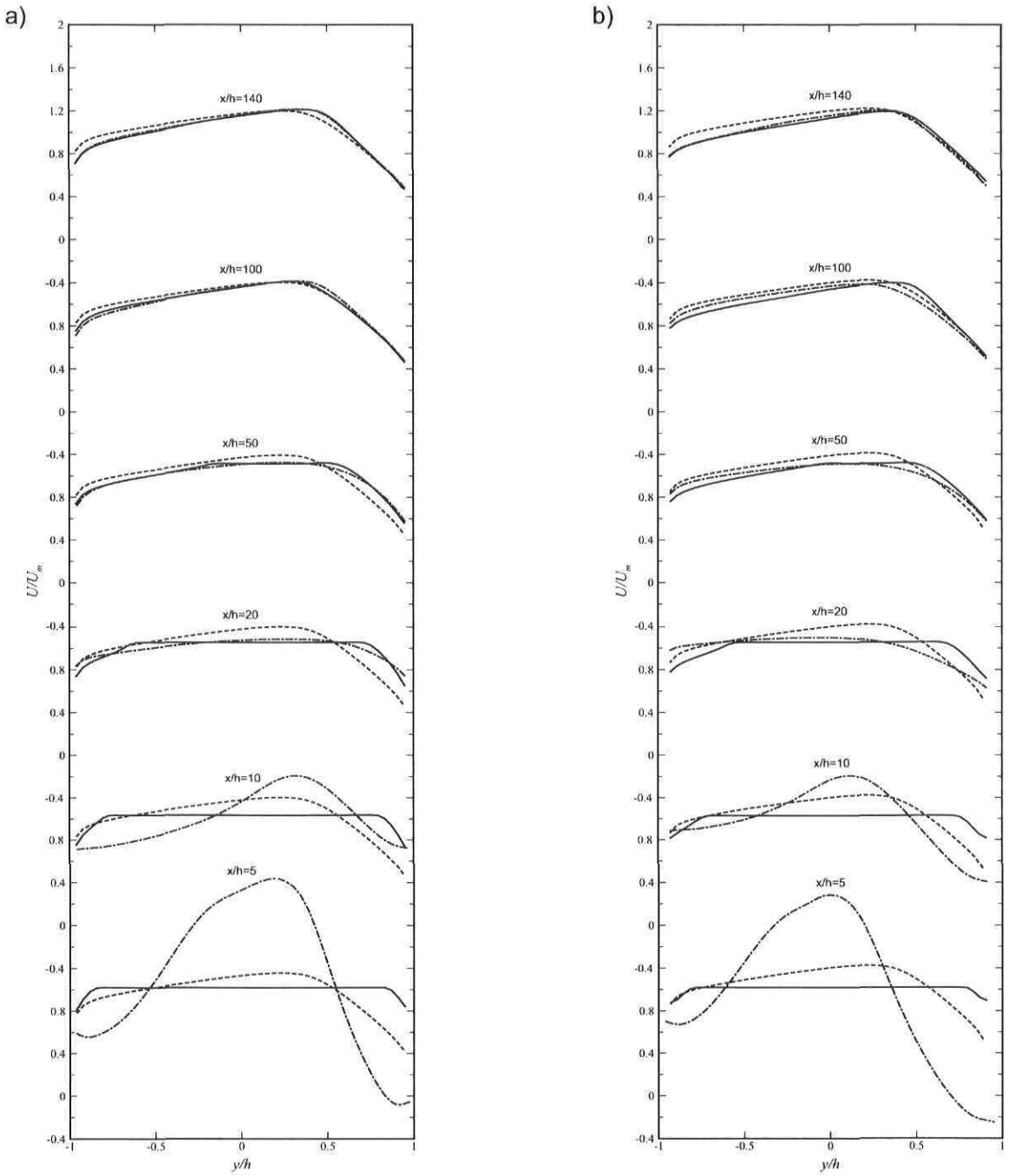

Figure 7.20: Streamwise velocity profiles at the symmetry plane of a rotating duct at $Ro = 0.22$. ——, Straight duct; — - —, actual duct; – –, fully developed solution. (a): $Re = 40000$; (b): $Re = 20000$.

To estimate the degree of flow development in the actual duct, the evolution of the streamwise velocity at the symmetry plane is plotted (see FIG. 7.20). As it was observed for the 2D case, the inlet region is characterized by a large momentum surplus in the central portion of the duct. At both Reynolds numbers, the presence of a separation bubble on the suction side is visible at $x/h = 5$, and a distance of approximatively $15h$ is required to diffuse this momentum surplus. At the two most downstream stations, the effect of the roll cell instability becomes noticeable via a momentum deficit in the destabilized region of the duct. Overall, no significant improvement of the flow development is observed in the actual duct since the benefits of a "pre-development" in the lateral channels are canceled by two large separations zones.
In conclusion, the 180° turns are detrimental to the flow development since they generate two strong centrifugal vortices that significantly alter the development of the Ekman layer. Moreover, the bends cause a large flow separation at the inlet of the main channel, which results in a deformation of the streamwise velocity profile and, in the experimental setup, may even cause a pulsating flow. Consequently, it is recommended to place a set of guides in the 180° turns in order to reduce the strength of the centrifugal vortices, and to eliminate all separation bubbles.

7.3 Improvements on the actual design

In chapter 6, a design was proposed to eliminate the separations bubbles at the entrance of the main channel. The configuration (see FIG. 6.12) consisted of three guides, strategically placed in each 180° turn, in order to have a proper momentum distribution at the entrance of the main channel. This solution allowed to remove all separations, but it didn't result in a substantial improvement of the flow development. The same design is now tested for a finite aspect ratio duct, and particular attention is given to the effect of the guides on the dynamics of the centrifugal vortices.
The duct has a length of $140h$, a width of $2h$ and an aspect ratio of 11. Fully developed conditions are set at the entrance plane of the two lateral channels ($4h$ upstream of the 180° turn), whereas an *outflow* condition is placed at the outlet boundary.
The mesh discretization in the x and y-direction are identical to the 2D case and 80 elements are used in the z-direction. The domain has 3 000 000 cells in total.
The configuration is tested for the rotating case ($Ro = 0.22$) at $Re = 40000$ and $Re = 20000$ to insure that the guides perform well over a reasonable range of flow regimes.
As shown in FIG. 7.21, for both Reynolds numbers, no separation bubble is present at the entrance of the main channel and momentum is more uniformly distributed across the duct. Thus, the set of guides removes all potential sources of pulsating flow.

The six guides also cause a breakage of the two centrifugal vortices into eight vortices of smaller size. As illustrated in the streamwise vorticity contours of FIG. 7.22, the small centrifugal cells are dissipated more quickly and their interaction with the Ekman layer is less intense. This allows a rapid development of the Ekman vorticity and of the end-wall generated secondary flow. It is interesting to notice that in the modified setup,

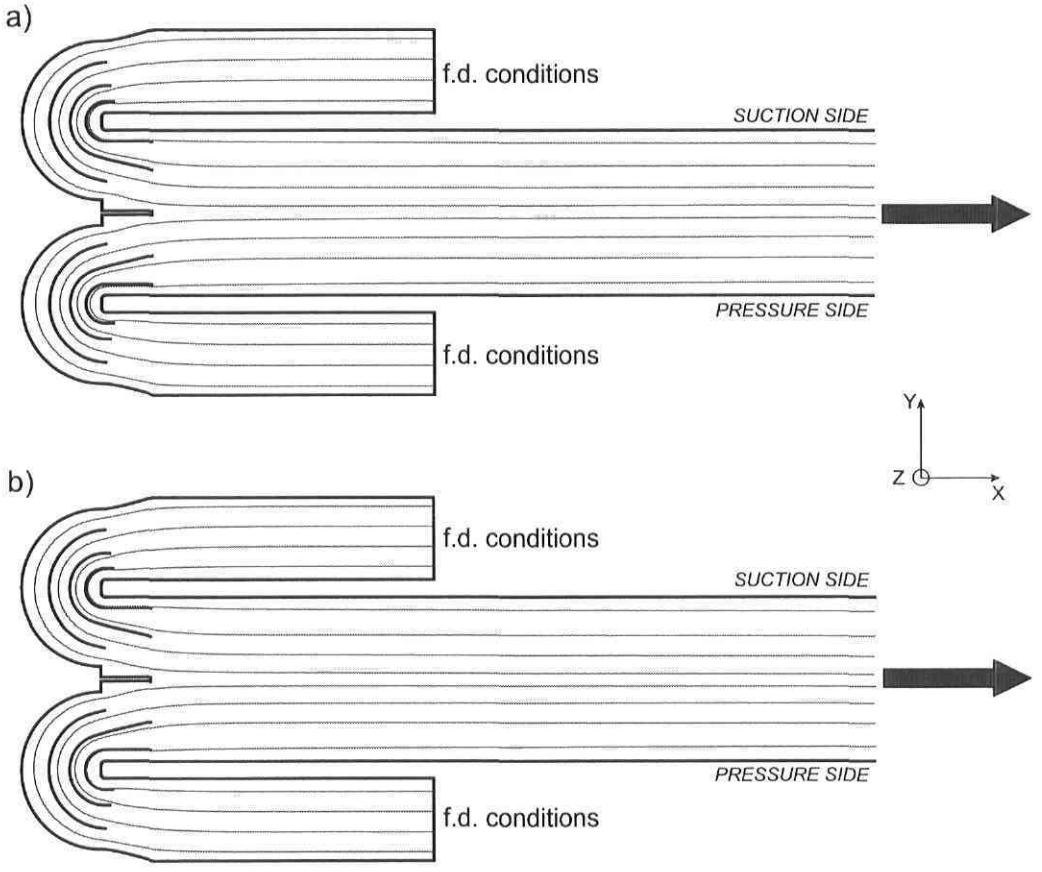

Figure 7.21: Streamlines at the symmetry plane of the modified rotating duct. (a): $Re = 40000$; (b): $Re = 20000$.

no counter-rotating longitudinal cells are visible at the entrance of the main channel, whereas two pairs where present in the basic configuration (see FIG. 7.16). A possible explanation is that in the actual duct, the separation bubbles induce a large flow acceleration in the central portion of the duct that stretches/amplifies the streamwise vortices.

The removal of the recirculating region has a profound effect on the flow development in the rotating duct and on the streamwise velocity in particular. The profiles of FIG. 7.24 confirm that the momentum surplus near the modified duct inlet has disappeared. The small wiggles visible at $x/h = 5$ are due to the wake generated behind each guide.

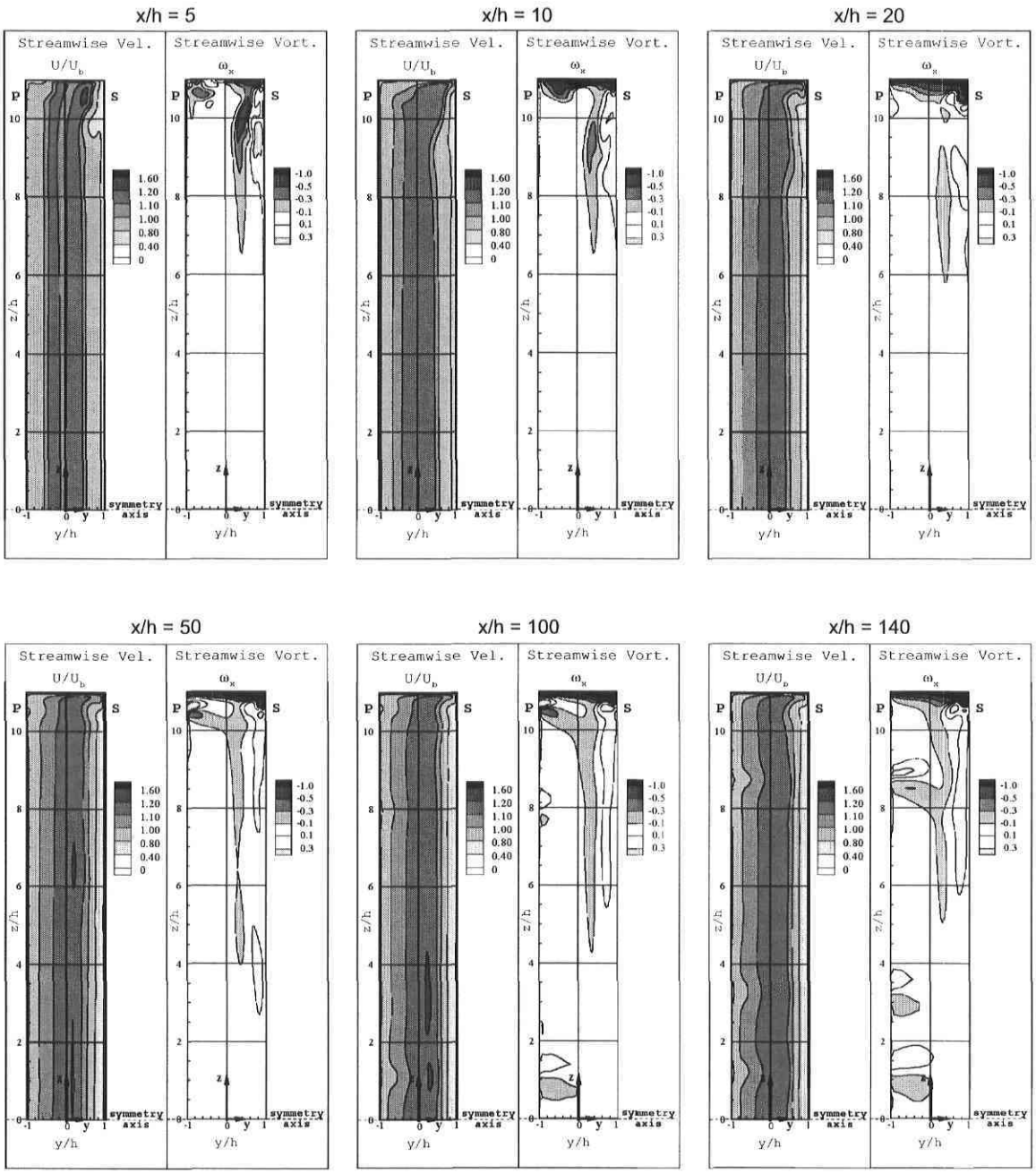

Figure 7.22: Plane contours at different stations along the modified duct at $Re = 40000$ and $Ro = 0.22$. Flow direction toward the observer.

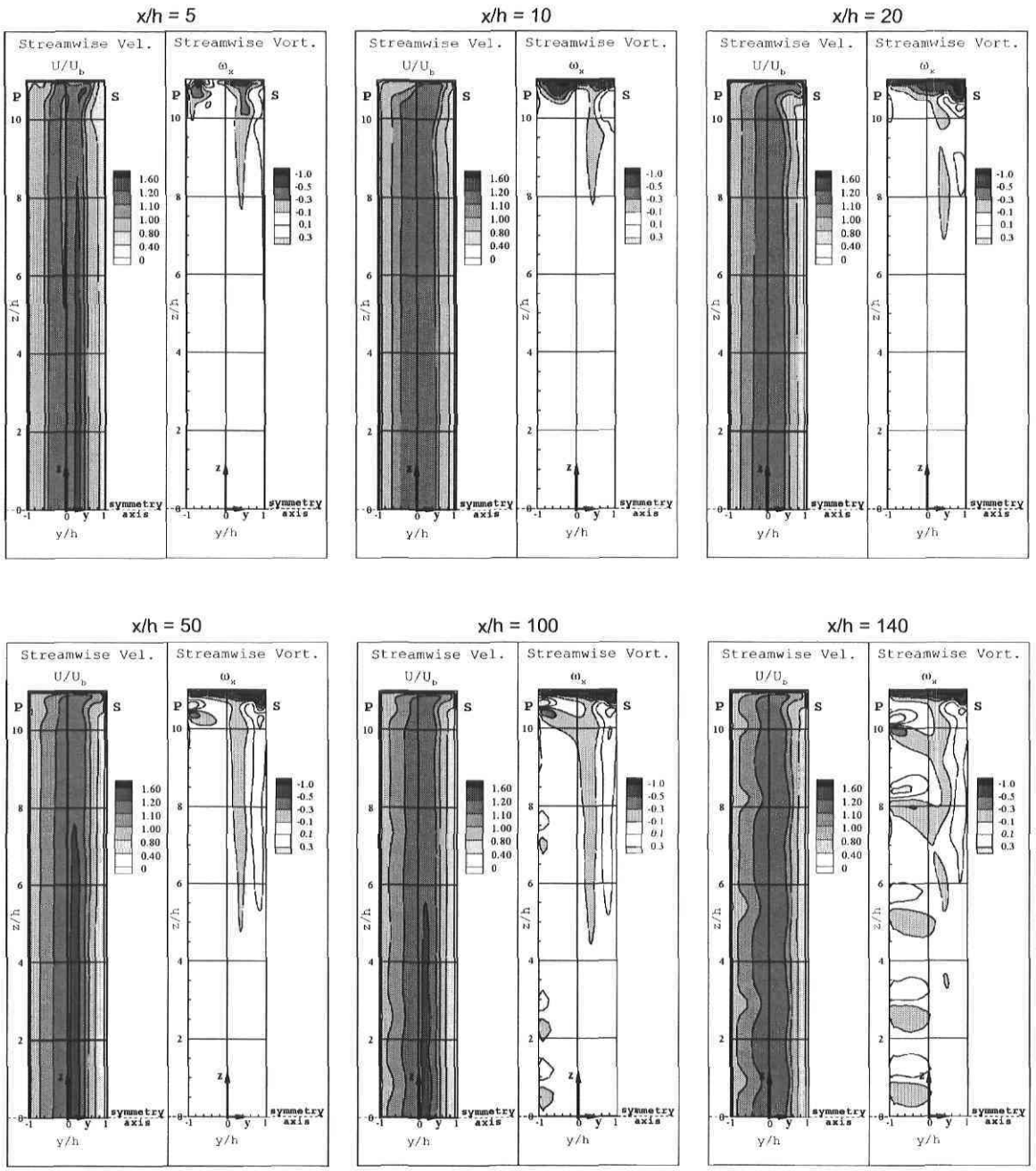

Figure 7.23: Plane contours at different stations along the modified duct at $Re = 20000$ and $Ro = 0.22$. Flow direction toward the observer.

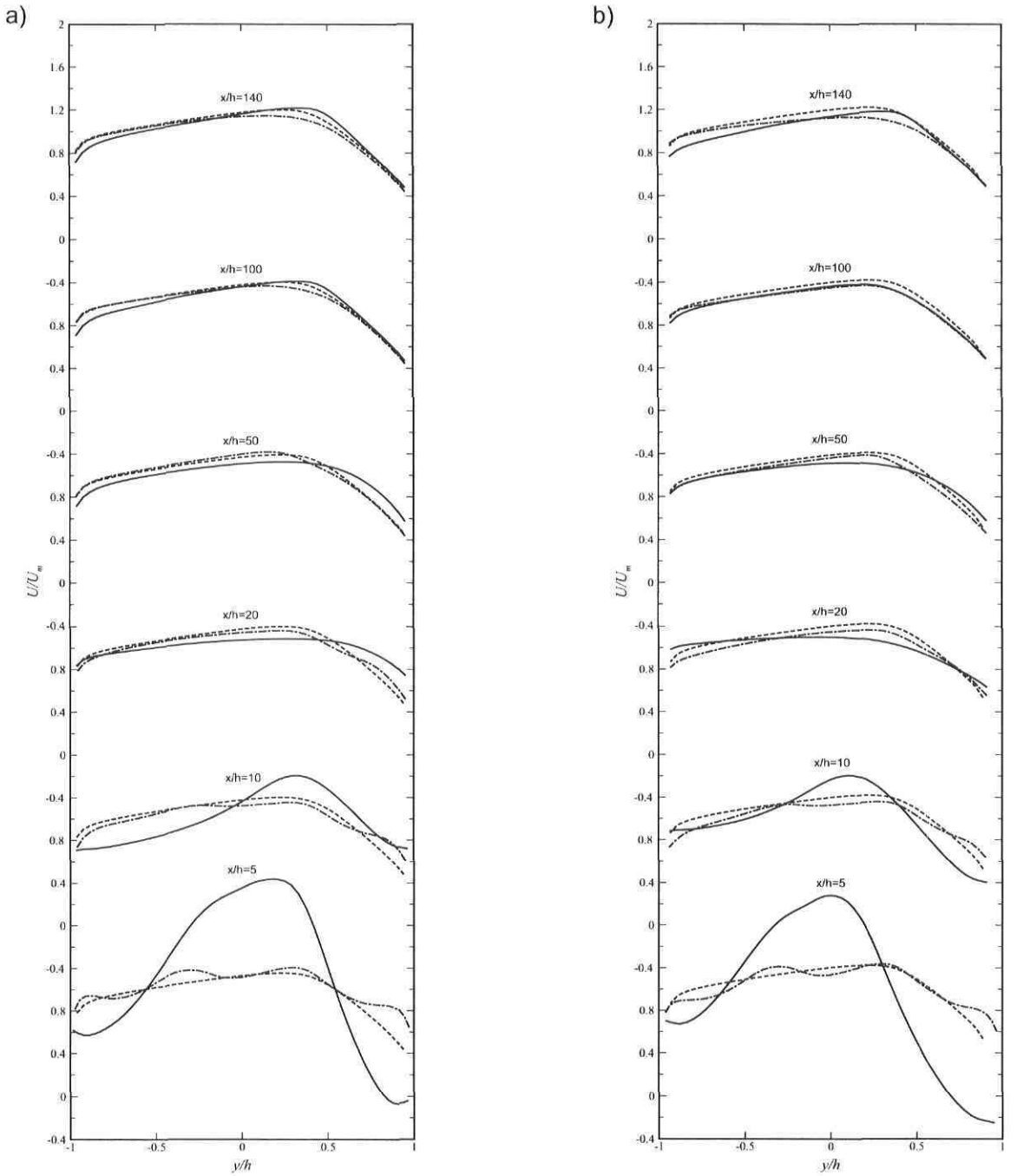

Figure 7.24: Streamwise velocity profiles at the symmetry plane of a rotating duct at $Ro = 0.22$. ——, Actual duct; — – —, modified duct; – –, fully developed solution. (a): $Re = 40000$; (b): $Re = 20000$.

Clearly, the new configuration accelerates the flow development since, at $x/h = 50$, the streamwise velocity profiles already has the main features of a fully developed solution. However, as it was observed in the straight and actual ducts, no fully developed state is attained because of the presence of tilted roll cells in the solution.
In conclusion, the 3D computations have confirmed the ability of the proposed design to completely remove all separation bubbles at the entrance of the main channel. Moreover, a notable improvement in the flow development is observed, particularly at $Re = 40000$. Consequently, this design fulfills both objectives, and its relative simplicity facilitates its implementation in the experimental setup.

Chapter 8

Unsteady fully developed flow in a rotating duct

Unsteady RANS calculations of the flow in a rotating duct of aspect ratio 11 are performed in order to capture the dynamic behaviour of the counter-rotating longitudinal vortices, and to verify if an unsteady but fully developed solution ($\partial/\partial x = 0$) can exist. In order to determine whether the end-wall generated secondary flow is solely responsible for the "unsteadiness" of the problem, calculations are also performed in a rotating duct of infinite aspect ratio.

8.1 Unsteady calculation in a rotating duct of finite aspect ratio

URANS simulations are run on a rotating duct of $AR = 11$ to investigate the interaction between the Ekman generated secondary flow and the Taylor-Görtler cells. Furthermore, the results will establish if an unsteady fully developed solution can exist in a rotating duct of finite aspect ratio. This study is performed at $Re = 40000$ and $Ro = 0.22$.

The computational domain is identical to the one used in section 5.2 for steady fully developed calculations (see FIG. 5.3). The mesh has 58650 cells: 5 elements in the x-direction, 51 in the y-direction and 230 in the z-direction. The discretization in the spanwise direction was specifically chosen in order to resolve very well the counter-rotating vortices along the pressure wall of the duct.

All unsteady calculations are performed using a second order implicit scheme for time

discretization, and thus the time step is not required to satisfy a stability criterion. However, for better accuracy, the time step $\Delta t^* = \Delta t\, U_b/h$ has been set to 0.01 in order to yield a Courant number ($C = U_i\, \Delta t/\Delta x_i$) of less than 1 everywhere in the domain. Computations with a coarser Δt^* of 0.1 have revealed no significant differences in the dynamics of the roll cells, except for a small phase change. Hence, a time step of 0.01 guarantees a good level of accuracy.

The solution is initialized with a uniform velocity profile with no turbulence, as to reproduce the conditions that were set at the entrance of the straight duct in the steady flow development calculations.

The instability starts to appear after a period $t^* = t\, U_b/h \approx 30$ at a location in the yz plane very similar to the one that was found in the straight duct (see FIG. 7.9). Once again, the secondary Ekman flow seems to hinder the formation of the instability since the first vortex pair always appears near the symmetry plane of the duct, i.e., where the cross-stream current is the weakest.

As illustrated in FIG. 8.1, the number of counter-rotating vortices in the duct increases with time, but stabilizes around a value of six pairs. The roll cells are now parallel to the xy plane (i.e., they are horizontal and they satisfy the fully developed condition $\partial/\partial x = 0$). However, they are unsteady since they are convected by the Ekman secondary flow toward the upper wall of the duct, at a rate analogous to the one found in the flow development calculation which was responsible for the tilting of the steady roll cells. Once more, when a vortex reaches the upper boundary, it is quickly dissipated and soon replaced by a new pair.

The wavy pattern visible on the velocity contours is due to the transport of momentum by the counter-rotating vortices. As shown by the contours of transverse velocity V/U_b of FIG. 8.2, the flow is swept away from the pressure wall between the positive and negative members of each vortex pair, whereas fast moving fluid is drawn toward the pressure wall between the pairs. At the symmetry plane of the duct, the vortex pair induces a transverse velocity ($V/U_b \approx 0.04$) in the positive y-direction which alters the streamwise velocity profile. The same transport mechanism applies for turbulence since highly turbulent fluid is convected by the vortical structures away from the pressure side, thus enhancing the turbulence level in the stabilized region of the duct.

The last four profiles of FIG. 8.3b show that, compared to the fully developed steady solution in a 2D channel ($\partial/\partial z = 0$), the "three-dimensional" profile presents a momentum deficit in the region close to the pressure side wall, since slow moving fluid is being convected away from that wall, at the symmetry plane ($z/h = 0$). The disparity is even greater when the comparison is made with the steady fully developed solution (FIG. 8.3a) since in the latter case no roll cells were present and the end-wall generated flow induced a transverse velocity in the negative y-direction, at the symmetry plane.

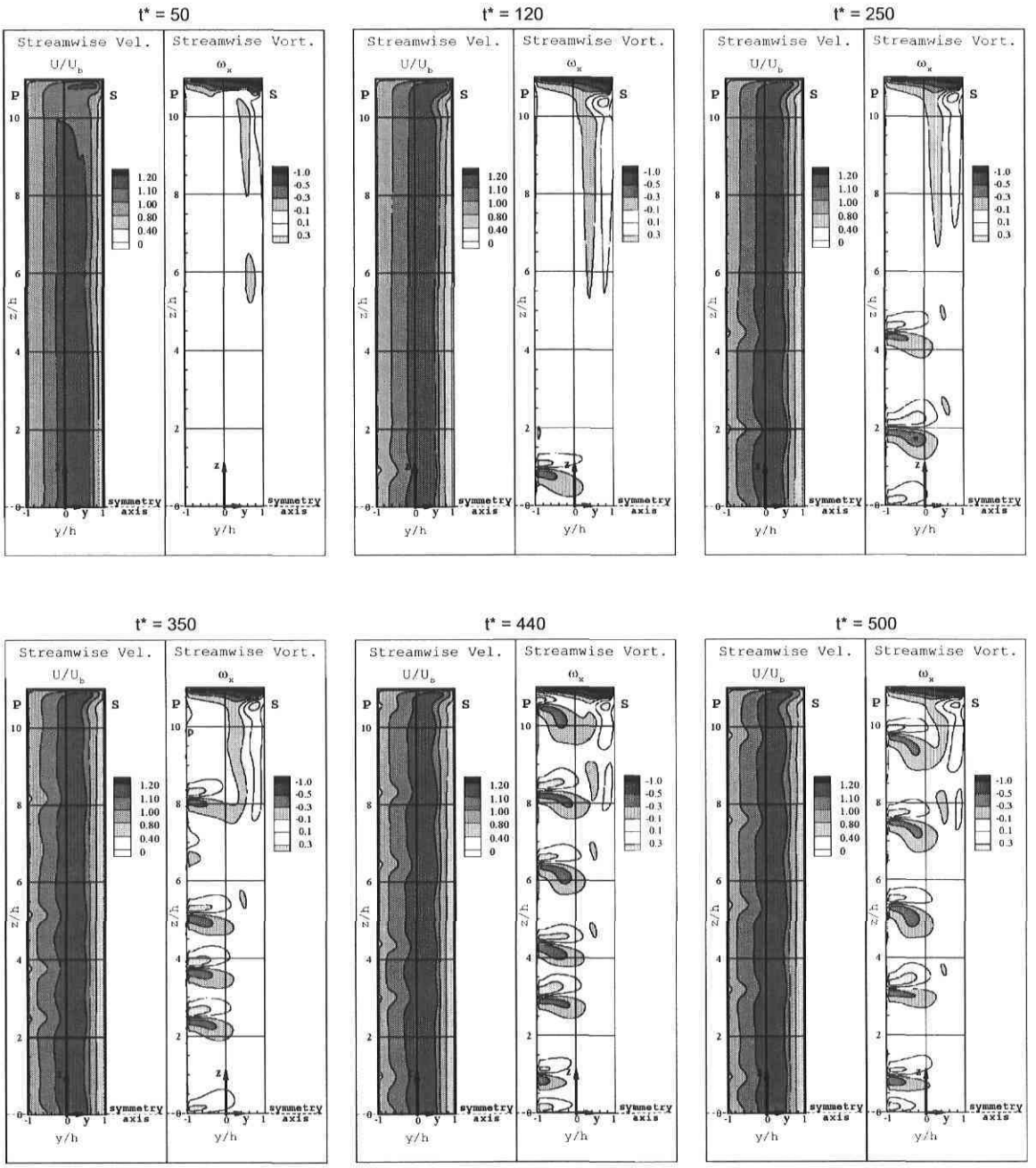

Figure 8.1: Unsteady flow in a rotating duct at $Re = 40000$ and $Ro = 0.22$. Flow direction toward the observer.

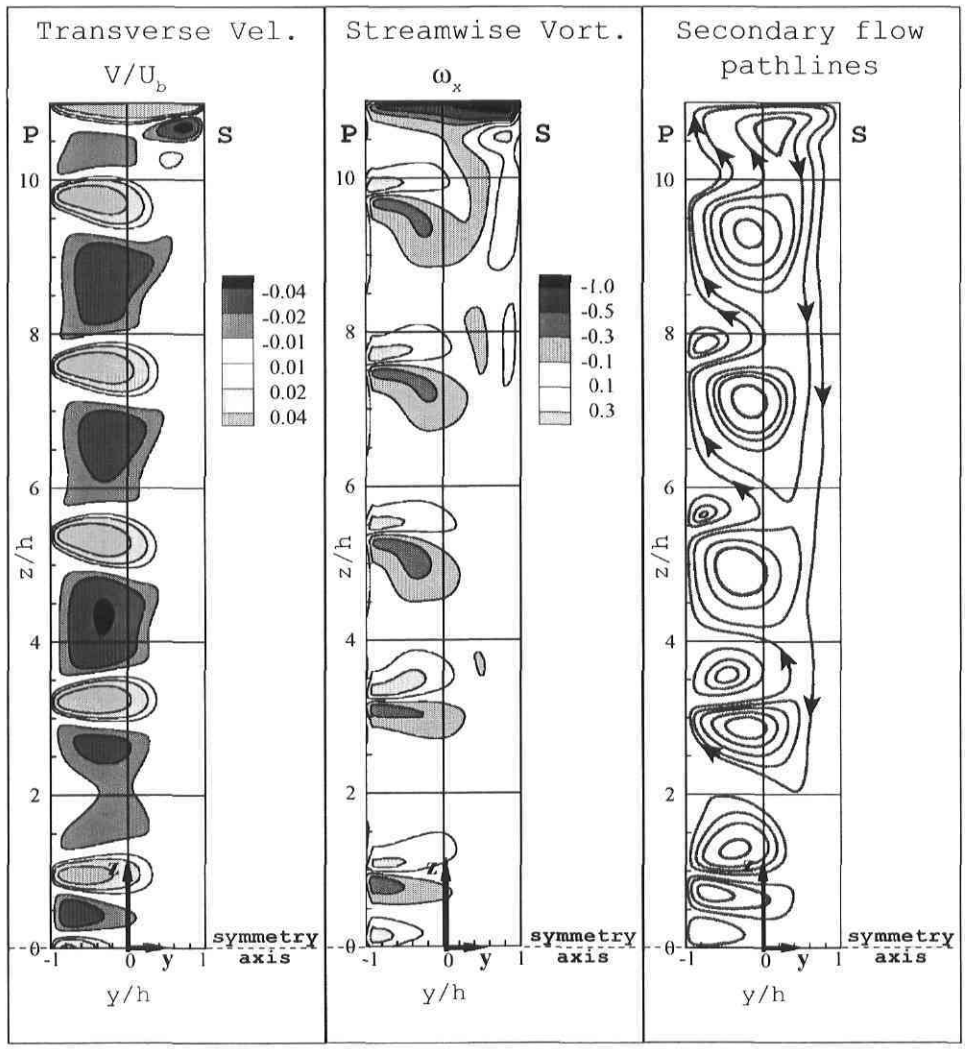

Figure 8.2: Plane contours and secondary flow pathlines at $t^* = 500$ in a rotating duct at $Re = 40000$ and $Ro = 0.22$. Flow direction toward the observer.

The analysis that was presented at the end of chapter 5 to help explain the discrepancies between the experimental results (Maciel *et al.*, 2003) and the DNS data (Alvelius *et al.*, 1999) remains valid since at $Re \approx 3000$ it is not clear whether the roll cells would be present in the experimental setup, but it is certain that the end-wall generated secondary flow does exist. Furthermore, the real flow does not have to satisfy a symmetry condition at $z/h = 0$ and thus the z-position of the roll cells in the central region of the experimental setup may differ from the numerical solution.

In summary, the time dependent calculation has shown that a fully developed flow ($\partial/\partial x = 0$) can exist in a rotating duct of finite aspect ratio, but the solution is found to be unsteady. The time varying character of the flow is due to the transport effect associated with the Ekman secondary flow.

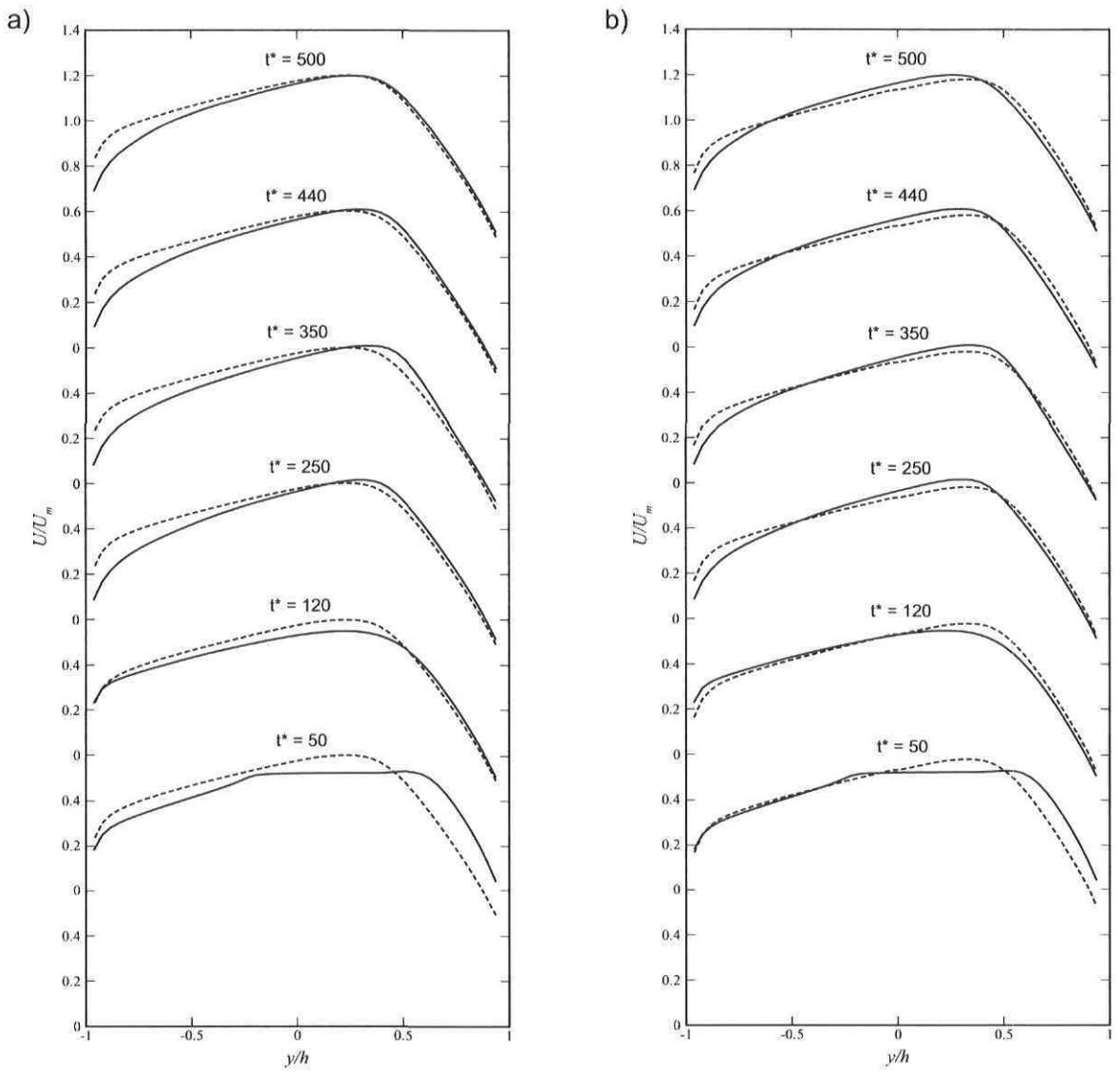

Figure 8.3: Streamwise velocity profiles in a rotating duct at $Re = 40000$ and $Ro = 0.22$. (a): ——, 3D unsteady case at $z/h = 0$; – –, 3D steady case at $z/h = 0$. (b): ——, 3D unsteady case at $z/h = 0$; – –, 2D steady case.

8.2 Unsteady calculation in a rotating duct of infinite aspect ratio

To verify if the end-wall generated secondary flow is solely responsible for the "unsteadiness" of the previous solution, URANS calculations are performed at $Re = 40000$ and $Ro = 0.22$ in a rotating duct of infinite aspect ratio, where the Ekman layer cannot develop since no end-walls are present.
The computational domain has the same length of the one used in the previous section, but has an aspect ratio of 3. Periodic conditions are applied in both the streamwise and spanwise directions in order to reproduce the fully developed solution in a duct of infinite aspect ratio. In the streamwise and spanwise directions, the mesh is identical to the previous case, and in the spanwise direction the discretization is done with 60 uniform cells. This yields a regular mesh of 15300 cells.
To reduce CPU time, a few iterations are performed with a steady solver and the "intermediate" solution is then set as initial condition for the unsteady simulation.
After a period of $t^* \approx 250$ ($\Delta t^* = 0.01$), the time dependent simulation evolves toward the steady state solution of FIG. 8.4, where three Taylor-Görtler vortex pairs are uniformly distributed with respect to the spanwise periodic boundaries. This configuration

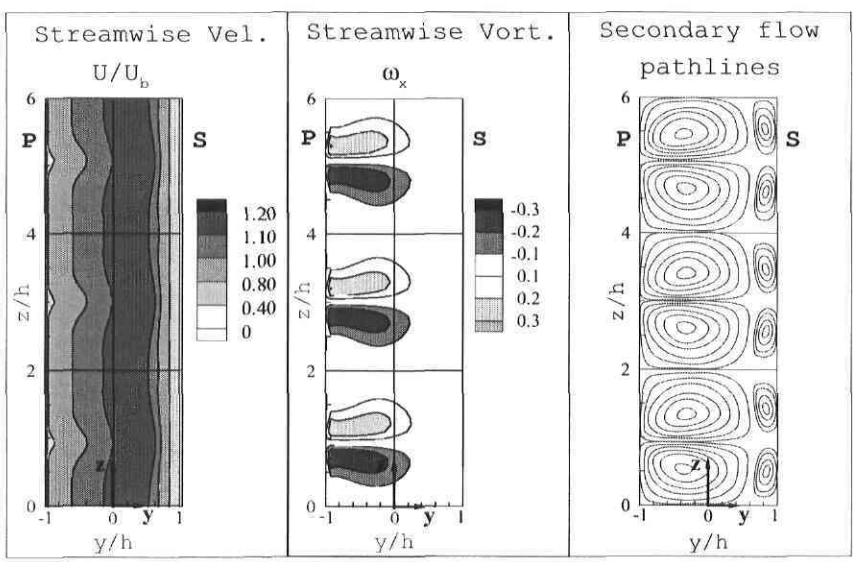

Figure 8.4: Steady state solution in a rotating duct of $AR = \infty$ (periodic length of $6h$ imposed) at $Re = 40000$ and $Ro = 0.22$. Flow direction toward the observer.

represents only one of the possibilities since, theoretically, the actual phase (z-position) of the roll cells is arbitrary. During the unsteady calculation, small displacements of the vortex pairs in the spanwise direction were observed and caused the relatively long time needed to reach the permanent solution.

In the steady state, the vortex pairs have a width of $1.5h$ and a wavelength of $2h$. These values are in good agreement with both the DNS data of Kristoffersen & Andersson (at $Re \sim 3000$, $Ro = 0.2$) and the experimental results of Johnston *et al.* (at $Re \sim 3000$, $Ro \sim 0.22$). However, the vortical structures are found to be more stable and persistent in time in the current URANS calculations, which may be due to the higher Reynolds number.

The secondary flow streamlines of FIG. 8.4 show the presence of six small vortices on the suction side wall of the duct in reaction to the Taylor-Görtler vortices. Those recirculating cells were not present in the rotating duct of finite aspect ratio due to the descending Ekman flow.

In conclusion, the present results show that a steady fully developed solution can exist in a rotating channel of infinite aspect ratio, and that the end-wall generated secondary flow is responsible for the "unsteadiness" in the rotating duct of $AR = 11$.

Chapter 9

Conclusion

Steady and unsteady RANS simulations have been run with a stress transport turbulence model to investigate basic flow characteristics and flow development in the entrance region for high aspect ratio turbulent duct flows under moderate rotation conditions.

Results have shown that rotation confines spanwise viscous effects in an Ekman-type layer near the end-walls, leading to a substantial quasi two-dimensional zone ($\partial/\partial z \approx 0$). However, the secondary flow generated near the upper and lower boundaries causes transverse advection and additional Coriolis forces which alter the streamwise velocity profile in such a way that it differs noticeably from the 2D channel case. Consequently, the presence of a "two-dimensional zone" ($\partial U/\partial z \approx 0$) in the rotating duct does not guarantee that the solution corresponds to the theoretical 2D case. Comparisons between experimental results (even for high aspect ratio ducts) and 2D numerical computations should thus be performed very cautiously.

Flow development computations in a plane 2D channel ($\partial/\partial z = 0$) have revealed that the entrance length increases with the presence of moderate system rotation since the Coriolis force has a stabilizing effect on the suction side that lessens the growth of the boundary layer. At high Ro, where stabilization occurs on both the pressure and suction sides, the difference in development length should become even greater. It was also noted that the distance required to reach full development (at 0.5% RMS criterion) is much longer for turbulent quantities than for momentum.

In a duct of aspect ratio 11, the flow development is greatly affected by the appearance of Taylor-Görtler cells near the pressure wall. A significant interaction of the vortical structures with the end-wall generated secondary flow is observed and, under the action of this cross-stream current, the roll cells are either tilted toward the end wall in steady flow computations or convected toward the end-wall in unsteady flow computations. Over a length of more than $300h$, no steady fully developed solution is

therefore reached since the slope of the counter-rotating "streamwise" vortices implies that $\partial/\partial x \neq 0$.

Unsteady flow calculations in a streamwise periodic domain ($\partial/\partial x = 0$) have shown that a fully developed solution can exist in a rotating duct of finite aspect ratio, but the flow cannot reach a steady state since the longitudinal roll cells are constantly convected by the Ekman secondary flow. The counter-rotating vortices are quickly dissipated when they reach the end-wall but new vortex pairs appear near the symmetry plane, thus perpetuating the unsteady character of the flow. Consequently, the presence of end walls with their unavoidable secondary flow has a twofold effect: it causes the flow to be time dependent, and it appears to hinder somewhat the formation of the roll cells, forcing the instability to initially develop near the symmetry plane of the duct.

The steady state solution of the infinite aspect ratio duct (no end-walls) suggests that the natural wavelength of the roll cell instability at $Re = 40000$ and a $Ro = 0.22$ is approximately $2h$, and that the width of the roll cell is about $1.5h$. The vortex pair closely preserves its dimensions in the duct of $AR = 11$ except close to the end wall where its interaction with the cross-stream current becomes too strong.

The second objective of the present work was to compare the flow development between a straight duct with a uniform velocity inlet and the actual duct built in the Experimental Fluid Mechanics Laboratory at Laval University. In the latter, the main channel is preceded by two lateral feeding channels that merge after a 180° turn and which contribute to "pre-develop" the flow.

3D computations have shown that the 180° turns are detrimental to the flow development since they generate two strong centrifugal vortices that significantly alter the development of the Ekman layer. Moreover, the bends cause a large flow separation at the inlet of the main channel which may cause a pulsating flow in the experimental setup.

An intensive study was done in order to correct these problems (see some of the ideas tested in Appendix B) and the final design consists of three guides strategically positioned in each 180° turn. This configuration allows to remove all separations bubbles at the entrance of the main channel, and significantly reduces the size of the centrifugal vortices. Consequently, the development of the Ekman layer is accelerated and the overall flow development is improved.

Recommendations for future work

The present numerical study has provided complementary information on the flow development and flow characteristics in a rotating duct of high aspect ratio. However, the following investigations could provide some very interesting prospects:

- *Unsteady flow development calculations would be useful in order to clarify the appearance and behavior of roll cells in an actual rotating duct.*
- *Experimental confirmation of the presence and impact of the secondary flow as well as the longitudinal roll cells would represent a significant and fundamental contribution in the field.*

Bibliography

ALVELIUS, K. & JOHANSSON, A.V. 1999 *Direct numerical simulation of rotating channel flow at various Reynolds numbers and Rotation numbers.* Doctoral Thesis of Alvelius. KTH Mechanics, Stockholm (Sweden).

EL TELBANY, M.M.M. & REYNOLDS, A.J. 1980 Turbulence in plane channel flows. *J. Fluid Mech.*, **111**, 283-318.

FERZIGER, J.H. & PERIĆ, M. 2002 *Computational Methods for Fluid Dynamics.* Springer, New York (US).

FLETCHER, C.A.J. 1991 *Computational Techniques for Fluid Dynamics.* Volume 1. Springer, New York (US).

FLUENT 6.1 *User's Guide*, Fluent Inc. 2003.

GALLETTI, B. & BOTTARO, A. 2004 Large-scale secondary structures in duct flow. *J. Fluid Mech.*, **512**, 85-94.

HART, J.E. 1971 Instability and secondary motion in a rotating channel flow. *J. Fluid Mech.*, **45**(2), 341-351.

HOPFINGER, E.J. & LINDEN, P.F. 1990 The effect of background rotation on fluid motion: a report on Euromech 245. *J. Fluid Mech.*, **211**, 417-435.

JOHNSTON, J.P., HALLEEN, R.M. & LEZIUS, D.K. 1972 Effects of spanwise rotation on the structure of two-dimensional fully developed turbulent channel flow. *J. Fluid Mech.*, **56**(3), 533-557.

JULIEN, S., TORRIANO, F., DUMAS, G. & MACIEL, Y. 2005 Investigation of the 3D inlet flow characteristics in a rotating channel setup. In *20th Canadian Congress of Applied Mechanics*, 571-572, Montreal.

JULIEN, S., TORRIANO, F. & DUMAS, G. 2006 Rotating turbulent duct flows — Part I: End-wall effects on two-dimensionality. In *14th Ann. Conf. of the CFD Society of Canada, Paper CFD-2006-1077*, Kingston.

KRISTOFFERSEN, R. & ANDERSSON, H.I. 1993 Direct simulations of low-Reynolds-number turbulent flow in a rotating channel. *J. Fluid Mech.*, **256**, 163-197.

LAUNDER, B.E., TSELEPIDAKIS D.P. & YOUNIS, B.A. 1987 A second-moment closure study of rotating channel flow. *J. Fluid Mech.*, **183**, 63-75.

LEZIUS, D.K. & JOHNSTON, J.P. 1976 Roll-cell instabilities in rotating laminar and turbulent channel flows. *J. Fluid Mech.*, **77**, 153-175.

MACFARLANE, I., JOUBERT, P.N. & NICKELS, T.B. 1998 Secondary flows and developing turbulent boundary layers in a rotating duct. *J. Fluid Mech.*, **373**, 1-32.

MACIEL, Y., PICARD, D., GLEYZES, C., YAN, G., & DUMAS, G. 2003 Fully developed turbulent channel flow subject to system rotation. In *33rd AIAA Fluid Dynamics Conference and Exhibit, Paper AIAA-2003-4153*, Orlando (US).

MACIEL, Y., YAN, G., & DUMAS, G. 2005 Experiments on turbulent channel flow subject to system rotation. In *20th Canadian Congress of Applied Mechanics*, 569-570, Montreal.

MÀRTENSSON, G. 2004 *Experimental and numerical study of turbulent flow in rotating ducts.* Licentiate Thesis. KTH Mechanics, Stockholm (Sweden).

MÀRTENSSON, G. 2006 *Analysis of laminar and turbulent flows with turbomachinery, biotechnology and biomechanical applications.* Doctoral Thesis. KTH Mechanics, Stockholm (Sweden).

MOIN, P. & KIM, J. 1982 Numerical investigation of turbulent channel flow. *J. Fluid Mech.*, **118**, 341-377.

MOIN, P. & KIM, J. 1997 Tackling turbulence with supercomputers. *Scientific American*, January issue, 62-68.

MUNSON, B.R., YOUNG D.F. & OKIISHI T.H. 1998 *Foundamentals of fluid mechanics.* John Wiley & Sons, New York (US).

NAKABAYASHI, K. & KITOH, O. 1996 Low Reynolds number fully developed two dimensional turbulent channel flow with system rotation. *J. Fluid Mech.*, **315**, 1-29.

NILSEN, P.J. & ANDERSSON, H.I. 1994 Developing turbulent flow in a rotating channel. *Int. J. Heat and Fluid Flow*, **15**(2), 100-103.

PANTON, R.L. 1996 *Incompressible Flow.* John Wiley & Sons, New York (US).

PETTERSSON, B.A. & ANDERSSON, H.I. 1997 Near-wall Reynolds-stress modeling in noninertial frames of reference. *Fluid Dynamics Research*, **19**, 251-276.

PETTERSSON, B.A. & ANDERSSON, H.I. 2003 Turbulent flow in a rotating square duct: a modeling study. *Journal of Turbulence*, **4**.

SALHI, A. & CAMBON, C. 1997 An analysis of rotating shear flow using linear theory and DNS and LES results. *J. Fluid Mech.*, **347**, 171-195.

SPEZIALE, C.G. & THANGAM, S. 1983 Numerical study of secondary flows and roll-cell instabilities in rotating channel flow. *J. Fluid Mech.*, **130**, 377-395.

SPEZIALE, C.G. 1982 Numerical study of viscous flow in rotating rectangular ducts. *J. Fluid Mech.*, **122**, 251-271.

TORRIANO, F., JULIEN, S., & DUMAS, G. 2006 Rotating turbulent duct flows — Part II: Flow development. In *14th Ann. Conf. of the CFD Society of Canada, Paper CFD-2006-1078*, Kingston.

TRITTON, D.J. 1988 *Physical Fluid Dynamics.* Oxford University Press, Oxford (UK).

TRITTON, D.J. 1992 Stabilization and destabilization of turbulent shear flow in a rotating fluid. *J. Fluid Mech.*, **241**, 503-523.

WATMUFF, J.H., WITT, H.T. & JOUBERT, P.N. 1985 Developing turbulent boundary layers with system rotation. *J. Fluid Mech.*, **157**, 405-448.

Appendix A

Fully developed solution with periodic boundary conditions

With an in-house CFD code, one could solve directly the fully developed Navier-Stokes equations ($\partial/\partial x = 0$ for all velocity components and turbulence, and $\partial p/\partial x = \text{cte}$), but this approach is not provided for in *Fluent*. We rather take advantage of the existence of periodic boundary conditions offered in *Fluent* to circumvent this problem. However, special considerations on the domain length and mesh discretization in the streamwise direction must be kept in mind in order to guarantee that the solution satisfies the $\partial/\partial x = 0$ condition.

In this section, the validity of periodic conditions for computing a fully developed solution is investigated. The periodic domain is scaled by various factors in order to change the domain length and streamwise cell dimension. The domain of reference consists of a 2D channel having a length of 10h and 10 cells in the streamwise direction.

L	Δx	RMS U	RMS ν_t/ν
$40h$	$4h$	0.00098	0.017
$20h$	$2h$	0.00059	0.011
$10h$	h	–	–
$5h$	$0.5h$	0.00077	0.015
$2.5h$	$0.25h$	0.0018	0.033
$1.25h$	$0.125h$	0.0025	0.045
$0.625h$	$0.0625h$	0.031	0.054
$0.3125h$	$0.03125h$	0.0039	0.067

Table A.1: $\|\triangle\|_{RMS}$ values at the central position of a periodic domain.

The transverse direction is discretized with 51 elements. All calculations are performed at $Re = 40000$ and $Ro = 0$ (no rotation) and using the RSM turbulence model.
The plot of FIG. A.1b shows that the turbulence level increases when the periodic domain is shortened. To better quantify this variation, the RMS norm is computed between the reference case ($L = 10h$, $\Delta x = h$) and all the other configurations. The

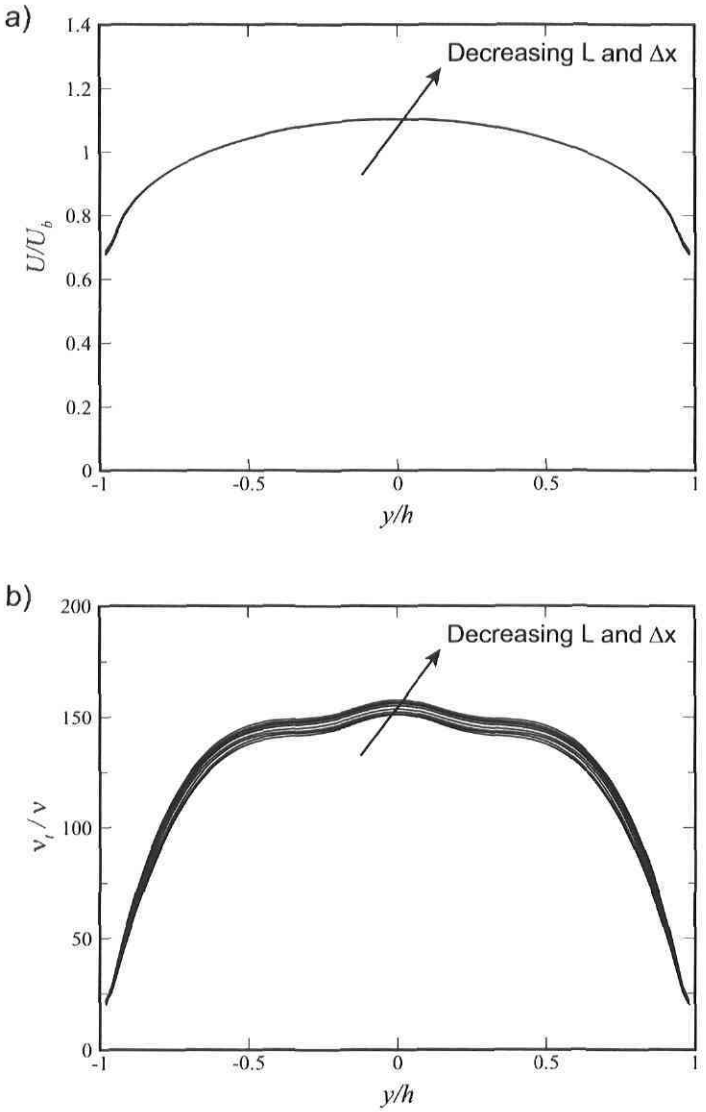

Figure A.1: 2D channel at $Re = 40000$ and $Ro = 0$. (a): Streamwise velocity profile at the center of periodic domain; (b): turbulent viscosity ratio profile at the center of periodic domain.

values of TABLE A.1 indicate that the change in the streamwise velocity is very small (below 0.5%), whereas it becomes quite important for ν_t/ν. Hence, there is a dependence of the turbulent quantities on the streamwise mesh discretization and/or domain length.
To determine which one of those two variables is affecting the solution, a new test is

performed, where only one parameter is varied at the same time. FIG. A.2 shows that a difference in the ν_t/ν profile is noted when Δx is varied (while keeping L constant) and also when L is varied (while keeping Δx constant). Thus, the turbulent viscosity ratio is affected by both the domain length and streamwise discretization. A possible

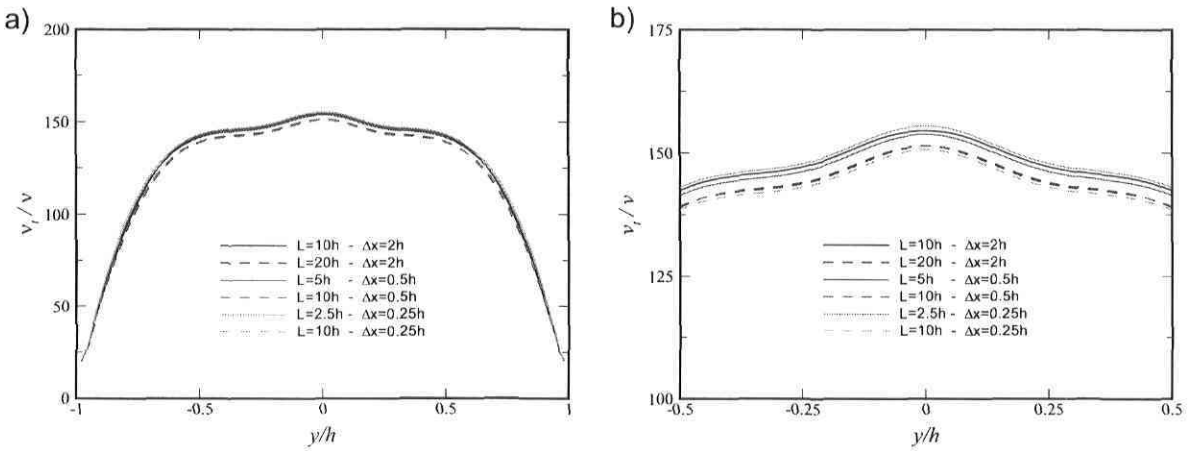

Figure A.2: 2D channel at $Re = 40000$ and $Ro = 0$. (a): Turbulent viscosity ratio profile at the center of periodic domain; (b): enlarged view of (a).

explanation is that the product $L \times N$ (where N is the number of cells in the streamwise direction) is the controlling factor. The reason being that the bigger the "effective distance" ($L \times N$) from the periodic boundaries, the less the solution in the center of the channel is affected by the boundary conditions. To validate this hypothesis, the

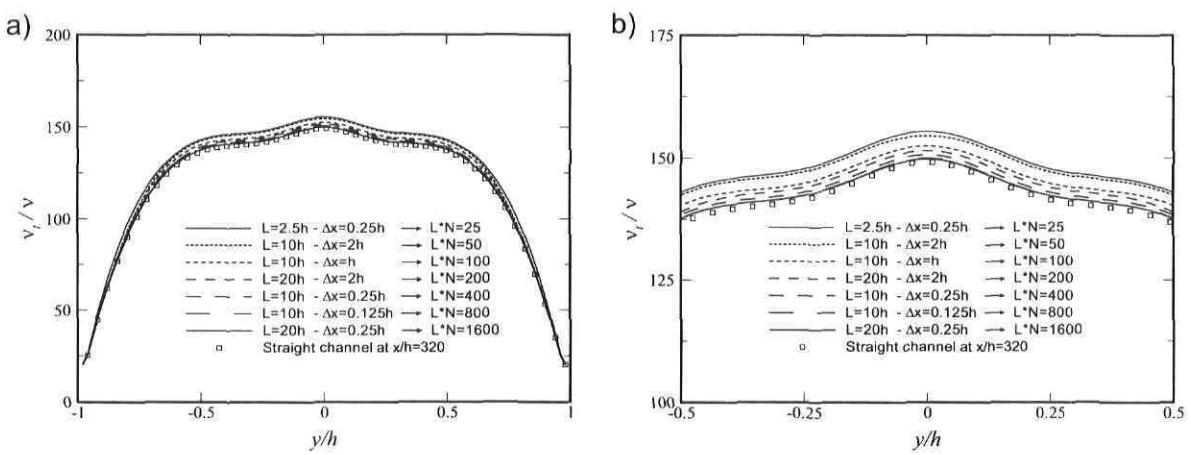

Figure A.3: 2D channel at $Re = 40000$ and $Ro = 0$. (a): Turbulent viscosity ratio profile at the center of periodic domain; (b): enlarged view of (a).

solutions obtained from periodic domains having different $L \times N$ values are compared with the fully developed ν_t/ν profile computed from a flow development in a very long and computationally expensive channel (see FIG. A.3). In the latter domain the Δx varies from $0.1h$ at the inlet to $0.4h$ at the outlet. The results show that, when the value

of $L \times N$ increases, the profile of ν_t/ν obtained with the periodic conditions approaches the "true" fully developed solution.

The periodic condition in the *Fluent* solver implies that the solution at the two periodic boundaries must be identical, but an evolution of the solution between the two boundaries is possible. To verify the parameters required to force a $\partial/\partial x = 0$ across the domain, the relative maximum amplitude of the fluctuations along the channel is computed as follows:

$$\text{variation} = \frac{\max(\phi) - \min(\phi)}{\min(\phi)}. \tag{A.1}$$

As indicated in TABLE A.2, the grid spacing in the streamwise direction (Δx) appears somewhat proportional to the amplitude of the fluctuations along the domain. In

L	Δx	U	$u'u'$	$v'v'$	$w'w'$	$u'v'$
$40h$	$4h$	0.00090	0.050	0.040	0.045	0.054
$20h$	$2h$	0.00040	0.032	0.022	0.029	0.031
$10h$	$2h$	0.00040	0.030	0.014	0.023	0.030
$10h$	h	0.00050	0.014	0.009	0.013	0.016
$10h$	$0.25h$	0.00030	0.004	0.0030	0.0040	0.0040
$2.5h$	$0.25h$	0.00030	0.0030	0.0020	0.0030	0.0040
$0.625h$	$0.0625h$	0.00020	0.008	0.00050	0.00080	0.00090

Table A.2: 2D channel at $Re = 40000$ and $Ro = 0$. Maximum variable fluctuations along a line at $y/h = -0.5$.

consequence, for a smaller Δx, all variables remain more uniform along the channel and better satisfy the fully developed condition.

In conclusion, a small Δx helps provide a $\partial/\partial x = 0$ but in order to have a "true" fully developed solution, the periodic domain should also have a large $L \times N$ (or $L^2/\Delta x$).

Appendix B

Tested designs for promoting flow development

For clarity purposes, only the final configuration aimed to promote the flow development in the actual channel was presented in section 6.3. However, many others designs were tested, and some of them are presented in this section. All calculations are performed at $Re = 40000$ and $Ro = 0.22$.

B.1 Actual channel without splitter plate

With this configuration, the splitter plate at the entrance of the main channel is removed in order to accelerate the mixing of the inlet flows coming from the two lateral channels.
The results of FIG. B.1b show that the removal of the splitter plate increases the development length. Moreover, the separation bubble on the suction side of the main channel becomes very large, and the flow is shifted toward the pressure side wall. Consequently, this solution must be discarded.

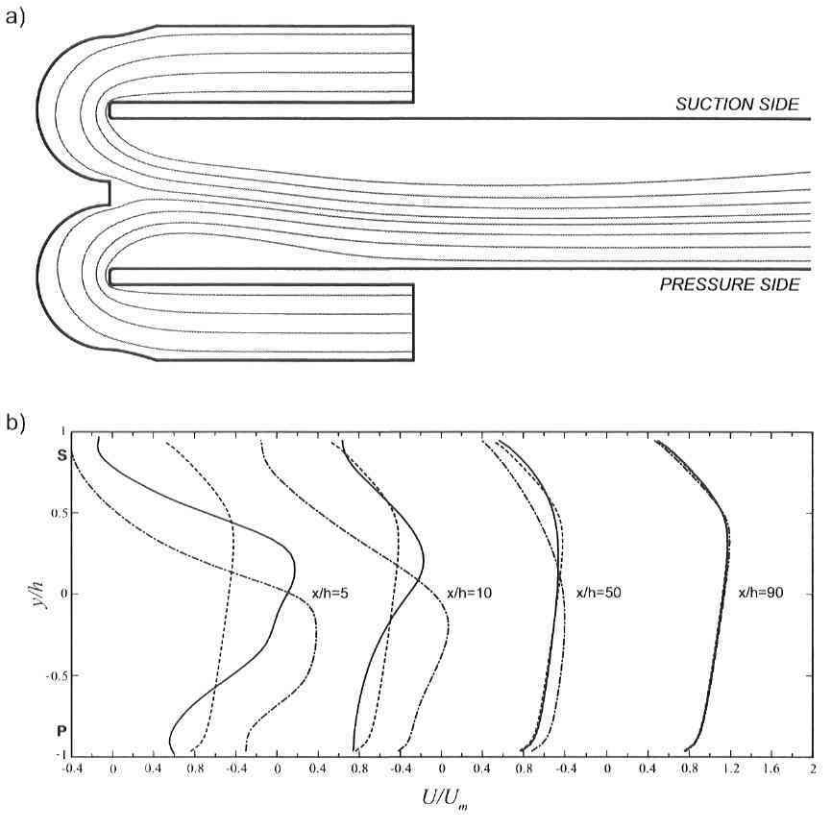

Figure B.1: 2D modified channel at $Re = 40000$ and $Ro = 0.22$. (a): Streamlines; (b): streamwise velocity profiles at different stations along the channel: ——, Actual channel; — – —, modified channel; – –, fully developed solution.

B.2 Actual channel with symmetric lips

To limit the size of the separation zones, two lips are placed at the entrance of the main channel. Although the size of the separation bubbles differs on the suction and pressure sides, the lips must be identical since the experimental setup will turn in both directions. Their shape follows the outline of the separation bubble on the pressure side of the channel (when the channel is turning counter clockwise).
As illustrated in FIG. B.2, the lips eliminate the separation bubble on the pressure side, but a recirculating zone is still present near the suction wall. The streamwise velocity profiles show no improvement in the flow development.

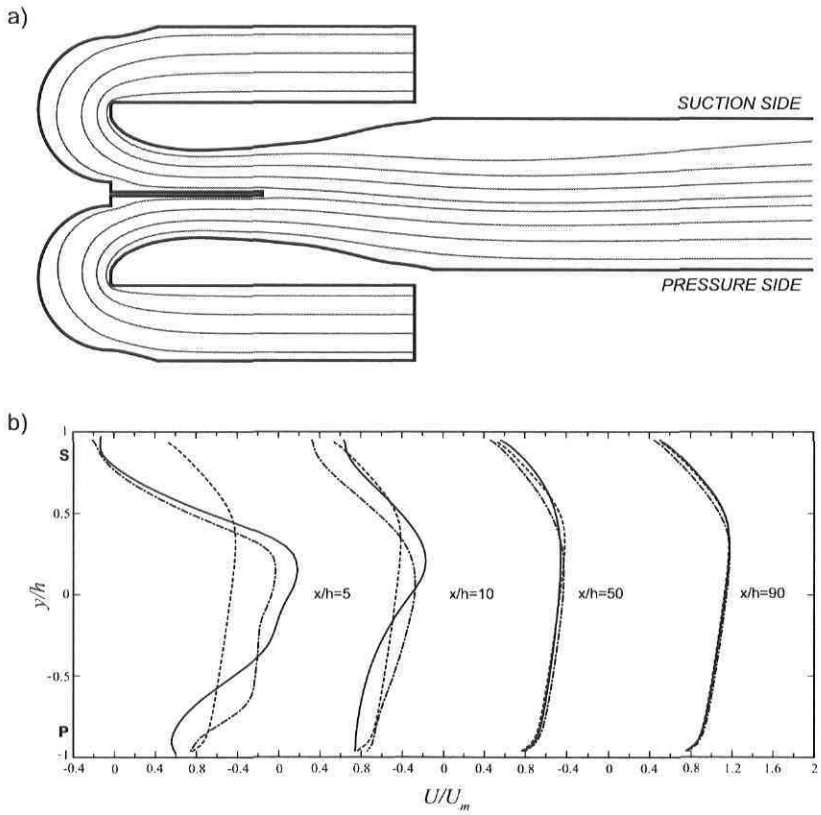

Figure B.2: 2D modified channel at $Re = 40000$ and $Ro = 0.22$. (a): Streamlines; (b): streamwise velocity profiles at different stations along the channel: ——, Actual channel; — – —, modified channel; – –, fully developed solution.

B.3 Actual channel with symmetric lips and flaps

To eliminate the separation bubble on the suction side of the channel having symmetric lips, two flaps are placed on the last portion of the lips. The flaps have a length of about $1.5h$ and they are at a distance of $0.3h$ from the lips.
The flaps eliminate the recirculating zone on the suction wall but the flow separates near the end of the pressure side flap. This small separation is responsible for the momentum deficit visible in the velocity profile of FIG. B.3b. Once more, no actual improvement in the flow development is observed.

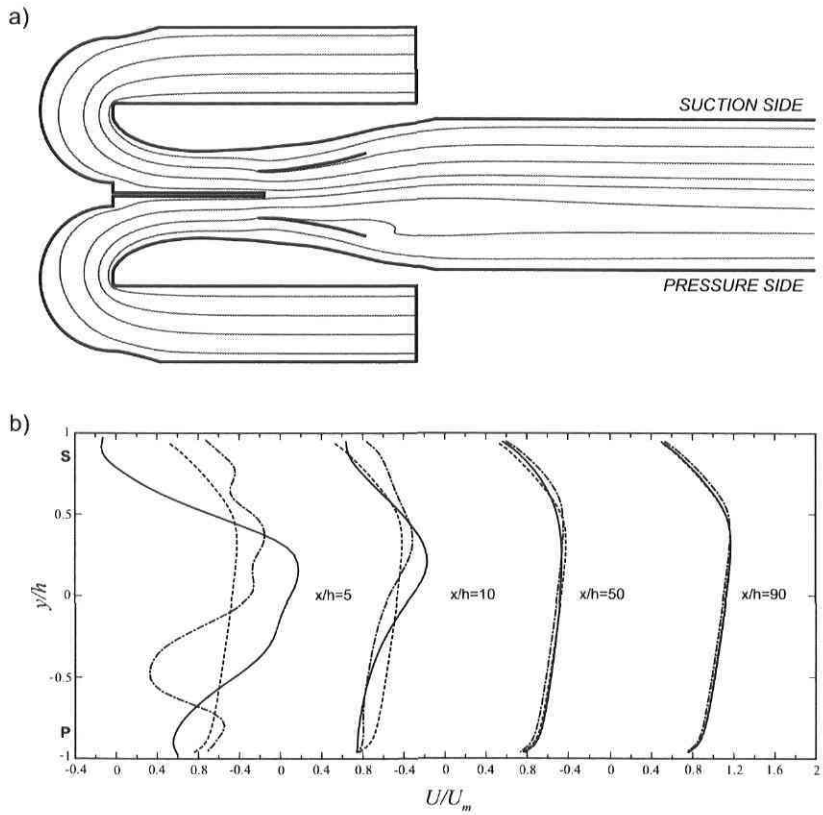

Figure B.3: 2D modified channel at $Re = 40000$ and $Ro = 0.22$. (a): Streamlines; (b): streamwise velocity profiles at different stations along the channel: ——, Actual channel; — – —, modified channel; – –, fully developed solution.

B.4 Actual channel with symmetric lips, flaps and filters

With this configuration, in addition to the lips and flaps, two porous membranes of thickness 0.5mm are placed normal to the flow direction at x/h=30. The membranes are attached on the pressure and suction walls and have a length of $0.5h$. The objective is to slightly readjust the momentum distribution across the channel.
In order to simulate a porous membrane with *Fluent*, a *porous jump* boundary condition must be used. With this b.c., three parameters have to be specified: the face permeability (α), the porous medium thickness (Δm), and the pressure jump coefficient (C_2). Since the local Reynolds number based on the membrane porosity ($Re_\delta = U_b\delta/\nu \approx 10$) is quite small, Darcy's law can be used:

$$\Delta p = -(\mu/\alpha)U\Delta m. \tag{B.1}$$

From equation (B.1), and by knowing by what percentage the velocity has to be decreased, the permeability of the medium can be estimated:

$$\Delta p = \frac{1}{2}\rho \left(U^2_{x=30h} - U^2_{fd}\right) = -(\mu/\alpha)U\Delta m. \tag{B.2}$$

In this case, the required permeability is $\alpha = 8 \times 10^{-8}$.
The effect of the porous membranes is visible on the velocity profile at $x/h = 50$, where a slight flow acceleration is induced in the central region of the channel. With this configuration, the flow development is slightly improved, but not sufficiently to motivate an implementation in the experimental setup. Moreover, the membranes may have a negative effect on the development of the Ekman layer in the 3D duct.

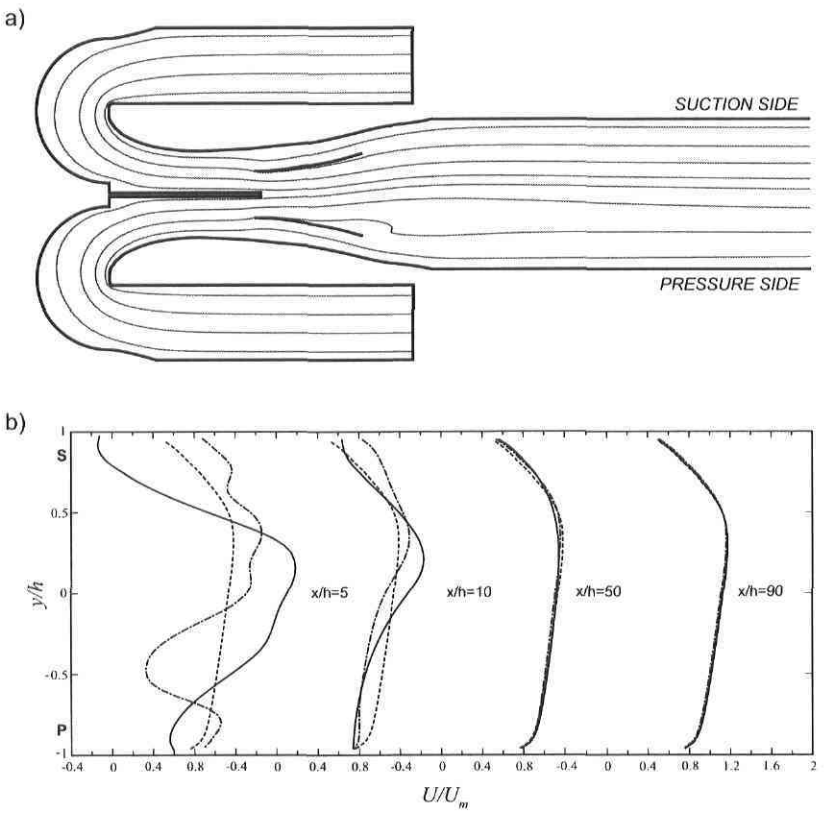

Figure B.4: 2D modified channel at $Re = 40000$ and $Ro = 0.22$. (a): Streamlines; (b): streamwise velocity profiles at different stations along the channel: ——, Actual channel; — – —, modified channel; – –, fully developed solution.

Appendix C

Parallel solver performance

In this section, 2D and 3D calculations are run in steady and unsteady mode in order to evaluate the performance of a parallel solver. The computer is a UNIX machine with two processors of 2.4GHz each, and a RAM of 4Go. The command used to launch a *Fluent* simulation in "background" mode is:
fluent 3ddp -t2 -g -i filename.jou > & output.dat &, where the *.jou* file includes all the parameters of the problem and the *.dat* file contains the convergence history. To achieve the best performance for parallel calculations, the interface between the partitions is minimized and each partition has the same number of cells.
3D cases are run with a RSM turbulence model which yield to a system of twelve

Case	# of cells	Bisection method	# of iter.	Comp. time	Time/iter.
3D steady	730 000	Serial solver	40	24.2 min	36.3
3D steady	730 000	Cartesian X-coord.	40	16.9 min	25.4 s
3D steady	1 200 000	Serial solver	40	40 min	60 s
3D steady	1 200 000	Cartesian X-coord.	40	26.3 min	39.5 s
2D steady	1 120 000	Serial solver	100	14.6 min	8.8 s
2D steady	1 120 000	Cartesian Y-coord.	100	9.4 min	5.6 s
2D steady	64 000	Serial solver	1000	7.7 min	0.46 s
2D steady	64 000	Cartesian X-coord.	1000	6.0 min	0.36 s
2D unsteady	1 120 000	Serial solver	5 ts	49.5 min	9.9 min/ts
2D unsteady	1 120 000	Cartesian Y-coord.	5 ts	35.4 min	7.1 min/ts
2D unsteady	64 000	Serial solver	20 ts	2.5 min	7.5 s/ts
2D unsteady	64 000	Cartesian X-coord.	20 ts	2.2 min	6.6 s/ts

Table C.1: Computational time of serial and parallel solvers.

equations, whereas 2D cases only require the resolution of three equations. The computation time for the serial solver (one processor) and the parallel solver are compared in TABLE C.1, and the computational gain from using a parallel solver is presented in TABLE C.2.

Case	# of cells	Computational gain
3D steady	730 000	30%
3D steady	1 200 000	34%
2D steady	1 120 000	36%
2D steady	64 000	22%
2D unsteady	1 120 000	30%
2D unsteady	64 000	12%

Table C.2: Computational gain from parallel solver.

The results show that the parallel computations always require a shorter period of time. As expected, the computational gain increases as the problem size becomes larger.
The performance of the dual processor machine is also compared with a single processor computer of 3.4GHz and 2Go of memory. The same test cases are used in the following analysis. The values of TABLE C.3 indicate that the computer equipped with a single

Case	# of cells	Computational gain
3D steady	730 000	-17%
3D steady	1 200 000	-7%
2D steady	1 120 000	-6%
2D steady	64 000	-15%
2D unsteady	1 120 000	-15%
2D unsteady	64 000	-25%

Table C.3: Computational gain from parallel solver.

3.4GHz processor outperforms a dual processor machine of 2.4GHz. Thus, the processor frequency is a key factor in the computational time required to run a simulation.